Aerosol optical properties at a savannah grassland site in South Africa

M Venter

orcid.org 0000-0001-5311-4085

Thesis accepted in fulfilment of the requirements for the degree *Doctor of Philosophy in Science with Atmospheric Chemistry* at the North-West University

Promoter:	Prof JP Beukes
Co-promoter:	Prof PG van Zyl

Graduation May 2020

22120017

Acknowledgments

'God keeps his promise, and he will not allow you to be tested beyond your power to remain firm; at the time you are put to the test, he will give you the strength to endure it and so provide you with a way out'. – 1 Corinthians 10:13 TEV

I have fulfilled a lifelong dream by completing my thesis. Ever since I was a high school student, I dreamt to one day complete a PhD study. And now, by concluding my thesis, I realised that I did. Although only my name appears on the front cover of this thesis, I received substantial support from my family, friends, colleagues, institutions and organisations. But most of all, I could not complete this thesis on my own, but only through the strength I have received from God. Therefore, I would like to praise and thank my Heavenly Farther for the opportunity He has granted me to pursue and complete my thesis. He had blessed me with courage, strength, determination, wisdom and the support of wonderful people throughout this journey.

I would also like to sincerely thank the following people:

My husband, Andrew, for all your support, motivation, understanding, prayers and willingness to help. You believed in me, encouraged me and gave me new perspective when I was demotivated. Thank you for your contribution, I am grateful to have had you part of every step in this journey.

My mentors, Prof Paul Beukes and Prof Pieter van Zyl, for your guidance, assistance and encouragement during this study. You have enabled me to develop an understanding of atmospheric science and what it takes to be a research scientist; I will forever be grateful.

My mother, Ilze, for your unconditional love, support, prayers and for having faith in me throughout my study. You have made me the person I am today by teaching me valuable life lessons and have shown me that hard work pays off. You are an inspiration.

My parents-in-law, Kobus and Rosemary, for your unconditional love, support and prayers during this study.

To my brother, Henri, for your love and care that only a sibling can give, and your understanding and support.

My family and friends for your understanding and encouragement.

To the Atmospheric Research and Chromium Technology Groups at the North-West University and the National Research Foundation (NRF) for the financial support toward this research.

Thank you

Marcell

Abstract

Atmospheric aerosols affect the earth's radiative budget in two ways: firstly, particles directly absorb and scatter short- and long-wave radiation and, secondly, particles indirectly influence the lifetime and physical properties of clouds. There are many uncertainties associated with these effects of atmospheric aerosols on the earth's radiative budget due to their high spatial and temporal variability of aerosol optical properties, particularly on regional scales. Consequently, high-resolution long-term, regional scale aerosol optical property measurements are required in order to decrease the uncertainties.

Southern Africa is an important sub-source region of Africa where open biomass burning produces significant amounts of aerosols, especially during the dry season. Within southern Africa, South Africa is the largest economy with numerous primary and secondary sources of aerosols.

Only a few papers have been published on aerosol optical properties in South Africa. Therefore, to partially address this knowledge gap, i.e. long-term ground level *in situ* aerosol optical data, aerosol optical properties, which include scattering and absorption coefficients (σ_{SP} and σ_{AP}), single scattering albedo (ω_0), and Ångström exponent (α_{SP}), are investigated based on *in situ* measurements conducted from September 2011 to November 2016 at the Welgegund measurement station. The σ_{SP} was measured with a three wavelength light scattering Nephelometer and the σ_{AP} with a multi-angle absorption photometer. The α_{SP} and ω_0 were calculated from the σ_{SP} and σ_{SP} and σ_{AP}, respectively.

Relatively well-defined seasonal and diurnal patterns were observed, which indicated the influence of open biomass burning frequencies, other possible sources (e.g. industrial emissions, domestic combustion, wind-blown dust) and meteorological effects (e.g. temperature, relative humidity, planetary boundary layer daily evolution and air mass circulation patterns).

Two main approaches, i.e. auto-generated source maps and defined source regions, were used to identify more unambiguously the sources and source areas that influenced the aerosol optical properties. From these two approaches, the contributions of seasonal sources (e.g. open biomass burning, domestic combustion for space heating, wind-blown dust) and continuous emission sources (e.g. industrial emissions and domestic combustion for cooking) were observed. From the auto-generated source maps, considering all aerosol optical properties for the entire measurement period, anthropogenic activities such as emissions from the Vaal Triangle, Mpumalanga Highveld, and Johannesburg-Pretoria megacity, as well as the aging and recirculation of pollution over the dominant anti-cyclonic recirculation pattern, in addition to high open biomass burning frequencies especially over eastern Zimbabwe and central Mozambique had the most significant effects on the aerosol optical properties (e.g. higher σ_{SP} and σ_{AP}), if compared to the background sector between west-southwest and south-southwest of Welgegund. The auto-generated source maps for defined periods, i.e. warmest/wettest, coldest and driest, peak open biomass burning, indicated the contributions from sources and/or source areas even better. From the warmest/wettest period for all aerosol optical properties, the contribution of air masses that had passed over industrial activities and the dominant anti-cyclonic recirculation pattern were evident. The coldest period mostly indicated the contribution of higher population densities (more domestic combustion for space heating) in addition to industrial activities that contribute year-round. From the driest period, the contributions of open biomass burning frequencies of air masses that had passed over eastern Zimbabwe and central Mozambique were evident for all aerosol optical properties.

The defined source regions approach was subdivided into three different methods that further improved the understanding of possible sources and source regions influencing aerosol optical properties. The predefined eastern and western sectors method allowed the comparison of aerosol optical properties for air masses that had passed over the eastern (higher industry population densities and open biomass burning frequencies), and western (very few industries, lower population densities and lower open biomass burning frequencies) sectors during the warmest/wettest and driest periods. From this comparison, the significant differences between the two

defined sectors and contributions of open biomass burning to all aerosol optical properties during the driest period were evident. The predefined source regions approach allowed the comparison of aerosol optical properties for air masses that had passed over the anthropogenic source regions in the eastern sector. From this approach, it was evident that the aerosol optical properties were significantly altered (if compared to the regional background) in air masses that had passed over the anthropogenic influenced source regions in the South African interior. For example, the σ_{SP} and α_{SP} indicated the extent of pollution of air masses that had passed over the Vaal Triangle (VaalT), as well as the occurrence of wind-blown dust that travelled over the VaalT from the eastern Free State to Welgegund. In the last method, information obtained by the predefined and auto-generated source map region methods was applied, which allowed the comparison between two separate background regions, i.e. Karoo and Kalahari, and two anthropogenically influenced regions, i.e. anti-cyclonic recirculation pattern and the industrial hub, during different periods, i.e. warmest/wettest, coldest and driest periods. From these aerosol optical properties results, it was evident that air masses that had passed over the Karoo were typically cleaner (e.g. lower σ_{SP} and σ_{AP}) than air masses that had passed over the Kalahari, and that air masses that had passed over the industrial hub during the coldest period were the most polluted (e.g. highest σ_{SP} and σ_{AP}).

To contextualise the aerosol optical properties measured at Welgegund, mean values were compared with other sites. The highest mean aerosol optical property values during all periods were lower than the mean values reported for polluted sites. The mean aerosol optical property values measured in air masses that had passed over the Karoo region during all periods were similar and/or higher to mean values reported for true background sites. The mean ω_0 for Welgegund over the entire measurement period was comparable with the mean ω_0 reported for Elandsfontein in the Mpumalanga Highveld. However, it was not that straightforward to contextualise the Welgegund ω_0 values with other sites, since the climatological effect of ω_0 depends on the albedo of the underlying surface.

Lastly, a statistical approach, i.e. multi-linear regression analysis, was applied to serve as an additional, independent analysis to support the source deductions made in the earlier chapters. Although the interpretations of the meaning of parameters

included in the optimum multi-linear regression equations, and the signs (positive or negative) associated with them, were somewhat speculative, it did indicate that the earlier source deductions were plausible.

Keywords: atmospheric aerosols, aerosol optical properties, scattering coefficient, absorption coefficient, single scattering albedo, Ångström exponent, Welgegund

Index

List of figures

Chapter 2

Chapter 3

Chapter 4

Chapter 5

Chapter 7

List of tables

Chapter 2

Chapter 6

Abbreviations

Al	Aluminum
Al_2O_3	Aluminium oxide
Anti-EBC	Combined anti-cyclonic recirculation pattern and Eastern Bushveld Complex
Ar	Argon
As	Arsenic
B	Boron
Back	Background
BC	Black carbon
BVOC	Biogenic volatile organic compound
$Ca(NO_3)_2$	Calcium nitrate
$CaSO_4$	Calcium sulphate
CO_2	Carbon dioxide
CO_x	Carbon oxides
CO	Carbon monoxide
Cl^-	Chlorine ion
Cr	Chromium
CCN	Cloud condensation nuclei
DMS	Dimethylsulphide
Fe_2O_3	Ferric oxide
Fe	Iron
GAW	Global Atmospheric Watch

GDAS	Graphical Data Analysis System
H_2	Hydrogen
HCl	Hydrogen chloride
HEPA	High Efficiency Particulate Air
HF	Hydrogen fluoride
H_2O_2	Hydrogen peroxide
H_2S	Hydrogen sulphide
HSO_3	Hydrogen sulphite
Hg	Mercury
HNO_3	Nitric acid
H_2SO_4	Sulphuric acid
HV	Mpumalanga Highveld
HV-MC	Combined Mpumalanga Highveld and megacity
HYSPLIT	Hybrid Single-Particle Lagrangian Integrated Trajectory
IN	Ice nuclei
IPCC	Intergovernmental Panel on Climate Change
Jhb-Pta	Johannesburg-Pretoria
K^+	Potassium ion
MAAP	Multi-angle absorption photometer
MC	Megacity
Mg^{2+}	Magnesium ion
$Mg(NO_3)_2$	Magnesium nitrate
MLR	Multi-linear regression
MODIS	Moderate Resolution Imaging Spectroradiometer

NCEP	National Weather Service's National Center for Environmental Prediction
NH_3	Ammonia
NH_4^+	Ammonium
NH_4HSO_4	Ammonium bisulphate
NPF	New particle formation
NO_3^-	Nitrate
N_2	Nitrogen
NO_x	Nitrogen oxides
NaCl	Sodium chloride
Na^+	Sodium ion
$NaNO_3$	Sodium nitrate
Na_2SO_4	Sodium sulphate
$OH^\bullet$	Hydroxyl radical
OA	Organic aerosols
OC	Organic carbon
O_2	Oxygen
O_3	Ozone
Pb	Lead
PM	Particulate matter
PM_{10}	Particulate matter with an aerodynamic diameter ≤ 10 μm
$PM_{2.5}$	Particulate matter with an aerodynamic diameter ≤ 2.5 μm
PSAP	Particle soot absorption photometer
PAS	Photoacoustic spectrometer
PBL	Planetary boundary layer

POA	Primary organic aerosols
RH	Relative humidity
RMSE	Root mean square error
SOA	Secondary organic aerosols
SVOCs	Semi-volatile organic compounds
Si	Silicon
SiO_2	Silicon dioxide
SAFARI	Southern African Regional Science Initiative
SHARP	Synchronised hybrid ambient real-time particulate
SO_4^{2-}	Sulphate
SO_2	Sulphur dioxide
SO_x	Sulphur oxides
T	Temperature
UV	Ultra violet
VaalT	Vaal Triangle
VOCs	Volatile organic compounds
WBC	Western Bushveld Complex
WHO	World Health Organization
σ_{AP}	Absorption coefficient
α_{SP}	Ångström exponent
σ_{SP}	Scattering coefficient
ω_0	Single scattering albedo

Chapter 1

Background, motivation and objectives

1.1. Background and motivation

Atmospheric aerosols are small solid or liquid particles that are suspended in the air. Aerosols originate from a mixture of natural (e.g. dust storms, volcanos, sea spray, lightning-induced open biomass burning) and anthropogenic (e.g. open cast mines, human-initiated open biomass burning, domestic combustion and industry) sources (Boucher, 2015; Williams & Baltensperger, 2009; Arimoto, 2003; Penner *et al*., 2001;). Physical properties of aerosols include the size, morphology, number and shape thereof. Aerosols are usually reported as particulate matter (PM) in different size ranges (e.g. PM_1, $PM_{2.5}$ and PM_{10}) and measured by mass concentration ($\mu g/m^3$). Aerosols have adverse health effects on the respiratory systems of humans and animals (Anderson, 2009). The adverse effects of aerosols on plants and the general planetary health include: soil nutrient enrichment/depletion, changing of the aquatic balance (e.g. pH) and changing of the global radiative balance due to their optical properties. The optical properties of aerosols are characterised by light scattering and absorption (Penner *et al.*, 2001; Andreae, 1995). Aerosol particles have direct (the scattering or absorption of radiation) and indirect (e.g. acting as cloud condensation nuclei) radiative effects on the Earth's climate system (Boucher, 2015; Penner *et al.*, 2001, Pöschl, 2005). The uncertainties associated with atmospheric aerosol properties in southern Africa have been emphasised in previous studies (Swap *et al.*, 2003; Laakso *et al.*, 2012; Laakso *et al.*, 2008; Ross *et al.*, 2003; Vakkari *et al.*, 2011; Queface *et al.*, 2001). These studies indicated that aerosol particles in South Africa have distinctive characteristics due to South Africa's unique sources and meteorological conditions. Examples of the latter include the anti-cyclonic recirculation pattern that can be observed over the central Highveld that traps pollutants for several days, strong inversion layers observed during the cold winter months that prevent vertical mixing (Gierens *et al*., 2019; Korhonen *et al*., 2014; Laakso *et al.*, 2012; Garstang *et al.*, 1996; Tyson *et al.*, 1996), as well as

pronounced differences between dry (May to mid-October) and wet (mid-October to April) periods that impact significantly on aerosol removal rates.

Notwithstanding the significance of the climatic effect of aerosols and the importance of South Africa (and southern Africa in general) within a regional and global atmospheric science perspective, few papers have been published on aerosol optical properties in South Africa. Most of these papers used vertical and/or remote sensing techniques to obtain aerosol optical data (Kumar *et al*., 2014; Queface *et al*., 2011; Campbell *et al*., 2003; Eck *et al*., 2003; McGill *et al*., 2003; Swap *et al*., 2003; Formenti *et al*., 2002; Diner *et al*., 2001), mostly focused only on measurements during open biomass burning periods (Campbell *et al*., 2003; Eck *et al*., 2003; McGill *et al*., 2003; Swap *et al*., 2003; Diner *et al*., 2001), and were generally based on short measurement periods during the SAFARI 2000 campaign (Swap *et al*., 2003). As far as the candidate could assess, the paper published by Laakso *et al*. (2012) is the only study to date where ground-level, longer-term (2 years for the aforementioned paper) aerosol optical properties, based on *in situ* ground level aerosol absorption and scattering measurements in South Africa, have been published. Although this paper made a significant contribution, it was a general paper that considered various aerosol and gas measurements, and therefore did not focus specifically on explaining observed aerosol optical phenomena in detail. Furthermore, no diurnal patterns were presented and possible source explanations were quite general. Additionally, the Laakso *et al*. (2012) measurement site (i.e. Elandsfontein) was situated in the internationally well-known NO_2 hotspot visible with satellite observations (Lourens *et al*., 2012), implying that the aerosol optical data are only representative of this relatively small area. In South Africa, the Cape Point Global Atmosphere Watch (GAW) station (Slemr *et al*., 2015; Venter *et al*., 2015; Slemr *et al*., 2013) also measures ground-level *in situ* aerosol absorption and scattering on a long-term basis; however, results from there have not yet been published in the peer-reviewed public domain.

1.2. Objectives

The general aim of this study is to investigate long-term aerosol optical properties measured at a savannah background site in the South African interior to gain insight into possible regional important sources and/or contributing factors.

The specific objectives include:

i. Obtain a suitable long-term dataset measured in the South African interior, which can be used to evaluate the aerosol optical properties;
ii. Process the raw data to calculate scattering (σ_{SP}) and absorption (σ_{AP}) coefficients, single scattering albedo (ω_0) and Ångström exponent (α_{SP}) for the entire dataset;
iii. Determining temporal patterns, i.e. diurnal and seasonal, for all the aerosol optical properties and make general deductions with regard to contributing sources and/or factors influencing the aerosol optical properties;
iv. Use more advanced data analysis techniques to investigate possible sources and/or factors influencing the aerosol optical properties;
v. Contextualise the aerosol optical properties (overall, seasonal and for specific source regions) within local and international perspectives; and
vi. Use a statistical tool to independently (without prejudice of candidate) evaluate source deductions made in (iii) and (iv).

Chapter 2

Literature survey

In this chapter, the general background of the atmospheric structure and climate system is presented in section 2.1. Thereafter, aerosols (section 2.2) are discussed in terms of sources, size and number concentrations, sinks, health effects, types of aerosols, and aerosol effects on climate. Previous studies in South Africa are presented in section 2.3 in terms of aerosol sources, studies of aerosol optical properties and meteorology in South Africa. Lastly, aerosol optical properties are introduced and discussed in section 2.4.

2.1 Introduction to the atmosphere and climate system

Climate can be described as the statistical properties of meteorological conditions, i.e. atmospheric pressure, winds, clouds, precipitation, temperature and relative humidity (RH), over a given time, where such period should be long enough to sample these meteorological conditions, but not too long to recognise natural and anthropogenic variations (Seinfeld & Pandis, 2016; Boucher, 2015; Barry & Hall-McKim, 2014). Climatology therefore differs from meteorology, which is the short-term fluctuations of the atmosphere (Boucher, 2015; Barry & Hall-McKim, 2014). The climate system comprises five interactive adjoined components that can be observed in Figure 2-1, i.e. the atmosphere, the hydrosphere (including the ocean), lithosphere (continental surfaces), cryosphere (defines all forms of ice on the planet) and marine and terrestrial biosphere (all living organisms on the planet) (Boucher, 2015; Barry & Hall-McKim, 2014; Lockwood, 2009). All these components are open and non-isolated as they act as flowing systems that are linked by complex feedback processes (Barry & Hall-McKim, 2014; Lockwood, 2009). The climate forms from the basic properties of these components and the interactions that exist between them within the boundary conditions, e.g. solar energy, the earth's orbit, ocean currents, clouds, volcanic activity and pollutants of anthropogenic emissions, which are enforced onto the climate system (Seinfeld & Pandis, 2016; Boucher, 2015).

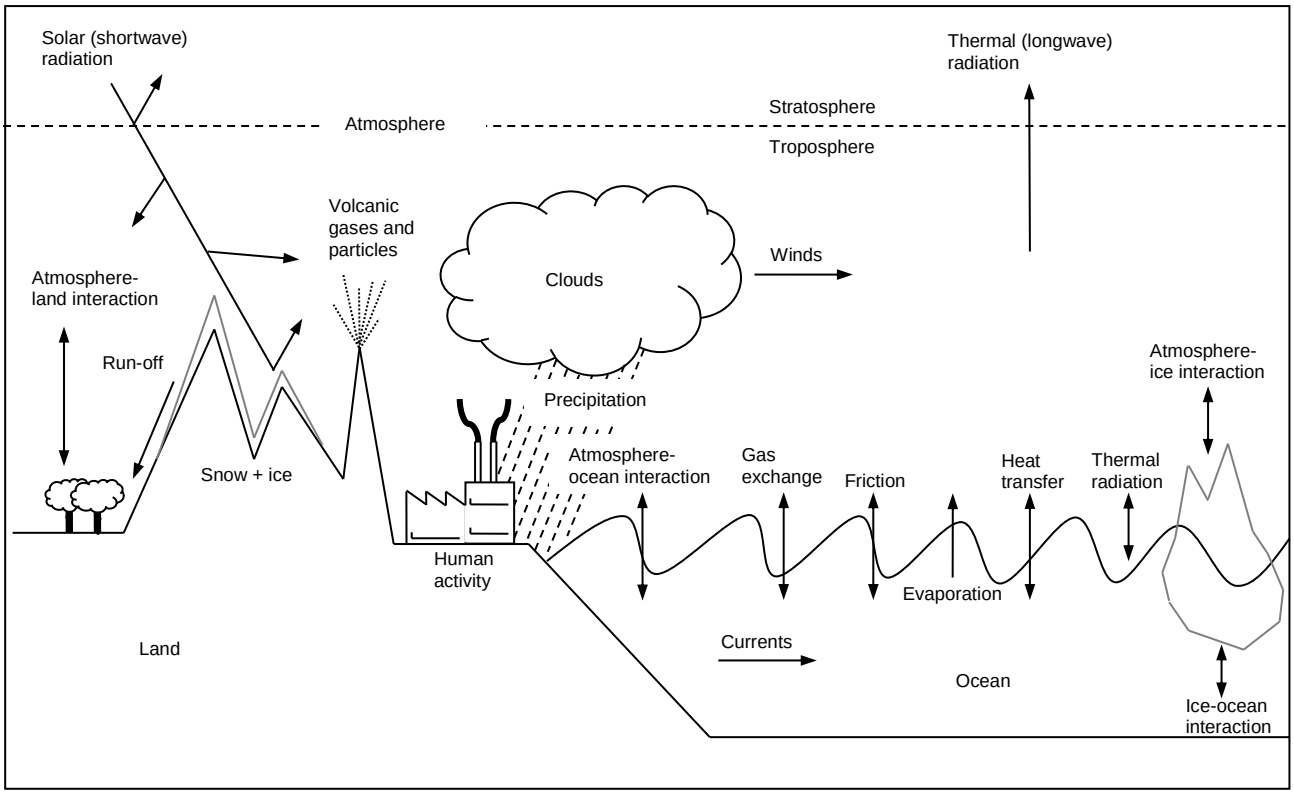

Figure 2-1: Interactions of different components in the climate system (based on Lockwood, 2009)

Figure 2-1 presents the interactions of different components in the climate system. The atmosphere is a thin layer that is held around the earth by gravity and comprises 78 % molecular nitrogen (N_2), 21 % molecular oxygen (O_2), 1 % argon (Ar), and other trace gases, which represent less than 1 % of the atmosphere (Seinfeld & Pandis, 2016; Boucher, 2015; Fishmen, 2003). Water vapour is the second most abundant component that is mainly found in the lower atmosphere in highly variable contents in both space and time (Seinfeld & Pandis, 2016; Boucher, 2015). As the altitude of the atmosphere increases, pressure and air density decrease. These variations of temperature and pressure with height are used to characterise the earth's atmosphere, and therefore the variation of the average temperature profile with altitude is used to distinguish between the layers of the atmosphere (Seinfeld & Pandis, 2016; Boucher, 2015):

- The troposphere is the lowest layer of the atmosphere that extends from the earth's surface to an altitude of ~10 – 15 km, depending on the latitude, i.e. the troposphere is the shallowest at the poles and the deepest in the tropics, and

season, i.e. thicker during the summer than the winter (Pidwirny, 2019; Seinfeld & Pandis, 2016; Boucher, 2015). In this layer, temperature decreases (average ~15 °C – ~-57 °C) with altitude, and rapid vertical mixing via convection occurs (Pidwirny, 2019; Seinfeld & Pandis, 2016). The planetary boundary layer (PBL) is a part of the troposphere that is directly influenced by the earth's surface, with a thickness of ~1 – 2 km (Boucher, 2015). The tropopause is the layer above the PBL and extends to the top of the troposphere (Boucher, 2015). The gradient temperature (lapse rate) of the atmosphere is associated with the cooling of air as it expands. It can typically vary from 5 K km^{-1} in wet conditions to ~10 K km^{-1} in dry conditions (Pidwirny, 2019; Boucher, 2015). The difference between the latter is due to latent heat being released when water condenses in the atmosphere, thereby decreasing the vertical temperature gradient (Pidwirny, 2019; Boucher, 2015).

- The stratosphere contains ~20 % of the total mass of the atmosphere and extends from the tropopause to a height of ~45 to 55 km where temperature increases (ranging from -57 °C to 0 °C) with altitude, due to ozone (O_3) gas molecules that absorb ultraviolet (UV) radiation from the sun creating heat, leading to slower vertical mixing and being more stratified than the troposphere (Pidwirny, 2019; Seinfeld & Pandis, 2016; Boucher, 2015). This layer is also known as the ozone layer.

- The mesosphere lies above the stratosphere and extends up to ~80 to 90 km. Within this layer, the temperature decreases (average -90 °C) with altitude with a rapid vertical mixing (Seinfeld & Pandis, 2016; Boucher, 2015).

- The thermosphere extends from the mesosphere up to ~600 km, where temperatures are high (up to 1 200 °C) due to the absorption of shortwave radiation by N_2 and O_2 and rapid vertical mixing (Pidwirny, 2019; Seinfeld & Pandis, 2016). Ions are produced by photoionisation in the ionosphere (upper mesosphere and lower thermosphere) (Seinfeld & Pandis, 2016).

- The exosphere is the uppermost layer of the atmosphere where air density is extremely low and gas molecules with sufficient energy can escape from the gravitational forces of the earth (Seinfeld & Pandis, 2016; Boucher, 2015).

The earth's climate system depends on two main external forcings, which determine its behaviour, i.e. solar radiation and the external conditions (Boucher, 2015; Lockwood, 2009). Solar radiation is considered to be the primary forcing mechanism and provides almost all the energy that controls the climate system (Boucher, 2015, Lockwood, 2009). Incoming solar radiation depends on the amount of radiation emitted by the sun and also on the earth's orbit characteristics around the sun that vary in time (Boucher, 2015). The climate system can be considered as an engine that turns solar radiation, absorbed by the earth's surface and atmosphere, into terrestrial radiation emitted by the surface and the atmosphere where some of the terrestrial radiation escapes to space and cools down the planet (Boucher, 2015). Solar radiation is shortwave radiation, e.g. UV, visible and near-infrared. In contrast, terrestrial radiation is longwave radiation, e.g. infrared (Boucher, 2015). Variations in the energy fluxes of solar and terrestrial radiation in the atmosphere that are induced by natural and anthropogenic changes in atmospheric composition, solar activity or earth surface properties can be defined as radiative forcing (Pöschl, 2005; Penner, 2001). There are three forms of matter present in the atmosphere that affect the radiative budget:

- Gas molecules: Molecular N_2 and O_2 make up more than 99 % of the atmosphere's volume (Boucher, 2015; Fishman, 2003). They are largely transparent to solar and terrestrial radiation, but can scatter solar radiation. Trace gases that can absorb and emit solar and/or terrestrial radiation are called greenhouse gases (Seinfeld & Pandis, 2016; Boucher, 2015).

- Hydrometeors: A hydrometeor is any liquid, water or ice particle suspended in or falling through the atmosphere (Boucher, 2015; Jacobson, 2002). Examples of hydrometeors are cloud droplets, ice crystals, raindrops, hailstones and snowflakes (Boucher, 2015).

- Aerosols: They are small particles that can exist in solid, liquid and semi-liquid form that are suspended in the atmosphere (Boucher, 2015; Jacobson, 2002). The difference between aerosols and hydrometeors is that the latter contains more water and are bigger in size. Aerosols also interact with solar radiation (Boucher, 2015, Jacobson, 2002).

Figure 2-2, presented by the IPCC's fifth assessment report (IPCC, 2013), indicates the radiative forcing estimates in 2011 relative to 1750 and the aggregated uncertainties for the main driver of climate change. According to this figure, the total anthropogenic radiative forcing for 2011 is 2.29 [1.13 - 3.33] W m^{-2}. For well-mixed greenhouse gasses (CO_2, CH_4, N_2O and Halocarbons) the radiative forcing emissions is 3.00 [2.22 – 3.78] W m^{-2}, which has a warming effect on the earth's radiative budget. The radiative forcing for the total aerosol effect on the atmosphere, including cloud adjustments due to aerosols is -0.9 [-1.9 -- -0.1] W m^{-2}, which has a cooling effect on the earth's radiative budget. This total radiative forcing of aerosols results from a negative radiative forcing from most aerosols and a positive radiative forcing from black carbon (BC), which absorbs solar radiation (IPCC, 2013).

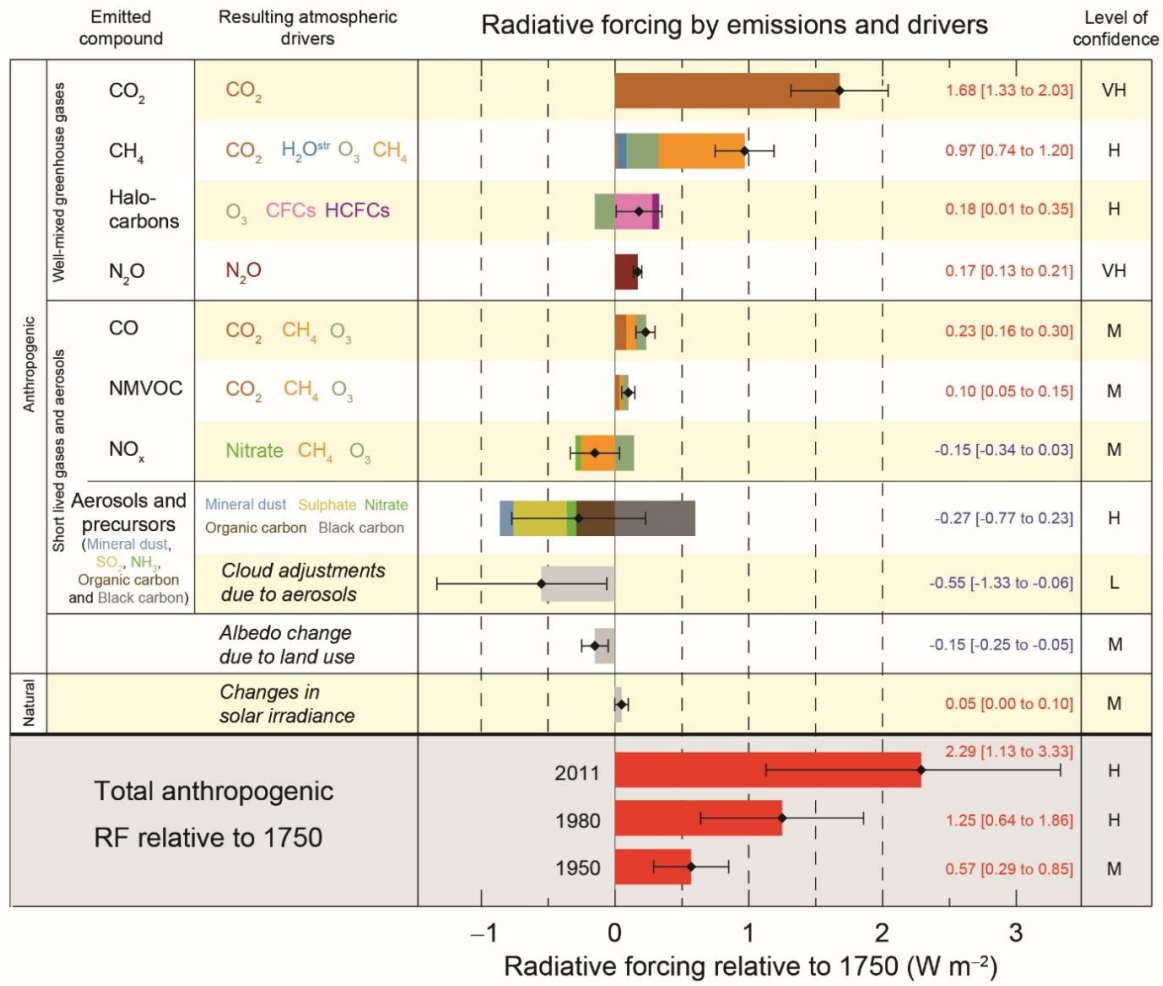

Figure 2-2: Components affecting radiative forcing in 2011 relative to 1750 (IPCC, 2013).

2.2 Aerosols

To differentiate between cloud particles from other types of particles in the atmosphere, aerosols can be defined as small solid or liquid particles that are suspended in the air, with the exception of all hydrometeors (e.g. cloud droplets, raindrops, ice crystals, graupel and snowflakes) (Seinfeld & Pandis, 2016; Boucher, 2015; Williams & Baltensperger, 2009; Pöschl, 2005). The concentration of aerosols in the atmosphere varies due to a large heterogeneity of sources and relatively short lifetime, which varies from a few hours to weeks depending on the particle, meteorological environments and particle properties (Turner & Colbeck, 2008; Pöschl, 2005). Aerosols have different properties, i.e. chemical composition, size, number and shape that are variable in space and time and can be classified according to these properties (Boucher, 2015).

Atmospheric aerosols can be emitted as primary or secondary species. Primary aerosols are emitted directly from natural or anthropogenic sources, e.g. aerosols produced during incomplete combustion and wind-blown dust from terrestrial surfaces (Boucher, 2015; Williams & Baltensperger, 2009; Pöschl, 2005). In contrast, secondary aerosols are formed from chemical reactions between primary aerosols and/or gases and/or water droplets already present in the earth's atmosphere, e.g. new particle formation (NPF) by condensation and nucleation of gaseous precursors (Boucher, 2015; Pöschl, 2005). Gas-to-particle conversion followed by condensational growth of the newly formed nanoparticles is often observed in the atmosphere (Kulmala *et al*., 2004). Secondary aerosol formation processes can be further categorised as homogeneous or heterogeneous. When condensable gases nucleate to form new particles in the atmosphere, it refers to homogeneous formation (Jacobson, 2002). Heterogeneous formation refers to the condensational growth on pre-existing nuclei (Williams & Baltensperger, 2009; Turner & Colbeck, 2008; Jacobson, 2002). Aerosol properties also vary spatially due to differences in the environment, but aerosols are not always representative of the surrounding environment due to transportation (Boucher, 2015).

Aerosols can further be classified into natural and anthropogenic origin or a mixture thereof. Natural sources include emissions from soils, ocean, natural open biomass

burning, vegetation and volcanoes (Boucher, 2015; Williams & Baltensperger, 2009; Jacobson, 2002). Anthropogenic sources largely include emissions from industrial activities (e.g. combustion of fossil fuels such as coal and oil), agricultural activities, induced open biomass burning, mining (e.g. dust), vehicle emissions and domestic combustion (cooking and space heating) (Boucher, 2015; Jacobson, 2002; Williams & Baltensperger, 2009). According to Jacobson (2002), emissions from anthropogenic sources are greater than emissions from natural sources. Natural and anthropogenic sources are discussed in more detail in section 2.2.1.

Aerosols can affect the radiative forcing of the climate system due to their different physical and chemical properties (Boucher, 2015; Williams & Baltensperger, 2009; Pöschl, 2005). Scattering and reflection of solar radiation by aerosols and clouds have a negative radiative forcing and tend to cool the earth's surface, whereas absorption of solar radiation, mostly by greenhouse gases and clouds, but also aerosols, has a positive radiative forcing and tends to warm the earth's surface (Pöschl, 2005). The fifth assessment report of the Intergovernmental Panel on Climate Change (IPCC) (2013) reported that most studies agree that anthropogenic aerosols have a net negative radiative forcing.

2.2.1 Sources of aerosols

2.2.1.1 Natural sources

Sea spray drops result from bursting of air bubbles formed by wind and wave action at the sea surface (Boucher, 2015; Williams & Baltensperger, 2009; Jacobson, 2002). Once airborne, the droplets can either return to the surface or evaporate to form organic or inorganic aerosols (Boucher, 2015; Williams & Baltensperger, 2009). Typical sizes for sea spray aerosols are from 100 nm to several tens of µm (Boucher, 2015; Williams & Baltensperger, 2009). The largest fraction of sea spray contains inorganic anions and cations, i.e. species in order of importance, chloride ion (Cl^-), sodium ion (Na^+), sulphate (SO_4^{2-}), magnesium ion (Mg^{2+}), potassium ion (K^+), calcium ion (Ca^{2+})and a smaller fraction of organic aerosols (OA) (Grythe *et al.*, 2014; Jacobson, 2002).

Mineral aerosols from arid and semi-arid regions are a large source (~45 %) of tropospheric aerosols (Marconi *et al.*, 2014). The chemical and physical weathering

of rocks and soils results in dust, consisting of minerals and organic materials, and is suspended by wind into the atmosphere (Boucher, 2015; Williams & Baltensperger, 2009; Arimoto, 2003; Jacobson, 2002). The extent of lifting depends on the particle mass and wind speed (Penner *et al*., 2001). Similar to sea spray particles, wind-blown dust particles have sizes from 100 nm to tens of µm. Larger particles (larger than 10 µm) fall out rapidly and particles between 1 and 10 µm stay suspended up to a few days to weeks in the atmosphere (Jacobson, 2002). Main sources of wind-blown dust include deserts, dust from unpaved roads, agricultural activities that include ploughing on loose soil to prepare for planting season, and dust storms (Jacobson, 2002).

Although volcanic eruptions only occur on a sporadic basis, it has a significant effect on the atmosphere when it occurs. Large quantities of water vapour, ash (mainly silicon dioxide, SiO_2, aluminium oxide, Al_2O_3 and ferric oxide, Fe_2O_3) and gases such as sulphur dioxide (SO_2), hydrogen sulphide (H_2S), carbon dioxide (CO_2), hydrogen chloride (HCl) and hydrogen fluoride (HF) are ejected into the atmosphere where SO_2 and H_2S are consequently oxidised to form SO_4^{2-} aerosols (Boucher, 2015; Andersson *et al*., 2013, Arimoto, 2003). The residence time of aerosols is relatively short if the sulphur-containing gases are emitted into the troposphere. However, if the volcanic explosion was powerful enough to inject the gases into the stratosphere, the aerosol residence time is much longer (a few months to more than a year) (Boucher, 2015).

Biological aerosols are also present in the terrestrial and marine biosphere. They contain plant and insect fragments, pollen grains, spores, bacteria, viruses, algae, fungi, protozoa and nematodes (Boucher, 2015; Arimoto, 2003; Williams & Baltensperger, 2009; Baltensperger & Furger, 2008). Depending on the size, particles can be transported by wind over varying distances. Plant and insect fragments are usually larger than 100 µm, large bacteria, pollen and spores are in the rage of 1 to 100 µm, and small bacteria and viruses are smaller than 1 µm (Boucher, 2015). Seawater also contains biological matter and is transferred into the atmosphere by sea spray (Boucher *et al.*, 2015; Baltensperger & Furger, 2008). Marine and terrestrial environments are also an important source of aerosol precursors (Boucher *et al.*, 2015; Williams & Baltensperger, 2009; Baltensperger &

Furger, 2008). A large natural source is the release of dimethylsulphide (DMS) from the ocean. DMS is produced by the biological activity of phytoplankton. It forms SO_4^{2-} aerosols through the photo-oxidation to methanesulphonic acid (CH_3SO_3H) and SO_2 (Boucher *et al.*, 2015; Williams & Baltensperger, 2009; Baltensperger & Furger, 2008). Volatile organic compounds (VOCs) are also emitted from plants and algae that are oxidised to contribute and condense as organic aerosols (OA) (Boucher, 2015; Crippa *et al*., 2013; Williams & Baltensperger, 2009). Aerosols such as these are called secondary biogenic aerosols with sizes of a few tenths of µm (Boucher *et al*., 2015).

2.2.1.2 Anthropogenic sources

Open biomass burning is the burning of organic material (e.g. wood, vegetation, peat), excluding fossil fuels (e.g. gas, oil and coal) (Boucher, 2015). It can be considered natural or anthropogenic (intentionally or as consequence of human behaviour) with most open biomass burning being anthropogenic (Boucher, 2015; Arimoto, 2003). Emissions from grassland or savannah burning mostly occur during the dry season when vegetation growth is less and biomass dries and contribute about 49.1 Tg yr^{-1} of aerosols globally (IPCC, 2013). The smoke consists of unburnt carbon and tars, which is evident of incomplete combustion (Jayaratne & Verma, 2001). Most of the particles emitted are in the form of submicron, accumulation mode particles (Jayaratne & Verma, 2001). Open biomass burning emissions produce organic carbon (OC, associated with hydrogen (H_2) and O_2 atoms), black carbon (BC) (soot, higher carbon content), SO_4^{2-}, nitrate (NO_3^-) and VOCs, which are aerosol precursors (Boucher, 2015, Jayaratne & Verma, 2001).

Production in the electricity generation and petrochemical industries is achieved by means of the pyrogenic processing of fossil fuels. Aerosol producing fossil fuels include coal, oil, natural gas, gasoline, kerosene and diesel. Emissions from these sources include soot (BC and OC), sulphur oxides (SO_x), nitrogen oxides (NO_x), particulate matter with an aerodynamic diameter less than or equal to 10 µm (PM_{10}), VOCs, trace metals, SO_4^{2-} and fly ash (Jacobson, 2002). Fly ash consists of aluminium (Al), silicon (Si), iron (Fe), Mg and Ca in the form of quartz, hematite, gypsum and clays (Jacobson, 2002).

In pyrometallurgical processes, dust can be emitted, i.e. raw material transport, bag filter dust, slag, ash and process residues. During the smelting processes off-gases are produced, containing dust, metalloid contents, VOCs, halogens and gaseous species such as SO_x, NO_x and carbon oxides (CO_x) (Westcott *et al.*, 2007; Apostolovski-Trujic *et al.*, 2007).

Large amounts of dust are released by mining operations during excavation, blasting, crushing, grinding and tailings management (Csavina *et al.*, 2012; Williams & Baltensperger, 2009). Dust from artisanal gold mining, industrial mining and uranium mining can contain contaminants such as mercury (Hg), lead (Pb), arsenic (As) and chromium (Cr) (Csavina *et al*., 2012). Coal mine dust contains silica, naphthalene and about 13 polynuclear aromatic hydrocarbons that are carcinogenic (Banerjee *et al.*, 2001).

Motor vehicle emissions are a major source of PM, hydrocarbons, SO_2, carbon monoxide (CO), CO_2 and NO_x, VOCs and photochemical smog (O_3 – reaction of VOCs and NO_x in presence of sunlight) (Tong *et al*., 2011; Schwela *et al*., 1997).

Domestic combustion contributes significantly to the atmospheric aerosol load. Most domestic combustion takes place in developing countries, especially in informal settlements (low income households that erect from any available material), where the needs for cooking, space heating and lightning are not addressed with electricity (Chiloane *et al*., 2017, Pretorius *et al*., 2015; Venter *et al*., 2012; Ludwig *et al*., 2003). Fuels used in household combustion include low grade coal, wood and paraffin (Pretorius *et al*., 2015). Domestic emissions contain a wide range of persistent polycyclic aromatic hydrocarbons, PM, organic pollutants, trace metals and gases (e.g. CO and NO_x) (Lee *et al*., 2005; Ludwig *et al*., 2003).

2.2.2 Size, number and mass concentrations

Atmospheric aerosols exhibit a range of sizes that are determined by formation processes and subsequent chemical and physical reactions (Turner & Colbeck, 2008). The form of aerosol size distribution is dependent on how concentration (i.e. surface area, volume, number or mass per unit volume of air) is expressed (Jacobson, 2002). Therefore, the size distribution can look different if plotted as

number concentration or mass distribution (Turner & Colbeck, 2008; Jacobson, 2002). The number concentration of aerosols decreases with increasing particle size; therefore, particles in small size ranges can be abundant in number, but contribute a small amount of the total mass (mass depends on the cube of diameter) (Turner & Colbeck, 2008); whereas particles in larger sizes contribute more to the total mass, but are less abundant in number. Figure 2-3 illustrates that once particles are airborne, they undergo several chemical and physical transformations that include changes in particle structure, size and composition through chemical reactions, coagulation, condensation and evaporation through activation in the presence of water supersaturation to become cloud droplets and fog, along with aerosol sources and sink processes (Seinfeld & Pandis, 2016; Pöschl, 2005). Aerosol sizes can span from a few nanometres, for new particles produced by nucleation, to tens or hundreds of micrometres, for large particles produced by wind friction on ocean and land surfaces (Boucher, 2015; Williams & Baltensperger, 2009). Aerosol sizes can be divided into two modes, i.e. fine and coarse modes. The fine mode can be further subdivided into nucleation, Aitken and accumulation modes (Boucher, 2015; Williams & Baltensperger, 2009; Turner & Colbeck, 2008; Jacobson, 2002), also illustrated in Figure 2-3. Table 2-1 presents the different modes, size fraction diameters and descriptions of the different modes in more detail.

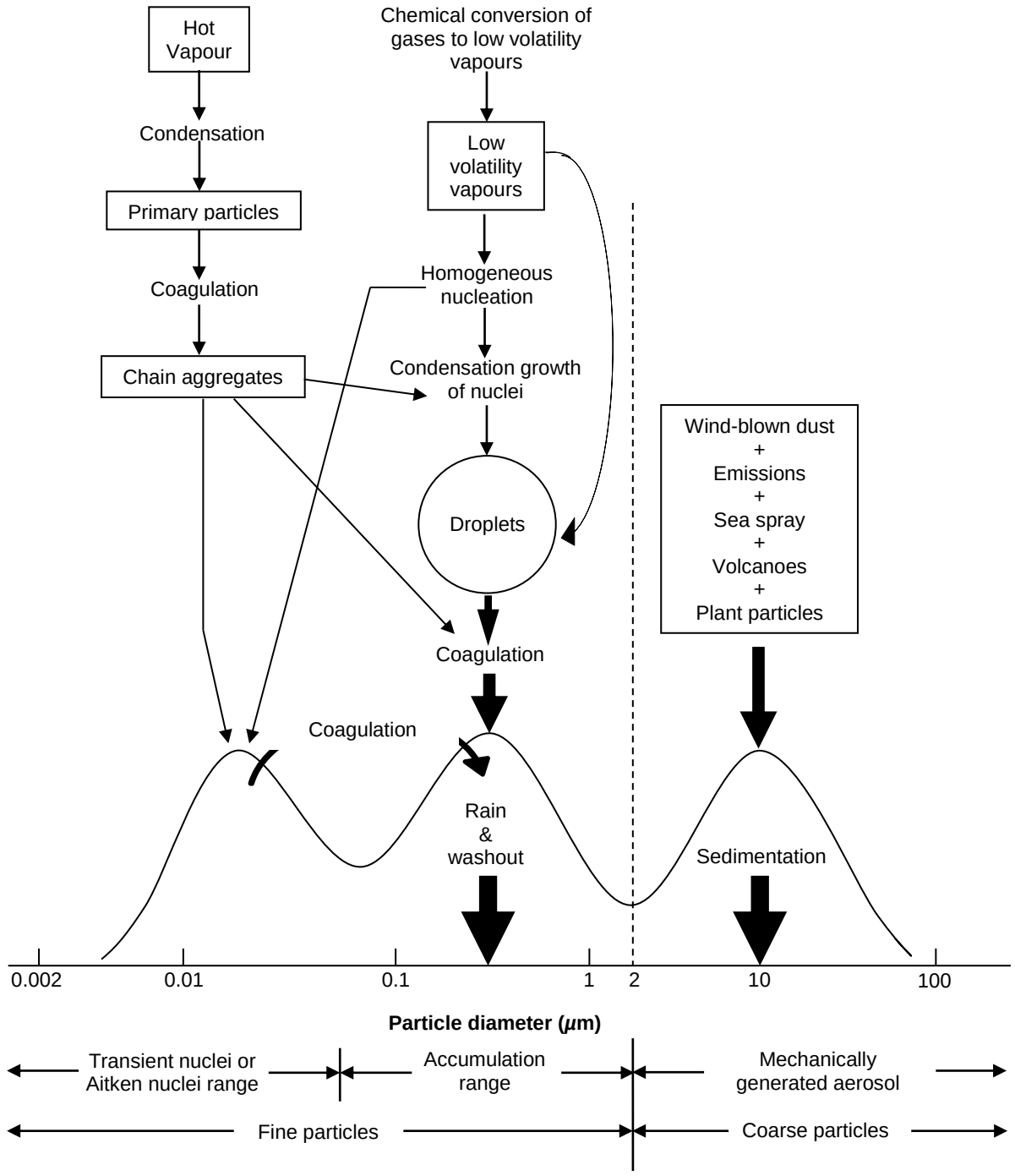

Figure 2-3: A schematic illustration of aerosol formation, processes and removal in the atmosphere (based on Seinfeld & Pandis, 2016)

Table 2-1: Size fraction diameters and description of the different modes (Williams & Baltensperger, 2009; Turner & Colbeck, 2008; Jacobson, 2002; Penner *et al*., 2001)

		Size fraction diameter (µm)	Description
Fine mode	Nucleation mode	≤0.001	Contains emitted particles formed from condensation of hot vapour processes, or newly nucleated particles formed by gas-to-particle conversion. Small emitted or nucleated particles are subject to rapid coagulation and/or condensation of vapours due to their high number concentration.
	Aitken mode	0.01-0.1	
	Accumulation mode	0.1-1	Coagulation and condensation move nucleation and Aitken mode particles to the accumulation mode. Particles in the accumulation mode are the most important and represent a substantial part of the aerosol mass. Accumulation mode particles' mass extinction efficiency is the largest and they have the longest atmospheric lifetime (1 to 2 weeks, as wet and dry deposition is inefficient causing particles to accumulate). These particles also form the majority of CCN. In addition, accumulation mode particles can affect a human health and visibility.
Coarse mode		≥1-2	Coarse mode particles are formed by sea spray, windblown-dust, volcanoes, plants and mechanical abrasion processes and are rapidly removed from the atmosphere within hours to a few days.

2.2.3 Aerosol sink processes

There are two mechanisms by which particles can be removed from the atmosphere, i.e. wet deposition and dry deposition (Figure 2-3). When particles are incorporated

into cloud droplets or ice crystals during the formation of precipitation, it is termed wet deposition (Seinfeld & Pandis, 2016, Pöschl, 2005). This process is the main sink of atmospheric aerosols. Dry deposition occurs when particles are deposited onto the earth's surface without precipitation of airborne water particles, but rather by convective transport, diffusion and adhesion (Pöschl, 2005). This process is less important on a global scale, but relevant in respect to health effects, air quality and soiling to monuments and buildings (Pöschl, 2005).

2.2.4 Health effects of aerosols

Anthropogenic and natural aerosols both have a significant influence on climate and human health. Inhalation of ultrafine particles is hazardous to human health due to their small size (World Health Organization (WHO), 2005; Shiraiwa *et al*., 2017; Pöschl, 2005). They can penetrate the membranes of the thoracic region of the respiratory system and enter the blood stream or can be transported along the olfactory nerves into the brain (Anderson *et al*., 2012; Pöschl, 2005). This can occur by being exposed over both short and long periods. Health effects include allergic diseases, cardiovascular and respiratory morbidity, i.e. aggravation of asthma, respiratory symptoms, as well as mortality from cardiovascular and respiratory diseases and lung cancer (Shiraiwa *et al*., 2017; Anderson *et al*., 2012; Pöschl, 2005). Groups with heart and lung diseases are most susceptible, and elderly people and children are also vulnerable. However, many uncertainties remain regarding differences in health effects of particles with different chemical compositions, or origin (Pöschl, 2005).

2.2.5 Types of aerosols

2.2.5.1 Inorganic aerosols

Ammonium (NH_4^+), SO_4^{2-} and NO_3^- form a large part of inorganic aerosol components in PM (Boucher, 2015; Squizzato *et al*., 2013). Other constituents that are less abundant are calcium sulphate ($CaSO_4$), sodium sulphate (Na_2SO_4), calcium nitrate ($CaNO_3$) and sodium nitrate ($NaNO_3$) (Weijers *et al*., 2010). According to the IPCC (2013) and Penner *et al*. (2001), most inorganic aerosols scatter solar radiation and produce a negative radiative forcing on (cooling effect) the earth (Figure 2-2).

SO_4^{2-} and NO_3^- are formed secondary in the atmosphere through the oxidation of SO_2 and NO_x in the gas or condensed phases, respectively (Weijers *et al*., 2010; Williams & Baltensperger, 2009). SO_2 is emitted by coal-fired power plants, smelters, industrial boiler and oil refineries, and NO_x (NO/NO_2) is emitted mostly from traffic emissions, coal-fired power plants and other industrial activities, as well as open biomass burning (Weijers *et al*., 2010; Williams & Baltensperger, 2009). According to the IPCC fifth assessment report (IPCC, 2013) global SO_2 emissions are average 55.2 Tg yr^{-1}. Ammonia (NH_3) is usually emitted from agricultural activities and, to a lesser extent, from fuel combustion and oil refineries with average emissions of 41.6 Tg yr^{-1} globally (Boucher, 2015; IPCC, 2013; Weijers *et al*., 2010). Ambient SO_4^{2-} and NO_3^- concentrations are not necessarily proportional to precursor gas concentrations, but the formation rate strongly depends on temperature, RH, gaseous precursors, concentrations of atmospheric oxidants and characteristics of pre-existing aerosols (Seinfeld & Pandis, 2016, Squizzato *et al*., 2013; Weijers *et al*., 2010; Pathak *et al*., 2009; Bergin *et al*., 2005, Baek *et al*., 2004). Previous studies indicated that ~50 % of SO_2 and NO_x are oxidised to sulphuric acid (H_2SO_4) and nitric acid (HNO_3), respectively, before being washed-out to the earth's surface (Williams & Baltensperger, 2009; Langner & Rodhe, 1991). The oxidation of SO_2 largely results in the formation of aerosol mass due to low H_2SO_4 vapour pressure, whereas HNO_3 is distributed between the gas and aerosol phases (Williams & Baltensperger, 2009). HNO_3 is removed from the atmosphere through wet and dry deposition and is therefore a major removal mechanism for tropospheric NO_x (Williams & Baltensperger, 2009).

SO_4^{2-} particles can be formed from SO_2 via two paths, i.e. gas-phase or aqueous-phase transformation (Weijers *et al*., 2010; Williams & Baltensperger, 2009). During gas-phase transformation, SO_2 is converted into H_2SO_4 by reacting with the hydroxyl radical ($OH^{\bullet}$), O_2 and small amounts of water vapour (Reactions 2.1-2.3) (Seinfeld & Pandis, 2016; Weijers *et al*., 2010):

$$OH + SO_2 \rightarrow HSO_3 \quad (2.1)$$

$$HSO_3 + O_2 \rightarrow HO_2 + SO_3 \quad (2.2)$$

$$SO_3 + H_2O \rightarrow H_2SO_4 \quad (2.3)$$

The conversion of hydrogen sulphite (HSO_3) to H_2SO_4 is a rapid reaction and the oxidation of SO_2 highly depends on the presence of $OH^{\bullet}$ radicals (Weijers *et al*., 2010; Williams & Baltensperger, 2009). Consequently, H_2SO_4 condenses on pre-existing particles and nucleates in high RH conditions to form H_2SO_4 droplets and in the presence of NH_3 gas neutralised ammonium sulphate ($(NH_4)_2SO_4$) (Reactions 2.4-2.5) (Weijers *et al*., 2010):

$$H_2SO_4 + NH_3 \rightarrow NH_4HSO_4 \quad (2.4)$$

$$NH_4HSO_4 + NH_3 \rightarrow (NH_4)_2SO_4 \quad (2.5)$$

During the aqueous-phase pathway, SO_2 dissolves in a droplet produced by clouds or fog. SO_2 is rapidly oxidised to H_2SO_4 if O_3 and hydrogen peroxide (H_2O_2) are present in the droplet (Weijers *et al*., 2010). When NH_3 is present in the droplet, H_2SO_4 is neutralised to ammonium bisulphate (NH_4HSO_4). The aqueous-phase pathway is faster, if compared to the gas-phase pathway (Weijers *et al*., 2010).

NO_3^- particles are produced from the oxidation of NO_x to form HNO_3 and consequently producing particles as a result of reactions with NH_3 or sodium chloride (NaCl) (Squizzato *et al*., 2013; Weijers *et al*., 2010; Williams & Baltensperger, 2009). During the daytime, NO_x reacts with $OH^{\bullet}$ (Reaction 2.6), which has a higher reaction rate than the SO_2 oxidation by $OH^{\bullet}$ (Reaction 2.1) (Seinfeld & Pandis, 2016; Weijers *et al*., 2010):

$$OH^{\bullet} + NO_2 \rightarrow HNO_3 \quad (2.6)$$

During night-time, NO_2 reacts with O_3 (Reactions 2.7-2.9), due to lower $OH^{\bullet}$ concentrations (Seinfeld & Pandis, 2016; Weijers *et al*., 2010) to form the nitrate radical ($NO_3^{\bullet}$):

$$O_3 + NO_2 \rightarrow NO_3^{\bullet} + O_2 \quad (2.7)$$

$$NO_2 + NO_3^{\bullet} \rightarrow N_2O_5 \quad (2.8)$$

$$N_2O_5 + H_2O \rightarrow 2\ HNO_3 \quad (2.9)$$

NH_3 reacts reversibly with HNO_3 to form NH_4NO_3 (Reaction 2.10):

$$NH_3 + HNO_3 \leftrightarrow NH_4NO_3 \quad (2.10)$$

NH_4NO_3 is semi-volatile and the backwards reaction (Reaction 2.10) is advanced during conditions of low atmospheric NH_3 concentrations, or high temperatures (Weijers *et al*., 2010; Worobiec *et al.,* 2003; Claes *et al*., 1998). Therefore, NH_4NO_3 concentrations are often higher during night-time and the colder season (Weijers *et al*., 2010; Ten Brink *et al*., 2007; Pun & Seigneur, 2001).

In coastal and marine regions, HNO_3 reacts with sea salt particles to form $NaNO_3$ and HCl (Reaction 2.11) (Weijers *et al*., 2010):

$$NaCl + HNO_3 \rightarrow NaNO_3 + HCl \quad (2.11)$$

HNO_3 is also easily absorbed onto dust particles, and forms stable products such as magnesium nitrate ($Mg(NO_3)_2$) and calcium nitrate ($Ca(NO_3)_2$) (Reactions 2.12-2.13) (Weijers *et al*., 2010):

$$MgCl_2 + 2\ HNO_3 \rightarrow Mg(NO_3)_2 + 2\ HCl \quad (2.12)$$

$$CaCO_3 + 2\ HNO_3 \rightarrow Ca(NO_3)_2 + H_2O \quad (2.13)$$

The chemical transformations of SO_2 to SO_4^{2-} particles and NO_x to NO_3^- particles compete with one another for the available $OH^\bullet$ radicals and NH_3 (Seinfeld & Pandis, 2016; Weijers *et al*., 2010; Williams & Baltensperger, 2009). The neutralisation of H_2SO_4 is generally favoured over the neutralisation of HNO_3, and NH_4NO_3 will only form when the total NH_3 exceeds the SO_4^{2-} by a factor of two or more on a mole basis (Seinfeld & Pandis, 2016; Squizzato *et al*., 2013; Weijers *et al*., 2010).

2.2.5.2 Aerosol black carbon

BC can be described as a carbonaceous fraction of PM that absorbs incoming shortwave solar radiation and longwave terrestrial radiation, which has a positive radiative forcing (warming effect) on the earth (Bond *et al*., 2013; IPCC, 2013) (Figure 2-2). Once airborne, BC undergoes regional and intercontinental transport and is removed from the atmosphere by means of wet and dry deposition, resulting in a lifetime of a few days to weeks (Bond *et al*., 2013). In addition to absorption, BC can also affect the earth's radiative forcing by influencing cloud formation and

snow/ice albedo (Wang, 2015; Bond *et al.*, 2013). BC has the ability to act as effective cloud condensation nuclei (CCN) and ice nuclei (IN) and consequently increases the cloud reflectivity, enhances precipitation in mixed-phased clouds and changes the number of liquid cloud droplets, ice particles and cloud extent (Wang, 2015; Bond *et al.*, 2013). Furthermore, deposition of BC on snow/ice decreases the reflectivity, thereby increasing the ability of the surface to absorb solar radiation that leads to a positive radiative forcing on the earth (Wang, 2015; Bond *et al*., 2013; Ramanathan & Carmichael, 2008). This process causes the snow/ice cover to melt (Wang, 2015). Shindell *et al*. (2008) estimated that more than half of the observed Arctic warming, since 1890, is due to the contribution of BC, and therefore BC is considered to be the second most important contributor to global warming after CO_2 (IPCC, 2013; Bond *et al*., 2004). In addition, BC contributes significantly to fine PM (~90 % fraction of $PM_{2.5}$) in the atmosphere, which can have harmful human health effects (IPCC, 2013; Sahu *et al*., 2011, Lighty *et al*., 2000).

BC is a primary aerosol that is directly emitted into the atmosphere. It is produced during incomplete combustion (lack of O_2) of long-chain fuels, i.e. fossil and biomass fuel combustion, diesel engine exhausts, open biomass burning and domestic combustion (Bond *et al*., 2013; IPCC, 2013). The largest global sources of BC are from forest and savannah open biomass burning (Bond *et al*., 2013). Nevertheless, domestic solid fuels (e.g. biomass and coal) contribute 60 to 80 % of African and Asian emissions, while diesel engines contribute ~70 % of emissions in North America, Europe and Latin America (Bond *et al*., 2013). BC contributions to the radiative budget from open biomass burning, fossil fuels and biofuel are ~42 %, ~38 % and ~20 %, respectively (Sahu *et al*., 2011; Bond *et al*., 2004). According to the fifth assessment report for IPCC (IPCC, 2013), the total emissions for BC is 10.5 Tg yr^{-1} globally. During the formation of BC, polycyclic aromatic hydrocarbons that are produced during combustion form precursors for BC (Bond *et al*., 2013). The precursors coagulate to larger sizes to serve as small spherical particle nuclei of tens of nanometres with graphite layers and a high C:H ratios, and then consequently coagulate to form a BC chain (Boucher, 2015; Bond *et al*., 2013). SO_4^{2-} and OC can condense as a coating on the BC surface, which creates an internal mixture that can alter the microphysical and optical properties of BC (Boucher, 2015).

2.2.5.3 Organic aerosol

Atmospheric aerosols contain thousands of organic compounds with different chemical and physical properties (Goldstein & Galbally 2007). OA contributes significantly to the total aerosol mass, e.g. the organic fraction of aerosols in urban air mostly contribute 30 to 60 % of the total fine PM in the atmosphere and have a substantial impact on atmospheric aerosol properties (Lazaridis, 2008). OA can be described as carbon-containing compounds that are combined with other inorganic chemical components such as H_2 and O_2 (Bond *et al*., 2013; Lazaridis, 2008). Examples of the latter include alkanes, alkenes, amines, alcohols, aromatic compounds, organosulphurated compounds, carbonylated compounds and organic acids (Boucher, 2015). Although the existence of organic components has been known for many years, methods still provide limited information on the actual character of individual organic compounds (Boucher, 2015; Pöschl, 2005). The carbonaceous fraction of OA consists of elemental carbon (also called BC) and OC (Seinfeld & Pandis, 2016; Lazaridis, 2008; Jacobson *et al*., 2000). OC is referred to as the carbon mass within OA, which excludes the H_2 and O_2 content. In addition, organic compounds usually form a layer on the surface of the elemental carbon fraction, and therefore tend to scatter incoming solar radiation (Figure 2-3). Generally, it is difficult to completely separate elemental carbon from OC, although OA can exist independently from elemental carbon (Jacobson *et al*., 2000).

The chemical composition of OA originating from open biomass burning differs from OA originating from the combustion of fossil fuel hydrocarbons (Boucher, 2015). The C:O ratio in OA can be used to indicate the chemical composition (Boucher, 2015). In oxygenated OA (containing O_2-rich compounds), the ratio is 0.25 and has higher values up to 1 for more aged OA. As OA ages in the atmosphere, they become more oxygenated, hygroscopic and less volatile (Boucher, 2015; Jimenez *et al*., 2009). Organic compounds enter the atmosphere by primary emissions, which are of natural (e.g. biogenic emissions and plant matter debris) and anthropogenic (e.g. fossil fuel, open biomass burning, domestic burning, as well as direct injection of unburnt fuel and lubricants) origin, as primary organic aerosols (POA) from terrestrial and marine environments (Seinfeld & Pandis, 2016; Facchini *et al*., 2010; Jacobson *et al*., 2000). POA comprises large complex mixtures of gas, i.e. VOCs, and particle

(OA) phase species, where they continuously evolve in the atmosphere through reversible phase partitioning, wet and dry deposition and chemical reactions with $OH^{\bullet}$ (during daytime) and $NO_3^{\bullet}$ (during night-time) (Lazaridis, 2008; Atkinson & Arey, 2003; Jacobson *et al*., 2000). Reactions of the latter are associated with the production of tropospheric ozone (O_3), oxygenated VOCs and secondary organic aerosols (SOA) (Crippa *et al*., 2013; Jacobson *et al*., 2000). SOA can be formed by chemical reactions of gas-phase compounds through different paths (Ervens *et al*., 2011). These paths include:

- NPF, which involves gas-phase reactions of VOCs that result in the formation of semi-volatile organic compounds (SVOCs) from which new aerosols are formed,

- gas-particle partitioning, which involves the formation of SVOCs through gas-phase reactions and absorption by pre-existing particles, and

- heterogeneous multiphase reactions between low volatility or non-VOCs with VOCs and SVOCs on the surface or in the bulk of aerosols or cloud particles.

According to Schulze *et al*. (2017), SOA is dominated by oxidation of biogenic VOCs, globally. SOA formation depends on various parameters, which include temperature, RH and the concentrations of inorganic and organic condensing and nucleating vapours that depend on local sources and sinks, i.e. photochemistry and pre-existing aerosol or cloud particles, as well as atmospheric transport (Seinfeld & Pandis, 2016; Kamens & Jaoui, 2001).

2.2.6 Aerosol effects on climate

Aerosol effects on climate can be classified as direct or indirect, with respect to the radiative forcing. Figure 2-4 presents a summary of the distinction between the direct and indirect effects and major feedback loops in the climate system (Pöschl, 2005). The direct effect involves the scattering and absorption of solar radiation, whereas the indirect effect involves CCN and IN activity. The direct and indirect effects will be discussed in more detail in the following sections. From Figure 2-4, the direct and indirect effects are determined by the aerosol structure, particle size and chemical composition, and therefore are strongly influenced by the atmospheric processes

such as chemical transformation, coagulation and water interactions (Pöschl, 2005). The feedback loops (Figure 2-4) illustrate that atmospheric aerosols interact with solar (shortwave) and terrestrial (longwave) radiation, precipitation and clouds, hydrological cycle and general circulation of the atmosphere, as well as natural and anthropogenic aerosols, and trace gas sources on regional and global scale (Pöschl, 2005). The processes in Figure 2-4 involve physicochemical processes, which depend on the meteorological environment and atmospheric composition and are largely not quantitatively characterised; therefore, a high uncertainty arises in the actual climate system responses and feedback to natural and anthropogenic perturbations (Pöschl, 2005).

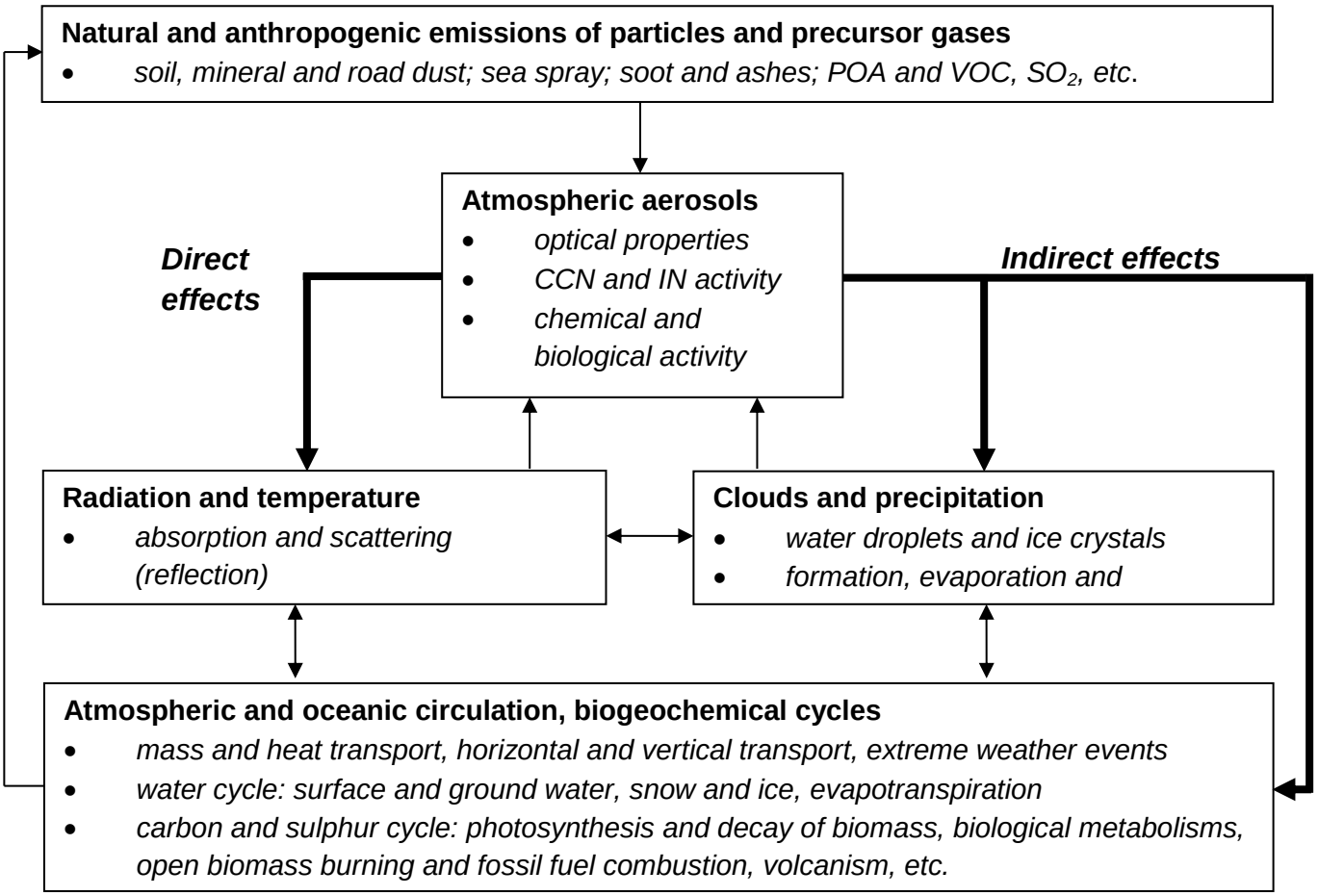

Figure 2-4: The direct and indirect effect of aerosols and major feedback loop in the climate system (based on Pöschl, 2005)

2.2.6.1 Direct effects

Figure 2-5 presents a schematic illustration of aerosols, radiation and clouds (Boucher, 2015). Aerosols can directly influence the climate by the scattering and absorption of solar (shortwave) and terrestrial (longwave) radiation. The scattering process involves the anisotropic interaction of solar and terrestrial radiation with aerosols that are refracted in all directions. The amount of radiation scattered back to space determines the magnitude of the direct forcing of aerosols at a specific location and time, which leads to a reduction of incoming solar radiation at the earth's surface, and loss of energy and cooling of the climate system (Seinfeld & Pandis, 2016, Boucher, 2015). The scattering itself depends on abundance, size and optical properties of the particles and the solar zenith angle (Seinfeld & Pandis, 2016). In contrast, absorption is when solar radiation is absorbed, thereby electromagnetic energy being transformed into heat (Boucher, 2015; IPCC, 2013). During absorption of solar radiation, the aerosol layer heats up and there is also a reduction of incoming solar radiation at the earth's surface (Boucher, 2015; IPCC, 2013). Aerosols that absorb solar radiation can also modify the vertical temperature profile, which impacts the RH and atmospheric stability, and therefore influences cloud formation (Boucher, 2015; IPCC, 2013). This effect is called aerosol semi-direct effect.

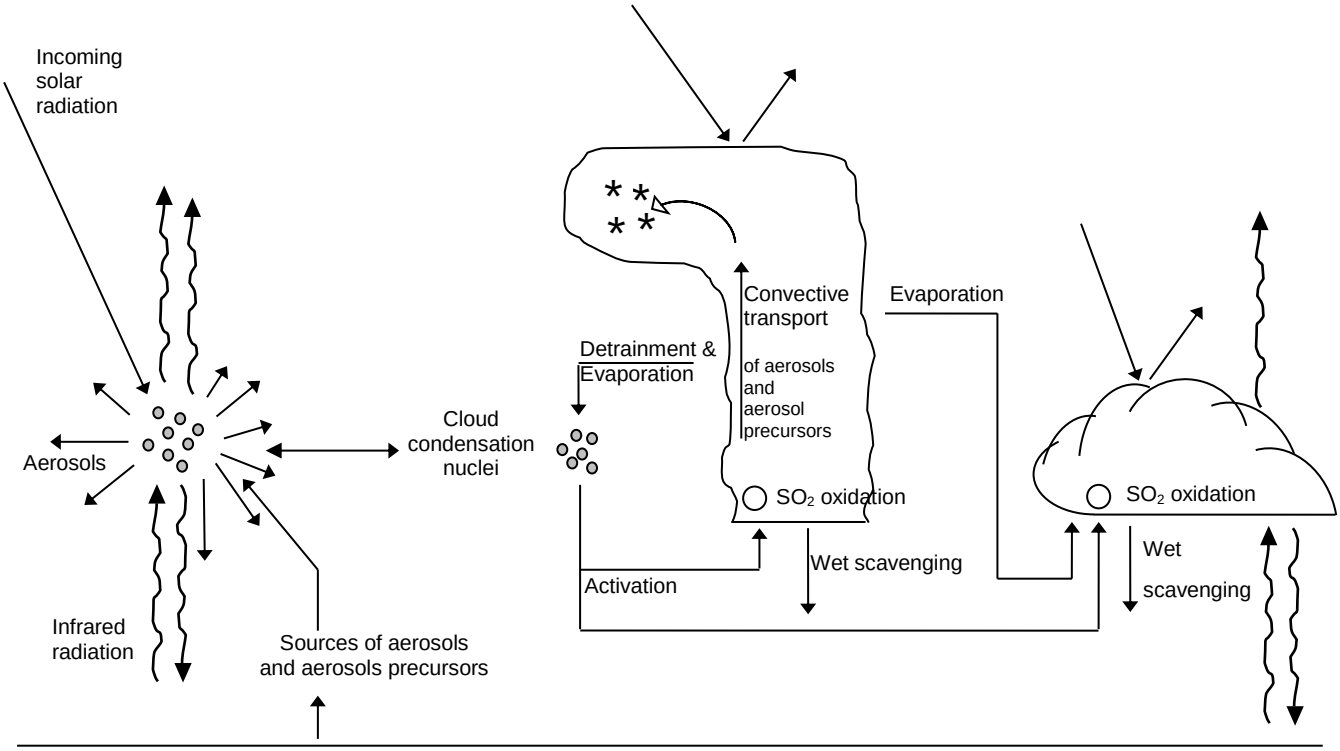

Figure 2-5: A schematic illustration of aerosol-radiation-cloud interactions (based on Boucher, 2015)

2.2.6.2 Indirect effects

The indirect effect of aerosols on the climate are more complex than the direct effect due to the dependence of many phenomena concerning aerosols, such as concentrations of CCN, ratio of CCN concentrations to cloud droplet number concentrations (and size), and cloud albedo and lifetime (Seinfeld & Pandis, 2016). A schematic illustration of the indirect effect is presented in Figure 2-5. Aerosols can affect the climate system by influencing the microphysical and optical properties of liquid and ice clouds, through CCN and IN activity, or by chemical and biological activity (influence on aerosol and trace gas emissions and transformation) (Boucher, 2015; Pöschl, 2005). CCN activity is the process where water vapour condenses, which controls the concentration and size population of cloud water droplets (Boucher, 2015). The degree of acidity of the cloud, as well as the rate of some chemical reactions in the droplet, can be determined and controlled by the chemical composition of the aerosol (Boucher, 2015; IPCC, 2013). Variations in number concentration of aerosols can cause changes in the population and sizes of cloud droplets and can lead to changes in cloud albedo (Seinfeld & Pandis, 2016; Boucher,

2015,). IN activity is when aerosols act as IN that favour the formation of the ice phase (Boucher, 2015; IPCC, 2013). Aerosols can also influence the properties of mixed-phase clouds, i.e. clouds that contain liquid droplets and ice crystals (Boucher, 2015; IPCC, 2013). The formation and properties of liquid water, ice and mixed-phase clouds and precipitation can be affected by an increase in CCN and IN in the atmosphere. Such effects are the cloud albedo effect (smaller cloud particles reflect more solar radiation), the cloud lifetime effect (precipitation efficiency is decreased by smaller cloud particles), the thermodynamic effect (the onset of freezing is delayed by smaller cloud droplets) and the glaciation effect (the precipitation efficiency is increased by more IN) (Pöschl, 2005). These and other related effects of aerosol, cloud, precipitation and radiation interactions influence the global and regional radiative forcing, hydrological cycle, temperature and general circulation of the atmosphere and ocean (Pöschl, 2005).

2.3 Aerosols in southern Africa

2.3.1 Aerosol sources

Africa is an important source region for numerous gas and aerosol species, but it is one of the least studied continents (Boko *et al*., 2007), possibly since most African countries can be regarded as developing (lacking resources). Southern Africa is an important sub-source region, with especially open biomass burning being a major concern due to its general air quality, health, visibility and climate impacts. Open biomass burning in this region includes grassland, savannah and forest fires, as well as agricultural burning, which combined produce significant amounts of aerosols especially in the dry season (Mafusire *et al*., 2016; Vakkari *et al*., 2014, 2018; Queface *et al*., 2011; Eck *et al*., 2003; Swap *et al*., 2003). Domestic combustion (i.e. cooking and domestic space heating) also contributes significantly to the atmospheric aerosol load, especially near informal settlements (low income households that erect housing from any available material) (Chiloane *et al*., 2017; Hersey *et al*., 2015; Venter *et al*., 2012). Within southern Africa, South Africa is by far the largest economy, with numerous sources (e.g. industries and an aged vehicle fleet, if compared to first-world countries) that emit aerosols as primary pollutants. Secondary formed aerosols are also very prevalent, with, for instance, regional NPF

frequencies measured in the South African interior being the highest ever recorded internationally (Nieminen *et al*., 2018). Major anthropogenic point sources in South Africa include an array of very large coal-fired power stations and petrochemical operations that do not de-SO_x or de-NO_x their off-gas (Pretorius *et al*., 2015; Lourens *et al*., 2011), and large mining and pyro-metallurgical industries (e.g. Loock-Hattingh *et al*., 2015; Venter *et al*., 2012; Hirsikko *et al*., 2012).

2.3.2 Studies of aerosol optical properties in South Africa

Only a few papers have been published on aerosol optical properties, where mostly vertical and/or remote sensing techniques were used to obtain aerosol optical data (Kumar *et al*., 2014; Queface *et al*., 2011; Campbell *et al*., 2003; Eck *et al*., 2003; McGill *et al*., 2003; Swap *et al*., 2003; Formenti *et al*., 2002; Diner *et al*., 2001). Some of these papers mostly focused only on measurements during open biomass burning periods (Campbell *et al*., 2003; Eck *et al*., 2003; McGill *et al*., 2003; Swap *et al*., 2003; Diner *et al*., 2001) and were generally based on short measurement periods during the Southern African Regional Science Initiative (SAFARI) 2000 campaign (Swap *et al*., 2003). As far as the candidate could assess, the paper published by Laakso *et al*. (2012) is the only study to date where ground-level, longer-term (in this case 2 years) aerosol optical properties, based on *in situ* aerosol scattering and absorption measurements in South Africa, have been published. Although this paper made a significant contribution, it was a general paper that considered various gas and aerosol measurements and therefore did not focus specifically on explaining observed aerosol optical phenomena in detail. Furthermore, no diurnal patterns were presented and possible source explanations were quite general. In addition, the optical data, presented by Laakso *et al*. (2012) mostly only represent measurements in the internationally well-known NO_2 hotspot, visible with satellite observations (Lourens *et al*., 2012). In South Africa, the Cape Point Global Atmosphere Watch (GAW) station (Slemr *et al*., 2015; Venter *et al*., 2015; Slemr *et al*., 2013) also measures ground-level *in situ* aerosol absorption and scattering on a long-term basis; however, no results have yet been published.

According to the fifth assessment of the IPCC (IPCC, 2013), the southern hemisphere remains under reported and large uncertainties are still associated with

aerosols and their optical properties. While ground-based in-situ measurements have been reported on in the Highveld Priority Area in southern Africa and unpublished results, available from the Cape Point GAW station – that is representative of an oceanic southern hemispheric background site – a knowledge gap still persists in the interior of southern Africa. To at least partially address this knowledge gap, this study has envisioned investigating the various aerosol optical properties in order to present results representative of the interior of South Africa.

2.3.3 Meteorology in the South African interior

Meteorology in the South African interior is characterised by a strong seasonal variability. Over the eastern interior of South Africa, the atmospheric circulation pattern is dominated by anti-cyclonic circulation during the winter months and experiences regular easterly disturbances during the summer months (Garstang *et al*., 1996; Laakso *et al*., 2012). Pollutants can get trapped in the anti-cyclonic circulation over South Africa for several days to weeks before exiting, primarily towards the east-coast in a well-defined plume (Laakso *et al*., 2012; Freiman & Piketh, 2002; Piketh *et al*., 2000; Garstang *et al*., 1996). Westerly disturbances occur ~20 % of the time throughout the year (Garstang *et al*., 1996; Laakso *et al*., 2012). Precipitation in the South African interior is characterised by strong seasonal variation and typically begins in middle October and ends in April (wet season). Local pollutant concentrations are affected by the precipitation cycle through wet scavenging during the wet season (Laakso *et al*., 2012). The dry months (May to mid-October) have almost no precipitation and pollutant levels increase due to large-scale open biomass burning. During the dry winter months and early spring months, inversion layers form at various altitudes (Garstang *et al*., 1996; Tyson *et al*., 1996; Tyson & Preston-Whyte, 2000) and the PBL depth is also shallower (Korhonen *et al*., 2014, Gierens *et al*., 2019). The inversion layers are created by a combination of a high pressure system (that is created by high altitude and subtropical subsidence) and low heat capacity of soil (Garstang *et al*., 1996). This layered atmospheric structure reduces vertical mixing and influences atmospheric pollutant concentrations significantly. In the presence of sunlight, the inversion layers break down through convective heating and the mixed layer height increases (Tyson *et al*., 1996; Korhonen *et al*., 2014; Gierens *et al*., 2019).

2.4 Aerosol optical properties

2.4.1 Scattering and absorption coefficient

Scattering coefficient (σ_{SP}) can be defined as the fraction of incident radiant energy removed by scattering per length of travel of radiation through a substance (Chin *et al*., 2009). Aerosol scattering and hemispheric backscattering at one or multiple wavelengths can be measured with an integrating nephelometer (Ramachandran, 2018; Anderson *et al*., 1996). The light scattered by aerosols is typically measured in a 0 to 180 ° angle range (Ramachandran, 2018, Heintzenberg and Wiedensohler, 2006). However, some systematic limitations were discovered involving full range coverage of scattering angles, i.e. light scattered at angles ~7° - ~170° is neglected that lead to an underestimation of the scattering coefficient, which is called truncation errors (Anderson *et al*., 1996). Literature (e.g. Anderson and Ogren, 1998, Massoli *et al.*, 2009; Bond *et al*., 2009; Müller *et al*., 2011) presented a correction for the truncation errors. The Beer-Lambert law is used to calculate scattering coefficients (Eq. 2.14) (Ramachandran, 2018, Anderson *et al*., 1996):

$$I = I_0 exp(-\sigma x) \tag{2.14}$$

where I is the intensity of light, I_0 is the intensity of the source, x the thickness of the medium through which the light passes and σ is the extinction coefficient (scattering and absorption coefficient) (Ramachandran, 2018).

In contrast to the scattering coefficient, the absorption coefficient (σ_{AP}) can be described as the fraction of incident radiant energy removed by absorption per length of travel of radiation through the substance (Chin *et al*., 2009). The attenuation of a beam of light is typically measured when it is transmitted through a sample. Examples of instruments that use this technique are the aethalometer (Hansen *et al.*, 1984), particle soot absorption photometer (PSAP) (eg. Bond *et al.*, 1999), and multi-angle absorption photometer (MAAP) (Petzold *et al.*, 2002; Petzold and Schönlinner, 2004). In this study, the MAAP was used to determine the absorption of aerosols. The measurement of BC is the most efficient light absorbing aerosol in the visible spectral range and is therefore strongly correlated (Petzold and Schönlinner; 2004). Thus, the relationship between the σ_{AP} and the corresponding BC mass

concentration c_{BC} is recognised by an aerosol mass-specific absorption coefficient $b_{(AP)}^{(BC)}$ given in Eq. 2.15 (Hyvärinen *et al*., 2013; Petzold and Schönlinner; 2004):

$$\sigma_{AP} = c_{(BC)} b_{(AP)}^{(BC)} \tag{2.15}$$

However, BC cannot be unambiguously measured with the above-mentioned measuring instruments due to a variety of aerosol mass-specific absorption coefficient values reported and is usually referred to equivalent BC (eBC) (Petzold and Schönlinner; 2004). Petzold and Schönlinner (2004) gave an elaborated description of the measurement of the absorption coefficient using a MAAP. A radiative transfer scheme is used to model radiative processes for the particle-loaded filter, aerosol filter layer alone, and the blank filter alone (Hyvärinen *et al*., 2013; Hänel, 1987). In addition to the transmission measurements, signals of scattered light to angles 165 and 130 are also measured (Hyvärinen *et al*., 2013). Consequently, the optical depth (τ_{fllter}) and the single scattering albedo (ω_{filter}) of the aerosol loaded filter match the measured reflected and transmitted signals (Hyvärinen *et al*., 2013; Hänel, 1987). With these values the σ_{AP} can be calculated by using Beer-Lambert law relationships (Eq. 2.16) (Ramachandran, 2018; Hyvärinen *et al*., 2013; Petzold, et al., 2005):

$$\sigma_{AP} = -\frac{A}{V}\left(1 - \omega_{filter}\right) \times \tau_{filter} \tag{2.16}$$

where A is the filter spot area and V the sampled volume. The incremental increase in σ_{AP} during time interval $t_i - t_{i-1}$ is given in Eq. 2.17, since the values of τ_{fllter} and ω_{filter} at given time always refer to the initial values of a filter free of any particles (Hyvärinen *et al*., 2013; Petzold, 2005):

$$\sigma_{AP}(t_i) = -\frac{A}{V}[(1 - \omega_{filter}(t_1)) \times \tau_{filter}(t_i) - \left(1 - \omega_{filter}(t_i - 1)\right) \times \tau_{filter}(t_i - 1)] \tag{2.17}$$

The scattering and absorption coefficients have dimensions of cross-sectional area per unit volume such as $m^2\ m^{-3}$, which is reported as inverse meters (m^{-1}) or inverse mega meters such as $M\ m^{-1}$.

2.4.2 Single scattering albedo

The single scattering albedo (ω_0) of an aerosol can be used to describe its radiative effect (Di Biagio *et al*., 2016; Montilla *et al*., 2011). ω_0, at a certain wavelength, may be defined as the fraction of light that is scattered with respect to the total amount of light that is extinct due to the absorption and scattering of an aerosol (Eq. 2.18) (Montilla *et al*., 2011):

$$\omega_0 = \frac{\sigma_{SP}}{\sigma_{SP}+\sigma_{AP}} \tag{2.18}$$

where σ_{SP} is the scattering coefficient and σ_{AP} the absorption coefficient. The ω_0 is a dimensionless quantity with values varying between 0 and 1. If $\omega_0 = 0$, scattering is purely due to absorption of light, warming the atmosphere, whereas if $\omega_0 = 1$, scattering takes place purely in the form of reflection, resulting in a cooling effect (Montilla *et al*., 2011). The ω_0 is dependent on the radiation wavelength that is observed, having, in general, higher values at shorter wavelengths (Di Biagio *et al*., 2016).

2.4.3 Angström exponent of scattering

Angström exponent of scattering (α_{SP}) represents the wavelength dependence of aerosol scattering (Eq. 2.19), which can be derived from the primary measurements of σ_{SP}, by σ_{SP}, $\approx \lambda^{-\alpha SP}$ as a function of wavelength (λ) (Ramachandran, 2018; Seinfeld & Pandis, 2016):

$$\alpha_{SP} = -\frac{d\log\sigma_{SP}}{d\log\lambda} \cong -\frac{\log\left(\sigma_{sp1}/\sigma_{sp2}\right)}{\log(\lambda_1/\lambda_2)} \tag{2.19}$$

α_{SP} can be used as an indication of aerosol sizes that can contribute to aerosol scattering, where small α_{SP} values (<1) indicate larger/coarse particles (radii >~ 0.5 µm) in scattering, and higher α_{SP} values (>1) indicate small/fine particles (radii <~ 0.5 µm) (Ramachandran, 2018; Ångström, 1929).

Chapter 3

Measurement site location and techniques, data processing and analysis

In this chapter, the measurement site location, source areas, biomes and population density of South Africa are presented in section 3.1, while measurement instrumentation is presented in section 3.2. Thereafter, general data processing and data analysis are described in sections 3.3 and 3.4, respectively.

3.1 Site location

Atmospheric measurements were conducted at the Welgegund measurement station (26°34'11.23"S, 26°56'21.44"E, 1480 m above sea level, www.welgegund.org) situated approximately 100 km west of Johannesburg, as indicated in Figure 3-1 (black star). The biomes of South Africa are also presented in Figure 3-1. Welgegund is located on a commercial farm, and is surrounded by grazed grassland and semi-savannah, as well as cultivated farmlands. Temperatures at the site are moderate, with dry winters and precipitation occurring mainly in the spring and summer months (Jaars *et al.*, 2018; Tiitta *et al.*, 2014). Welgegund can be considered as representative of the regional background of the interior of South Africa as there are no significant anthropogenic pollution sources nearby and most of the large point sources are situated in the sector between north to south-east from Welgegund (indicated in the zoomed-in map in Figure 3-1). However, aged air masses that had passed over the industrialised source areas also occasionally impact Welgegund. These source areas include:

- The Johannesburg-Pretoria megacity conurbation with more than 10 million people, indicated in the population density map in Figure 3-2 (Lourens *et al*., 2012).

- The western Bushveld Complex that hosts more than 11 pyrometallurgical smelters in less than a 60 km radius (Hirsikko *et al*., 2012). The western

Bushveld Complex holds most of the world's platinum group metals (PGMs) and a significant fraction of chromium. The area wherein it lies has also recently been declared as part of the Waterberg Priority Area (Department of Environmental Affairs, 2012).

- The eastern Bushveld Complex that also hosts a number of pyrometallurgical smelters.

- The Mpumalanga Highveld, where 11 coal-fired power stations, a very large petrochemical producer and several pyrometallurgical smelters are located in a small geographical area (Lourens *et al*., 2011; Collet *et al*., 2010). This area and part of the Gauteng Province were declared as the Highveld Priority Area in 2007 (Department of Environmental Affairs, 2007).

- The Vaal Triangle Area that host several chemical and petrochemical operations, a couple of pyrometallurgical smelters and a coal-fired power station. This area and the southern Gauteng Province were declared as the Vaal Triangle Airshed Priority Area (Department of Environmental Affairs, 2005).

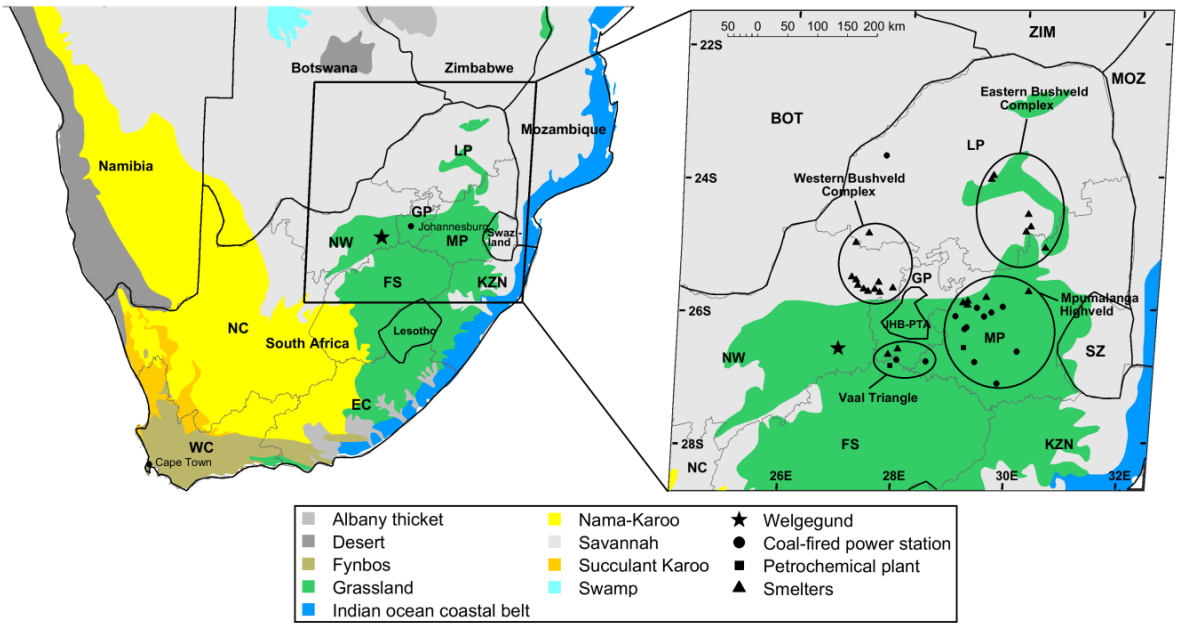

Figure 3-1: Southern African map indicating the location of Welgegund within context of vegetation types (Mucina & Rutherford, 2006), major point sources in the interior of South Africa and the Johannesburg-Pretoria megacity. Province abbreviations: WC – Western Cape, NC – Northern Cape, EC – Eastern Cape, FS – Free State, NW – North West, GP – Gauteng Province, LP – Limpopo Province, MP – Mpumalanga Province, KZN – KwaZulu-Natal

It is evident from the population density map (Figure 3-2) that human activities increase to the east of Welgegund with significantly lower density to the west. Therefore, the western sector of Welgegund can be considered as a relatively clean background sector. Figure 3-3 presents a photo of the Welgegund measurement station.

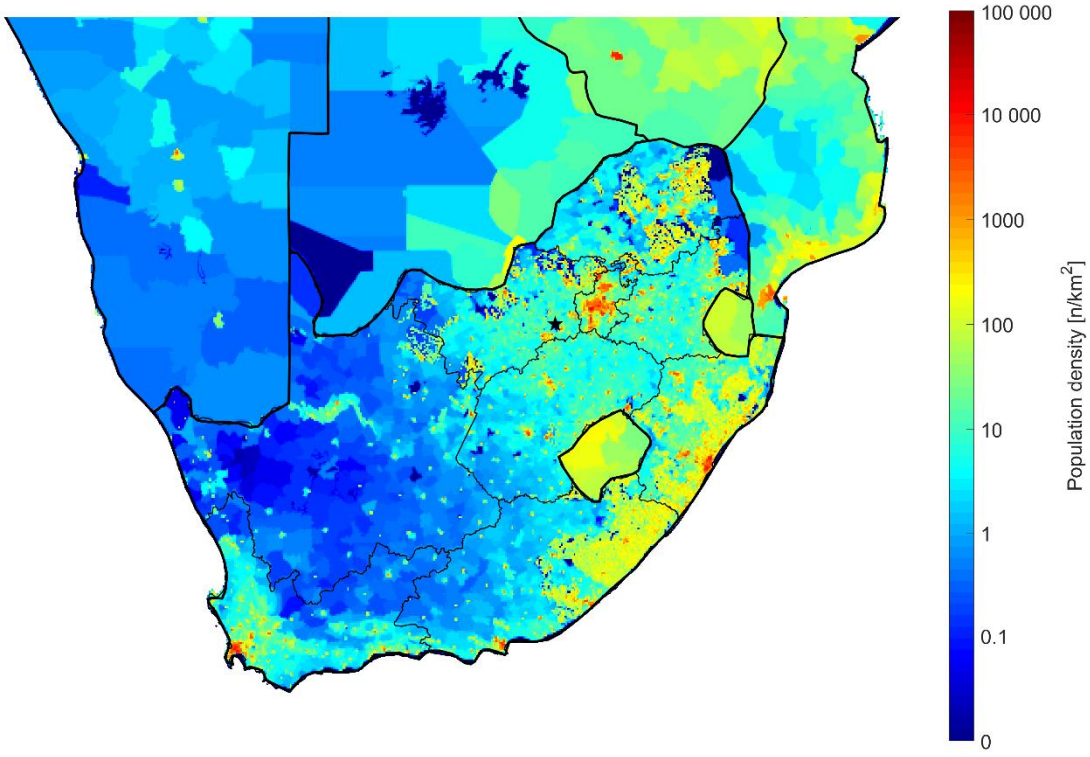

Figure 3-2: The population density for southern Africa (CIESIN, 2010) with Welgegund indicated as the black star

Figure 3-3: Welgegund measurement station situated on grazed land

As previously indicated in section 2.3.3, anti-cyclonic recirculation of air masses is a prominent feature over the interior of South Africa, which can be observed in an overlay back trajectory (see section 3.4.2 for details of air mass history simulations) map for Welgegund in Figure 3-4. The area over which anti-cyclonic recirculation of air masses occurs, as observed from Welgegund, can be considered as a separate 'source area', in addition to the previously mentioned source areas (e.g. Johannesburg-Pretoria megacity, western Bushveld Complex, Mpumalanga Highveld and Vaal Triangle area), since the composition of these air masses will differ from air masses that had passed over the other source areas. Air mass history analysis will be described in later sections.

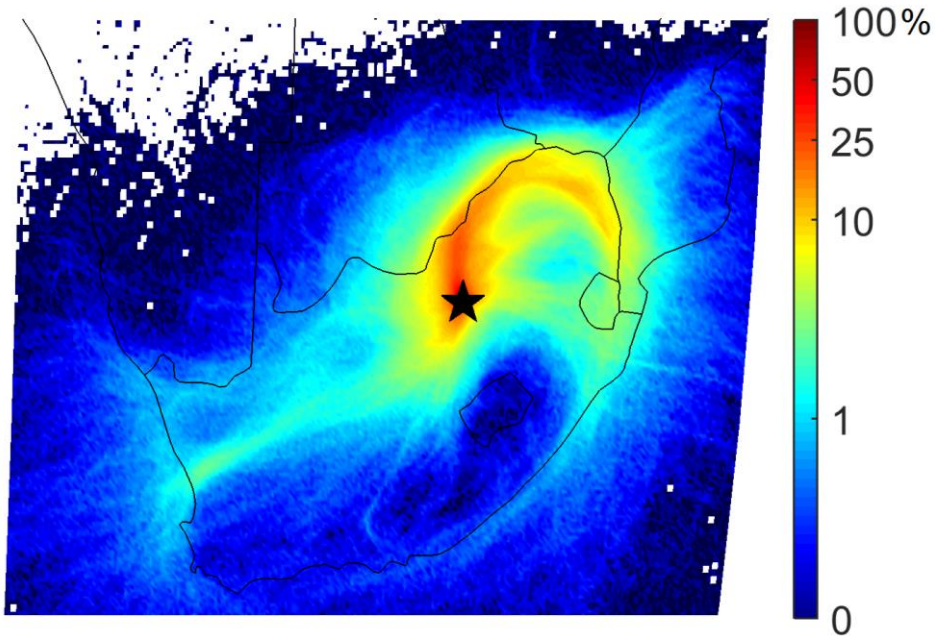

Figure 3-4: Overlay back trajectory map of 96-hour backward trajectories arriving hourly at Welgegund at a 100 m arrival height for the entire measurement period (September 2011 to November 2016)

3.2 Measurement instrumentation

3.2.1 Aerosol measurements

The 3-wavelength nephelometer, MAAP and SHARP instruments were connected to an inlet drier (nafion, below 40 % relative humidity) to avoid hygroscopic growth of particles and condensation. Particles larger than 10 µm were excluded with a PM_{10} inlet and the incoming airflow was split between the MAAP, nephelometer and SHARP.

3.2.1.1 Scattering

The light scattering was measured with a 3-wavelength nephelometer (Ecotech Aurora 3000) at 450, 525 and 635 nm (Figure 3-5). The nephelometer calibration was checked once a week with a HEPA filter (zero) and CO_2 (span). If the instrument response was more than 10 % off, a full calibration was conducted. Between calibrations, the readings were corrected for span and zero drift assuming that the drift is linear between calibration checks.

Figure 3-5: 3-wavelength nephelometer (Ecotech Aurora 3000) instrument

3.2.1.1 Absorption

Light absorption was measured with a multi-angle absorption photometer (MAAP) (model 5012 Thermo Fisher Scientific Inc.) (Figure 3-6) at a wavelength of 637 nm. The MAAP measures light absorption, but reports equivalent black carbon (eBC) (definitions according to Petzold *et al*., 2013) concentrations by using the absorption mass efficiency 6.6 m^2g^{-1}. By multiplying the eBC concentrations by the absorption mass efficiency, the light absorption coefficient (σ_{AP}) can be calculated at 637 nm.

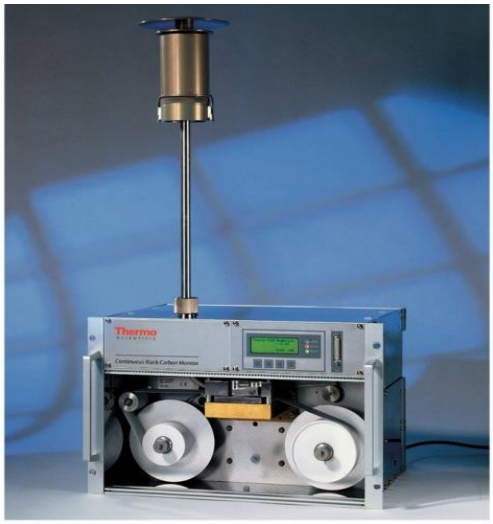

Figure 3-6: Multi-angle absorption photometer (MAAP) (model 5012 Thermo Fisher Scientific Inc.) instrument

3.2.1.3 Particulate matter

Particulate matter with an aerodynamic diameter ≤ 10 µm (PM_{10}) was measured with a synchronised hybrid ambient real-time particulate (SHARP) monitor (model 5030, Thermo Fisher Scientific Inc.) (Figure 3-7).

Figure 3-7: Synchronised hybrid ambient real-time particulate (SHARP) monitor (model 5030, Thermo Fisher Scientific Inc.) instrument

3.2.2 Meteorology

A Vaisela QMR102 tip bucket rain intensity meter was used to measure precipitation. Relative humidity (RH) and ambient temperature were measured with a Rotronic MP

101A instrument, while wind speed and direction were measured with a Vector A101ML and A200/L, respectively.

3.2.3 Ancillary measurements

SO_2 was measured with a Thermo-Electron 43S SO_2 analyser, NO/NO_x with a Teledyne 200AU $NO/NO_2/NO_x$ analyser, CO with a Horiba APMA-360 CO analyser, and O_3 with an Environment SA 41M O_3 analyser, respectively. Maintenance and calibration of these instruments at Welgegund have been extensively discussed in previous publications (e.g. Beukes *et al*., 2015), and are therefore not repeated here.

3.3 General data processing

The Welgegund measurement station is most likely the most comprehensively equipped long-term continuously operating atmospheric monitoring station in the southern Africa interior (Beukes *et al*., 2015). The measurements were conducted from September 2011 to November 2016, which were only interrupted if instruments were calibrated or serviced when general maintenance was performed, and during power failures. Beukes *et al*. (2015) described in detail the site maintenance procedures and data quality assurance that entailed various steps/actions; therefore, only a summary is give here. A scheduled site visit was undertaken once a week for maintenance of measurement equipment, including inspection and adjustment of instrument flows, inlet cleaning and other *ad hoc* procedures. PM_{10} measurement equipment was calibrated once a month. All instruments are connected to a master PC that is linked to a modem, which sent the data to a server on a daily basis. The downloaded data were inspected daily (during weekdays) for quality assurance. If irregularities were observed, or if instrumental diagnostic signals were abnormal, the site was visited (in addition to the scheduled weekly visit) as soon as possible, usually on the same day, to resolve the problem. Times of visits and actions taken were recorded on an electronic diary. For all instruments, the raw high resolution 1 min data were processed to account for maintenance and calibrations, as well as power failures and recovery periods after power failures. The data were corrected based on diary entries and uncertain data quality periods were automatically removed with fit-for-purpose Matlab algorithms and then for flow checks. For additional quality assurance, the data were also visually inspected. Thereafter, the 1

min data were converted to 15 min averages. Such averages were also only calculated if at least two thirds of the 1 min data were available. All particle concentrations were also converted to standard temperature and pressure conditions.

3.4 Data analysis

3.4.1 Aerosol optical calculations

Procedures previously described by Laakso *et al*. (2012) were used to calculate the various optical parameters. Firstly, the scattering coefficient (σ_{SP}) was corrected for temperature (273 °K) and pressure (1013 mbar) to correlate with the σ_{AP}'s temperature and pressure, and secondly the nephelometer truncation error was corrected according to Müller *et al*. (2011). The MAAP data were also corrected for artefacts (Hyvärinen *et al.*, 2013) during the data quality assurance described in Section 3.3. Thereafter, the Ångström exponent (α_{SP}) was calculated for the entire wavelength range (450, 525, 635nm), by fitting the logarithm of the σ_{SP} and the respective wavelengths to Eq. (3.1):

$$\ln(\sigma_{SP}, \lambda) = -\alpha_{SP} \ln(\lambda) - C \tag{3.1}$$

where C is a constant.

The α_{SP} was then used to logarithmically interpolate the wavelength of σ_{SP} to correlate with that of the σ_{AP}, measured with a MAAP at λ = 637 nm (Müller *et al*., 2011). Therefore, σ_{SP} and σ_{AP} reported in this paper will be for λ = 637 nm. The single scattering albedo (ω_0) can be defined as:

$$\omega_0 = \frac{\sigma_{SP}}{(\sigma_{SP}+\sigma_{AP})} \tag{3.2}$$

at 637 nm (Gong *et al*., 2015, Montille *et al*., 2011). As previously indicated in section 2.4, the α_{SP} can be used as a qualitative indicator of particle size distribution (Laakso *et al*., 2012; Schuster *et al*., 2006; Ångström, 1929). Small values (α_{SP} <~ 1) indicate coarse mode particles (radii >~ 0.5 µm) that are associated with, for instance, sea salt and dust particles, and large values (α_{SP} >~ 2) indicate fine mode particles (radii <~ 0.5 µm) that are typically associated with biomass burning and anthropogenic

emissions (Ramachandran, 2018; Laakso *et al*., 2012; Schuster *et al*., 2006; Eck *et al*., 1999). The interpretation of α_{SP} is not unambiguous; however, as previously indicated (Shen *et al*., 2018; Virkkula *et al*., 2011; Garland *et al*., 2008; Schuster *et al*., 2006), it is more applicable to the interpretation of volume or mass mean diameters than number mean diameters.

3.4.2 Air mass history analysis

The Hybrid Single-Particle Lagrangian Integrated Trajectory (HYSPLIT) model (version 4.8) of the National Oceanic and Atmospheric Administration (NOAA) Air Resources Laboratory (ARL) was used to determine air mass histories (Draxler & Hess, 2004). The model was run with meteorological data from the Graphical Data Analysis System (GDAS) archive of the US National Weather Service's National Center for Environmental Prediction (NCEP) and archived by ARL (Air Resources Laboratory, 2012). All back trajectories were calculated for 96 hours backwards, arriving hourly at Welgegund with an arrival height of 100 m. Lower arrival heights could result in increased error margins on individual trajectory calculations, since the orography in HYSPLIT is not very well defined. Overlay back trajectory maps (e.g. as presented in Figure 3-4) were generated by superimposing individual back trajectories with a fit-for-purpose algorithm on a southern African map that was divided into 0.1 x 0.1 degree grid cells. The number of trajectories passing over all the cells were then normalised (to maximum 100 %) with the colours red and dark blue indicating the highest and lowest overpass percentages, respectively. The pixel-like characteristics caused by the 0.1 x 0.1 degree grid cell division were partially removed by interpolating the colours. Similar procedures have been applied by numerous previous authors (e.g. Venter *et al*., 2015; Laakso *et al*., 2012).

3.4.3 Fire locations

Fire locations were determined with the Moderate Resolution Imaging Spectroradiometer (MODIS) collection 5 burned area product (Roy *et al.*, 2008) and results expressed as gridded 500 m pixels as specified in the MODIS user manuals (Boschetti *et al*., 2013, 2009)

3.4.4 Multiple linear regression

Multiple linear regression (MLR) models the relationship between one or more independent variables (x) and a dependent variable (y) by fitting a linear equation to the observed data, where c is constants or known parameters:

$$y = c_0 + c_1x_1 + c_2x_2 + c_3x_3 + \ldots\ldots\ldots\ldots\ldots\ldots c_ix_i \quad (3.3)$$

In this study, MLR analysis was conducted by using a fit-for-purpose Matlab algorithm to determine whether the σ_{SP}, σ_{AP}, ω_0 and α_{SP} values (considered as dependent parameters) could be estimated from other independent parameters measured at Welgegund. All independent parameters, i.e. gaseous species such as O_3, SO_2, NO, NO_2 and CO, radiation, temperature, RH, wind speed and direction, potential temperature gradient and PM_{10}, were considered in this analysis. The root mean square error (RMSE) was used to compare the measured values of the aerosol optical properties with the calculated values applying the optimal MLR equation. The RMSE measures the quality of the fit between the measured data (actual) and predicted (calculated) values (Salkind, 2010). Previous studies applied similar methods for several atmospheric species, e.g. Du Preez *et al*. (2015), Venter *et al*. (2015) and Awang *et al.* (2015). The RMSE was calculated with Eq. 3.4:

$$RMSE = \sqrt{\frac{\sum_{i=1}^{n} (Y_{calc,i} - Y_{exp,i})^2}{n}} \quad (3.4)$$

Where Y_{calc} is the predicted/calculated value using a specific model, Y_{exp} is the experimental/observed values from the actual data, and n the number of observations

3.4.5 T-test analysis

The t-test was used to evaluate the statistical difference between aerosol optical properties categorised in different periods in Section 5.2.2. A p-value of 0.05 was utilised as the threshold. Values less than this threshold indicated a statistical variance, i.e. aerosol optical property values were statistically different. In contrast, p-values above 0.05 were considered not statistically different. Although various source regions and periods may not prove statistically different, visual assessment of

the back trajectory maps still yielded valuable information, and variance, since the t-test does not consider intra-variance in geographic location.

Chapter 4

Meteorology, open biomass burning frequencies and temporal patterns of aerosol optical properties

In this chapter, the meteorological parameters, i.e. temperature, relative humidity and cumulative precipitation (section 4.1), at Welgegund, as well as open biomass burning frequencies of southern Africa (section 4.2) are presented. These factors can influence the aerosol optical properties significantly, and therefore they are considered here. Thereafter, the seasonal (section 4.3) and diurnal (section 4.4) patterns of the aerosol optical properties are considered within the context of possible sources. The chapter ends with a short conclusion (section 4.5).

4.1 Meteorological data

Seasons observed at Welgegund can be divided into two periods, i.e. the warm and wet period (October to April) that includes late spring, summer and early autumn, and the cold and dry period (May to September), which includes late autumn, winter and early spring. From Figure 4-1 that presents the median, 25th and 75th percentiles of the monthly temperature for the entire measurement period measured at Welgegund (September 2011 to November 2016), a seasonal variation is evident. Higher temperatures (21 °C median) can be observed from November to February, and lower temperatures (10 ºC median) during the cooler months (May to August). The highest temperature recorded at Welgegund during the measurement period was 39.8 °C in November 2012, while the lowest temperature was -6 °C in October 2015.

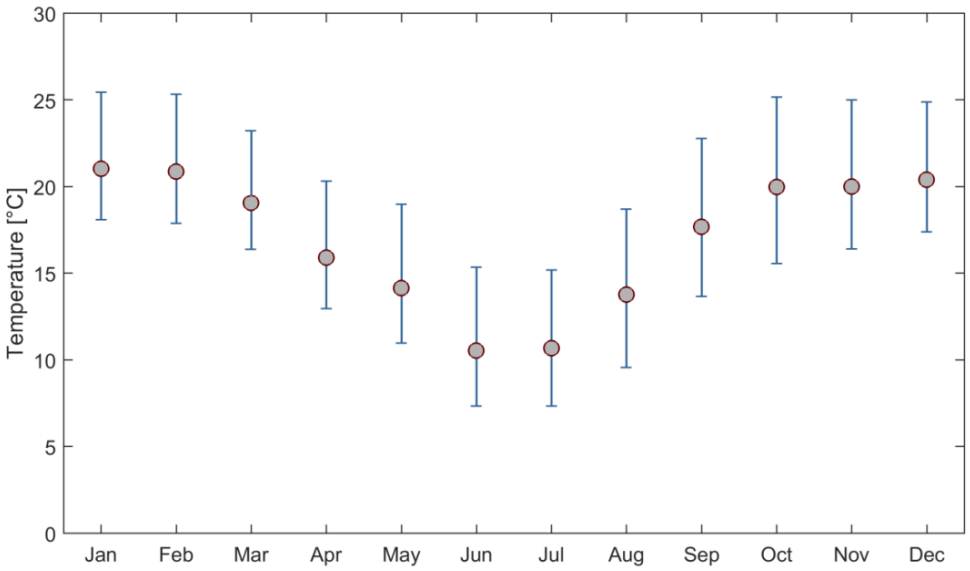

Figure 4-1: Monthly median temperatures (dots), as well as the 25th and 75th percentiles (whiskers) for the entire measurement period at Welgegund

Cold and dry periods are usually associated with lower relative humidity (RH) and little to no precipitation, whereas the warm and wet period is characterised by higher RH and more precipitation. This can be observed in Figures 4-2 and 4-3 that present the median, as well as 25th and 75th percentiles, of the monthly RH and cumulative rain, respectively, for the entire measurement period. From these figures, seasonal variations can also be observed. RH that is generally above 50 % is associated with higher precipitation (~86 mm/month average) in the warmer months, whereas the cooler months received on average almost no precipitation (below ~15 mm/month) with lower RH (generally below 50 %). The average annual precipitation is ~500 mm and approximately >80 % of rain events take place in the wet season.

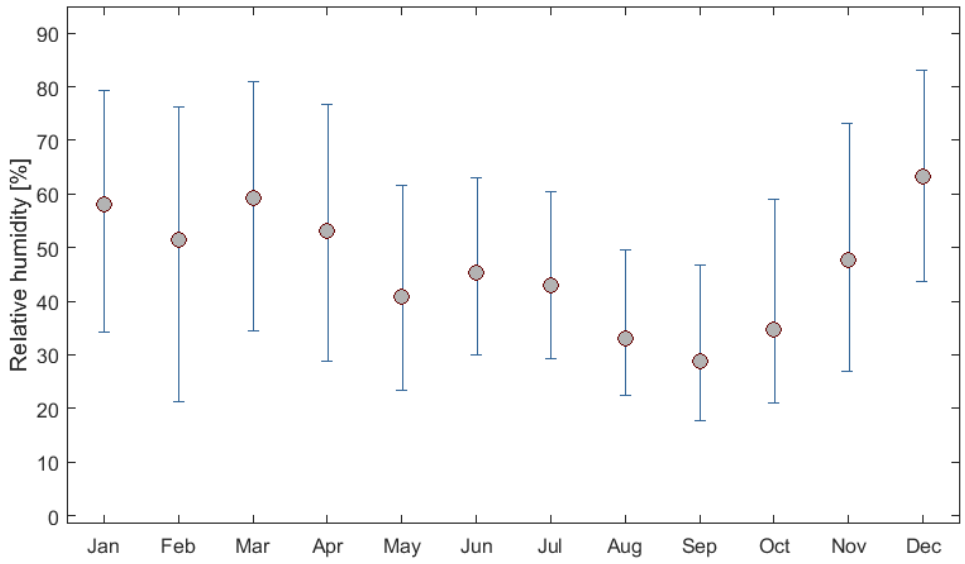

Figure 4-2: Monthly median % RH (dots), as well as the 25th and 75th percentiles (whiskers) for the entire measurement period at Welgegund

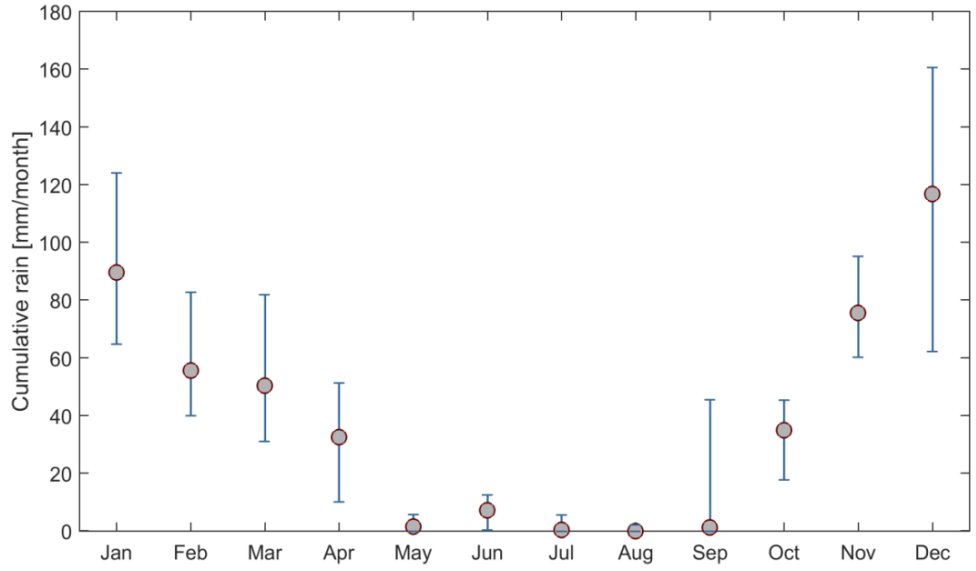

Figure 4-3: Monthly median cumulative rain (dots), as well as the 25th and 75th percentiles (whiskers) for the entire measurement period at Welgegund

4.2 Open biomass burning frequencies

Southern Africa is one of the largest sources of open biomass burning emissions on a global scale (Vakkari *et al*., 2014; Van der Werf *et al*., 2010; Langmann *et al*., 2009). Annually, thousands of square kilometres of savannah and grassland (section

3.1, Figure 3-1) are burned. Biomass burning plumes from southern Africa can even affect Australia (Pak *et al*., 2003; Swap *et al*., 2003). These plumes were described as the 'River of smoke' by Swap *et al*. (2003), which are hundred kilometres wide and thousands of kilometres long. During the cold and dry period, the lack of precipitation (Figure 4-3) contributes significantly to open biomass burning, whereas such fires are to a large degree prevented during the warm and wet season. This can be observed in Figure 4-4 presenting the Moderate Resolution Imaging Spectroradiometer (MODIS) burned area pixel counts within 100 and 250 km radii around Welgegund for the entire measurement period, as well as the monthly cumulative rain measured at Welgegund. The highest open biomass burning frequencies were evident from May to October, and fewer open biomass burning frequencies from November to April. According to Archibald *et al*. (2008), availability of fuel and moisture, as influenced by the preceding two years' rainfall, is likely the important driver for open biomass burning frequency and spatial variation in southern Africa. Therefore, from Figure 4-4, it is evident that 2014 had above average rainfall (~101 % of regional average; Droughtsa, 2019) with the highest burn scar pixel counts, while 2016 was below the average rainfall year (~83 % of regional average; Droughtsa, 2019) with the lowest burn scar pixel counts. The spatial distribution of open biomass burning in southern Africa is illustrated in Figure 4-5, which uses 2014 as an example. It is obvious from Figure 4-5 that most open biomass burning occurs in northern and eastern South Africa, due to biomes there being more productive (section 3.1, Figure 3-1).

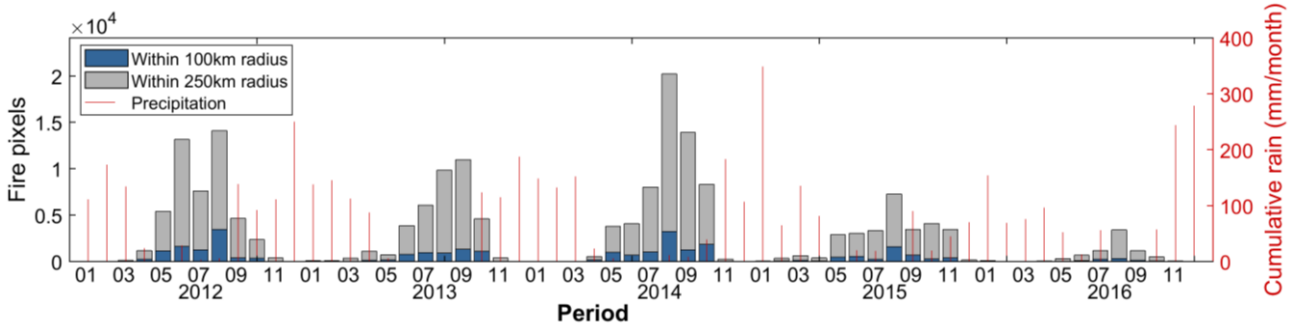

Figure 4-4: Fire burnt scar pixel counts within 100 and 250 km radii around Welgegund, determined with MODIS collection 5 burned area product (Roy *et al*., 2008), and monthly cumulative rain measured at Welgegund, for the entire measurement period

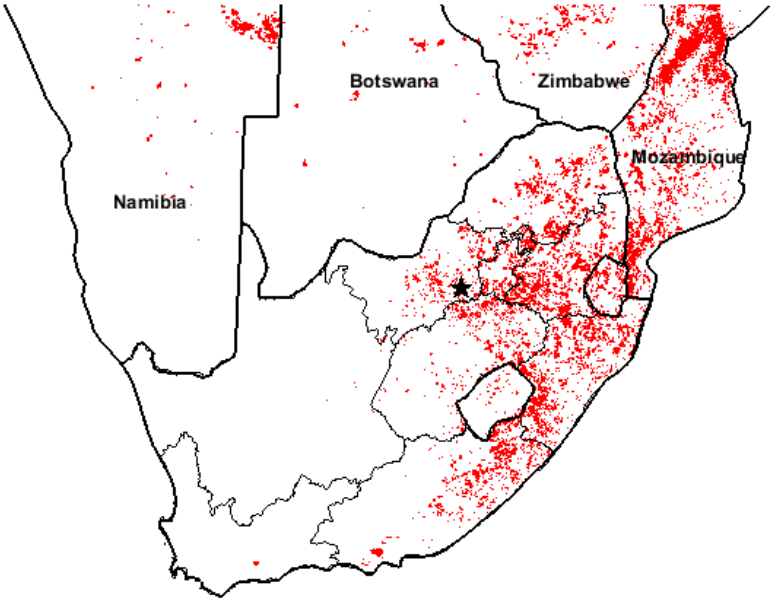

Figure 4-5: A map of southern Africa indicating fire pixels observed for 2014 determined with MODIS collection 5 burned area product (Roy *et al*., 2008)

4.3 Seasonality of aerosol optical properties

4.3.1 Scattering coefficient (σ_{SP}) and absorption coefficient (σ_{AP})

Figures 4-6a and 4-7a present the monthly statistical distribution of σ_{SP} and σ_{AP}, respectively, for the entire measurement period. Figures 4-6b and 4-7b present the monthly statistical distribution of σ_{SP} and σ_{AP}, with data in corresponding months grouped together (i.e. all January data grouped together, Februaries, etc.). From both these sets of figures (Figures 4-6a and b, as well as 4-7a and b), a clear seasonal cycle can be observed. The highest medians were observed in the winter and early spring months (June to September), while the lowest medians were recorded during the summer and autumn months (December to April). There are several possible reasons for the relatively well-defined σ_{SP} and σ_{AP} seasonal patterns. Domestic space heating occurs mostly during the colder winter months in the South African interior (Chiloane *et al*., 2017; Hersey *et al*., 2015; Venter *et al*., 2012), while domestic cooking is practised irrespective of ambient temperatures. The fuel used in domestic combustion depends on the availability and cost of the various fuel types, but low grade coal, wood and paraffin are very typical (Pretorius *et al*.,

2015). Furthermore, open biomass burning frequency generally increases during winter and peaks in either late winter (August) or early spring (September) (Figure 4-4), which is also the driest period (Figures 4-2 and 4-3). Less wet deposition (Figure 4-3), increased anti-cyclonic recirculation of air masses over the South African interior (Tyson *et al*., 1996), lower planetary boundary layer (PBL) depths and more prominent thermal inversion layers (Gierens *et al*., 2019; Korhonen *et al*., 2014; Garstang *et al*., 1996) during the colder months all result in aerosol accumulation in the lower atmosphere. Increased wind-blown dust also occurs during the dry season, especially the late dry season (August to mid-October). Additionally, in the cold winter months (Figure 4-1), higher electricity consumption occurs in South Africa (Pretorius *et al*., 2015), which results in increased sulphur dioxide (SO_2) and nitrogen oxide (NO_x, a combination of nitrogen monoxide, NO, and nitrogen dioxide, NO_2) emissions (which are precursors of aerosol sulphate, SO_4^{2-} and nitrate, NO_3^-, respectively), from large coal-fired power stations that do not remove such species from their off-gas (Pretorius *et al*., 2015; Lourens *et al*., 2011). Considering the afore-mentioned, the observed σ_{SP} and σ_{AP} seasonal patterns are likely due to a complex combination of the afore-mentioned seasonal sources and meteorological conditions.

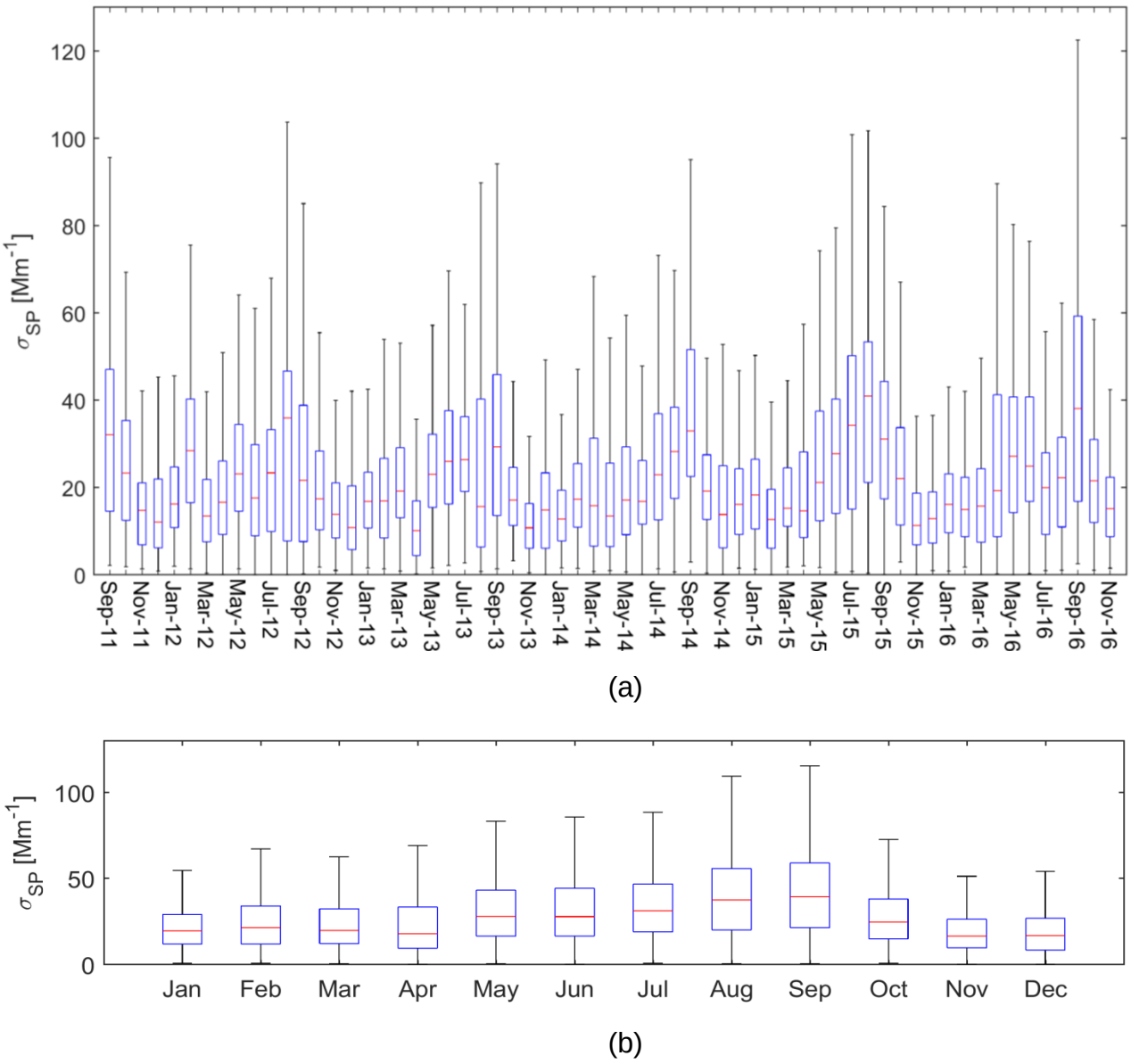

(a)

(b)

Figure 4-6: (a) Monthly statistical distribution of σ_{SP} measured at Welgegund for the entire measurement period. (b) Monthly statistical distribution of σ_{SP}, with corresponding months grouped together (i.e. all January data grouped together, Februaries, etc.). The red line represents the median, the top and bottom edges of blue boxes the 25th and 75th percentiles and the black whiskers indicate 99.3 % coverage

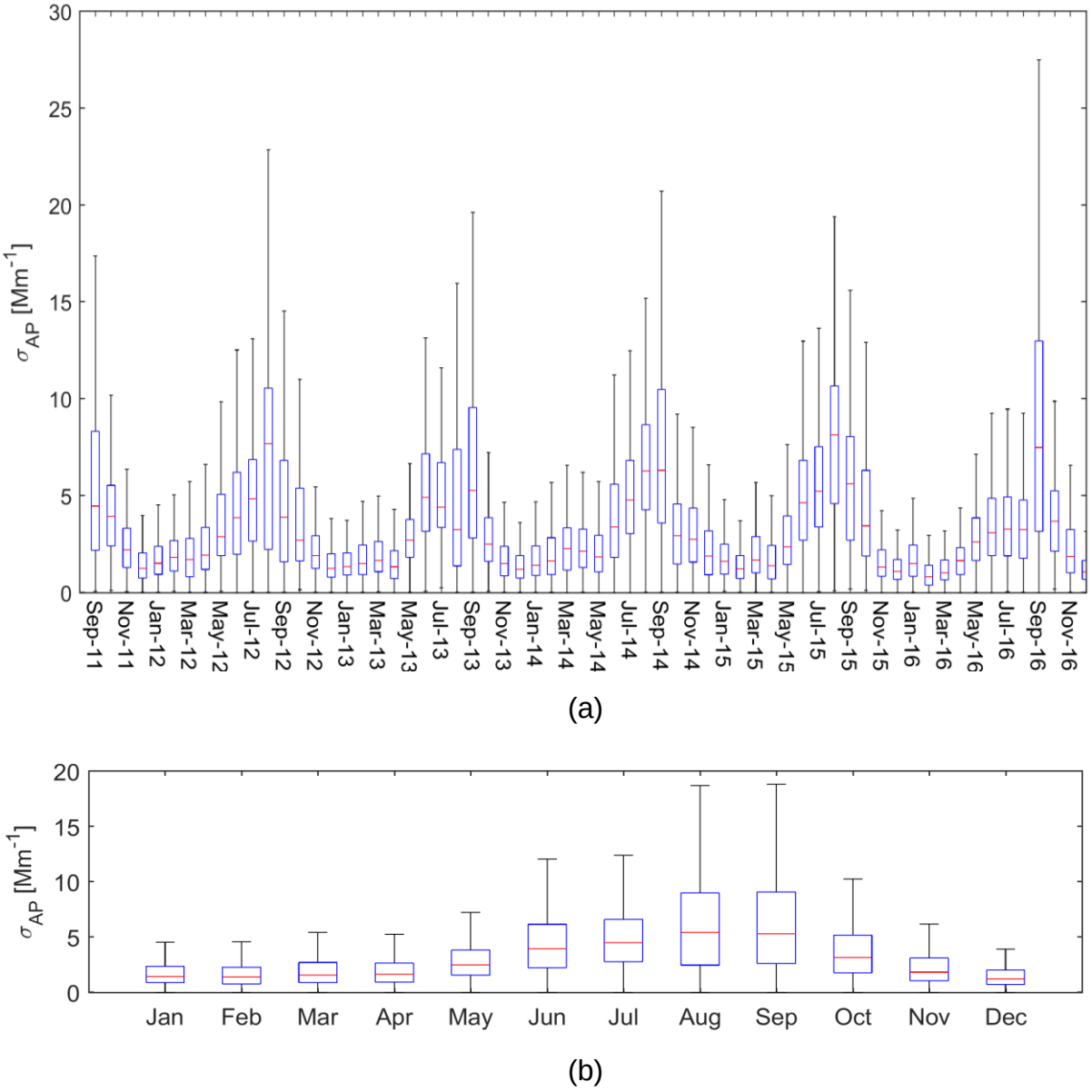

Figure 4-7: (a) Monthly statistical distribution of σ_{AP} measured at Welgegund for the entire measurement period. (b) Monthly statistical distribution of σ_{AP}, with corresponding months grouped together (i.e. all January data grouped together, Februaries, etc.). The red line represents the median, the top and bottom edges of blue boxes the 25th and 75th percentiles and the black whiskers indicate 99.3 % coverage

4.3.2 Single scattering albedo (ω_0)

In Figures 4-8a and 4-8b, a clear seasonal pattern can be observed for ω_0, with more absorbing aerosols observed during the winter and early spring months, while more reflective aerosols occurred during the summer and early autumn months. This

ω_0 seasonality does not correlate with the σ_{SP} and σ_{AP} seasonality, where both these parameters reach maximum values in the winter and/or early spring. The reason why the ω_0 seasonality differs from that of σ_{SP} and σ_{AP} is due to the σ_{AP} peak in the late dry season being much sharper (increase if compared to wet season) than the corresponding σ_{SP} peak. This is illustrated by the relatively small ratio difference of 2.1 between the average of the three highest (89.2 Mm^{-1}) and average of the three lowest (42.8 Mm^{-1}) medians of the σ_{SP} per season, if compared to the correlating average ratio of 3.6 for σ_{AP} (derived from the average of the three highest medians, i.e. 16.1 Mm^{-1}, and the average of the three lowest medians, i.e. 4.5 Mm^{-1} per season). The σ_{AP} being much sharper than the σ_{SP} peak can be due to increased equivalent black carbon (eBC) emissions from seasonal combustion sources (e.g. open biomass burning and domestic combustion for space heating), as previously indicated (Chiloane *et al*., 2017; Tiitta *et al*., 2014). In addition, SO_2 will be converted more effectively to SO_4^{2-} during the higher RH conditions (Connell, 2005; section 2.2.5.1) in the wet season (Figure 4-3), which will contribute to the σ_{SP} not reducing as much as σ_{AP} during that time of the year. SO_4^{2-} has been proven to be the dominant inorganic ionic aerosol species (Venter *et al*., 2018; Aurela *et al*., 2016; Tiitta *et al*., 2014) and ionic species in rain water (Conradie *et al.*, 2016) in the South African interior.

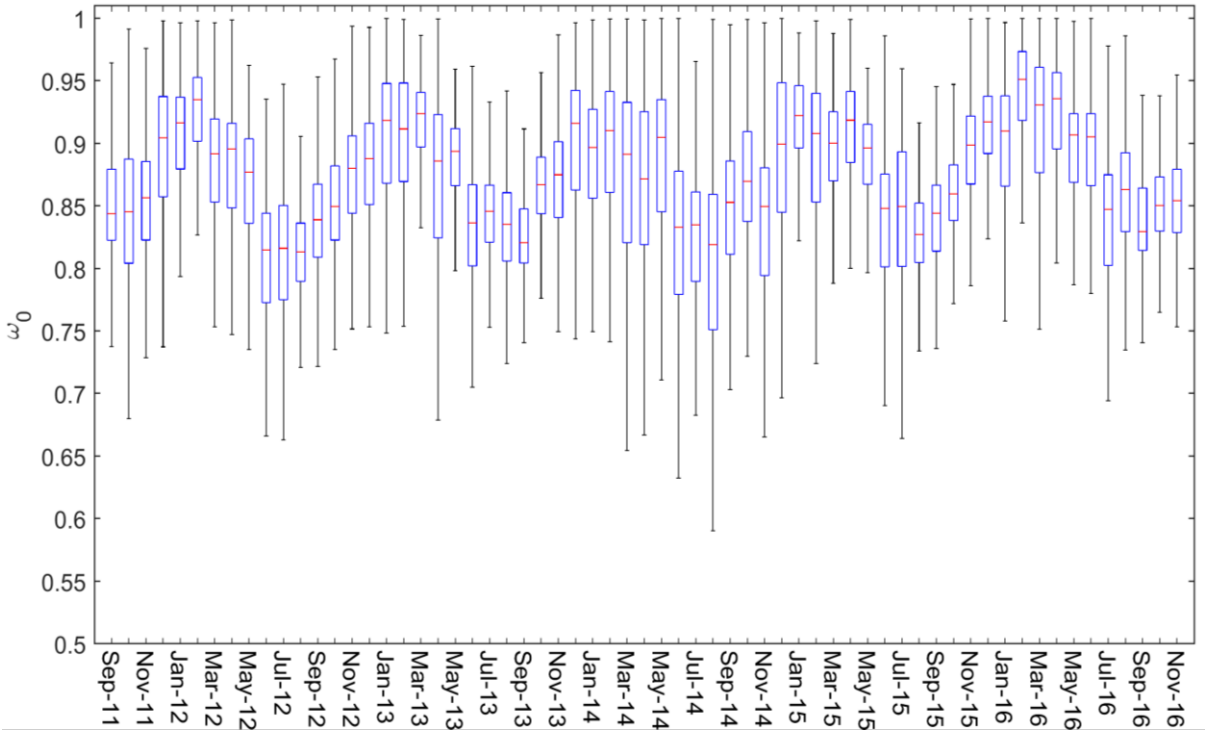

(a)

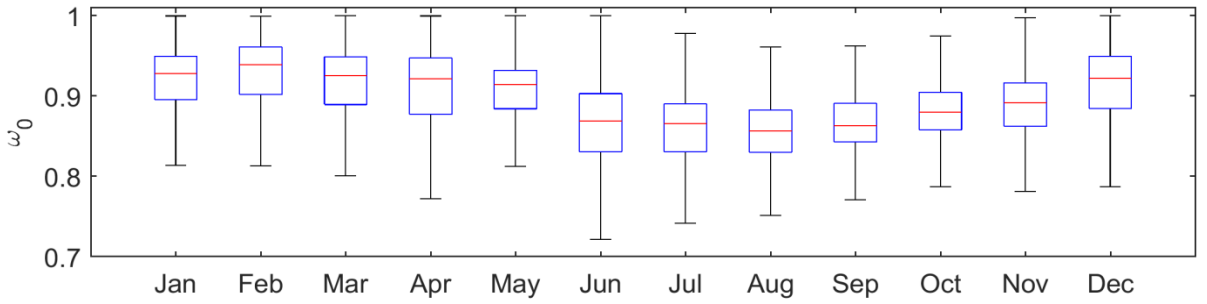

(b)

Figure 4-8: (a) Monthly statistical distribution of ω_0 measured at Welgegund for the entire measurement period. (b) Monthly statistical distribution of ω_0, with corresponding months grouped together (i.e. all January data grouped together, Februaries, etc.). The red line represents the median, the top and bottom edges of blue boxes the 25th and 75th percentiles and the black whiskers indicate 99.3 % coverage

4.3.3 Ångström exponent (α_{SP})

A seasonal cycle for the α_{SP}, with the highest median and smallest particle size distribution in summer and early autumn months, and lowest median and largest particle size distribution in the winter and early spring months, can be observed in

Figures 4-9a and b. The timing of the minima in α_{SP} correlates with the peak in wind-blown dust emissions, which are most significant in late winter and early spring. Open biomass burning also peaks during this time of the year (Figure 4-4), but generally emits smaller particles than wind-blown dust. In contrast, the summer and early autumn months are not impacted significantly by the afore-mentioned dry season specific emission sources, but are likely to be fractionally more affected by secondary aerosol formation that is very prevalent in the South African interior (Nieminen *et al*., 2018; Vakkari *et al*., 2015, 2011; Hirsikko *et al*., 2013, 2012).

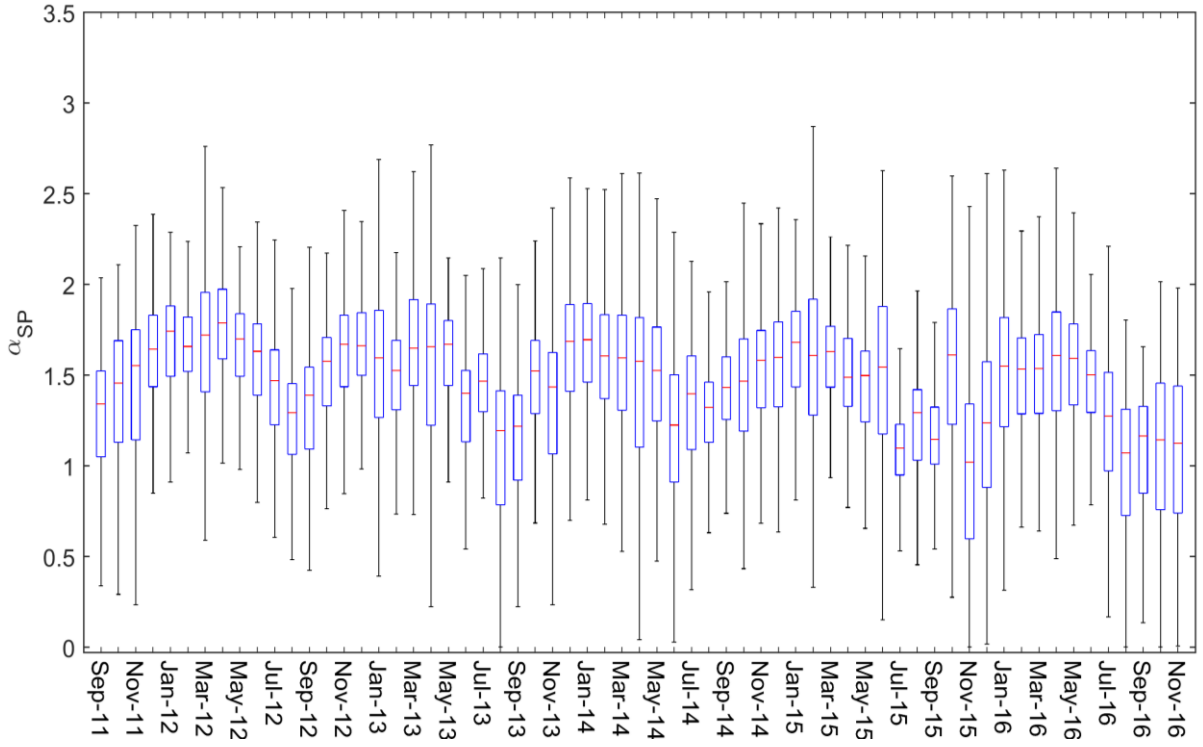

(a)

Figure 4-9: (a) Monthly statistical distribution of α_{SP} measured at Welgegund for the entire measurement period. (b) Monthly statistical distribution of α_{SP}, with corresponding months grouped together (i.e. all January data grouped together, Februaries, etc.). The red line represents the median, the top and bottom edges of blue boxes the 25th and 75th percentiles and the black whiskers indicate 99.3 % coverage

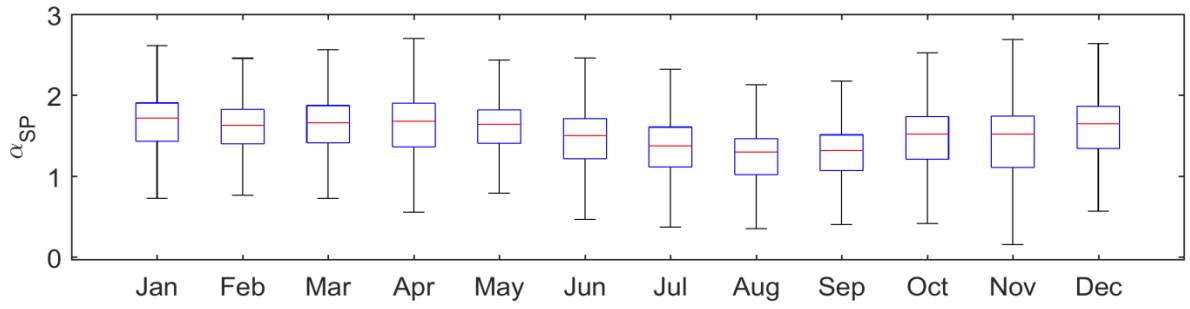

(b)

Figure 4-9: continue; (a) Monthly statistical distribution of α_{SP} measured at Welgegund for the entire measurement period. (b) Monthly statistical distribution of α_{SP}, with corresponding months grouped together (i.e. all January data grouped together, Februaries, etc.). The red line represents the median, the top and bottom edges of blue boxes the 25th and 75th percentiles and the black whiskers indicate 99.3 % coverage

An interesting phenomenon that can be observed from Figure 4-9a is that very small values for α_{SP} (approaching zero) are occasionally observed. These observations can be directly correlated with dust storms that are observed at Welgegund. Such small α_{SP} values are typically reported for Sahara and Middle Eastern dust impacted sites (Dubovik *et al*., 2001). Figures 4-10a and 4-10b present photos of such dust storms approaching a sport field in the city of Potchefstroom (approximately 22.5 km from Welgegund, measured in a straight line) and blowing across a road near Potchefstroom, respectively. A more detailed discussion of wind-blown dust and associated sources areas will be presented later.

(a)

(b)

Figure 4-10: Dust storms (a) approaching a sport field in the city of Potchefstroom (approximately 22.5 km from Welgegund, measured in a straight line) (photo courtesy of Bertus le Roux) and (b) blowing across a road near Potchefstroom (photo courtesy of Ville Vakkari)

4.4 Diurnal patterns of aerosol optical properties

4.4.1 σ_{SP} and σ_{AP}

In Figures 4-11 and 4-12, the average seasonal diurnal patterns of σ_{SP} and σ_{AP} are presented, respectively. As is evident from Figure 4-11, the σ_{SP} for all seasons peaked in the morning (between 6:45 and 8:15) and early evening (between 17:45 and 19:00). The σ_{AP} for all seasons (Figure 4-12) indicated similar patterns during the morning, but did not specifically peak in the early evening – it rather increased throughout the night. The afore-mentioned σ_{SP} and σ_{AP} diurnal patterns clearly indicate the influence of the PBL. Gierens *et al*. (2019) presented the evolution of layers observed in the PBL for the different seasons at Welgegund. In essence, the afore-mentioned authors indicated that all seasons had similar patterns, which entailed growth in the mean mixed layer depth from just after sunrise to a maximum (spring, summer, autumn and winter equal to ~2.5, 2.3, 2.05 and 1.9 km, respectively) in late afternoon (Gierens *et al*., 2019). The formation of the maximum PBL depth therefore correlates with the minima in observed σ_{SP} and σ_{AP} (Figures 4-11 and 4-12). According to Gierens *et al*. (2019), a residual layer remains after sunset – the depth of which decreases as the evening progresses. Additionally, after sunset, a stable layer (which is most likely due to thermal inversion) forms at an approximately mean depth of 100 m, which traps and concentrates near-surface emissions in a smaller volume (Gierens *et al*., 2019). This effect is stronger during the colder months, if compared to the warmer months (Gierens *et al*., 2019). In addition to the PBL, sources that vary diurnally (e.g. domestic combustion for space heating) can also contribute to the observed diurnal patterns.

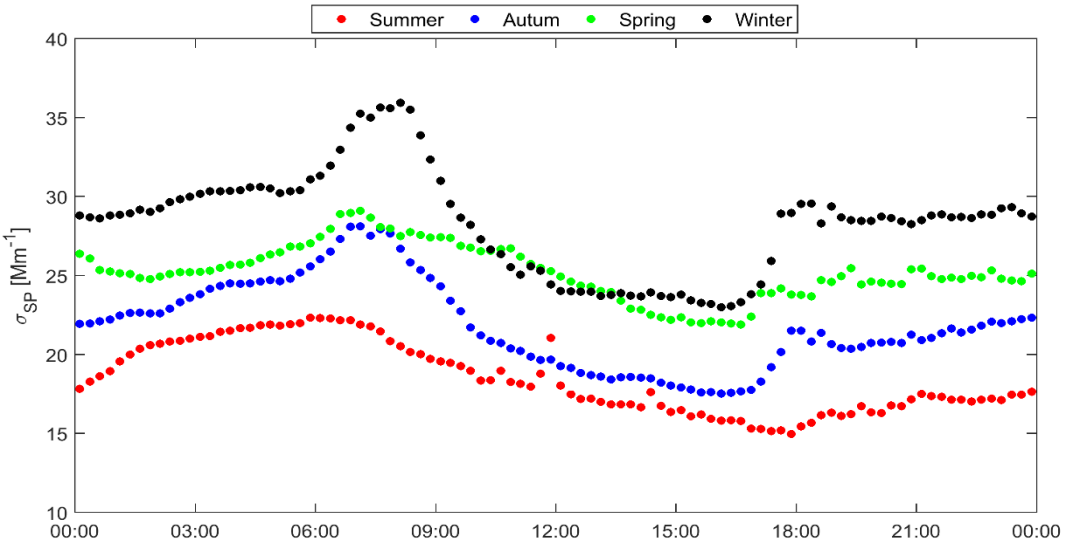

Figure 4-11: Average seasonal diurnal patterns of σ_{SP} measured at Welgegund for the entire measurement period

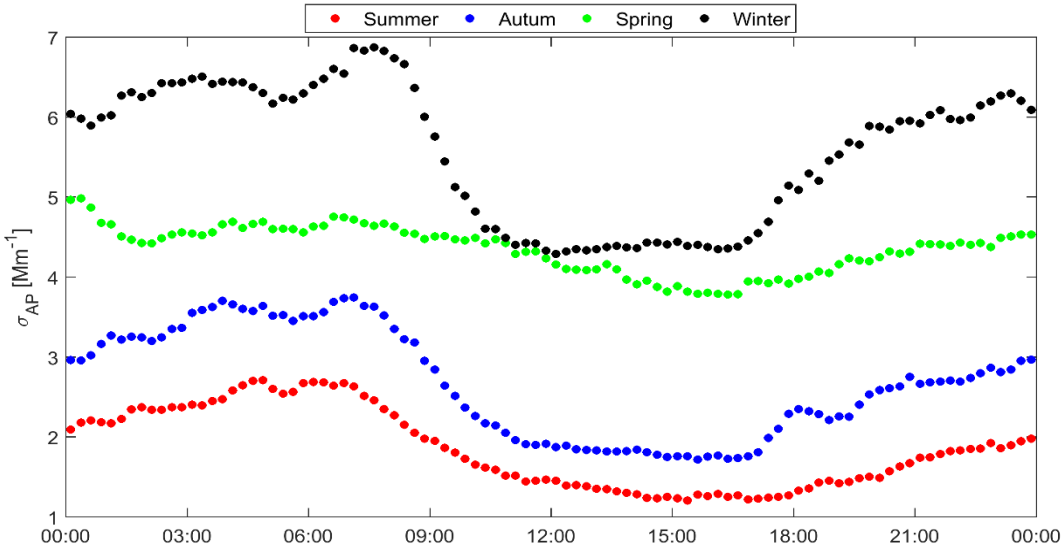

Figure 4-12: Average seasonal diurnal patterns of σ_{AP} measured at Welgegund for the entire measurement period

4.4.2 ω_0

Figure 4-13 presents the average seasonal diurnal patterns of ω_0, with all seasons indicating similar variations. The ω_0 starts increasing after sunrise in the morning, reaches a maximum at approximately 15:00, and decreases after sunset. Obviously, the ω_0 represents the combined effect of σ_{SP} and σ_{AP}; however, the following

reasons are likely to explain the more reflective nature of the particulate matter (PM) during daytime:

- After sunrise, ozone (O_3) starts forming due to photochemistry (Figure 4-14), with associated increased hydroxyl radical ($OH^{\bullet}$) concentrations (Seinfeld & Pandis, 2016; Connell, 2005) – both resulting in increased oxidising capacity that leads to higher concentrations of reflective species, e.g. organic aerosols (OA) and SO_4^{2-}, which dominate the PM composition in the South African interior (Venter *et al*., 2018; Aurela *et al*., 2016; Tiitta *et al*., 2014). From Figure 4-14, it is evident that O_3 concentrations at Welgegund reach maxima at approximately 1 to 2 hours after maxima solar radiation (Laban *et al*., 2018), which matches with maxima observed in the ω_0 diurnal patterns (Figure 4-13). As far as the candidate could assess, $OH^{\bullet}$ concentrations have not been measured in South Africa, although Gierens *et al*. (2014) did model diurnal patterns thereof.

- The break-up of low-level inversion layers and growth of the mixed layer in the PBL (Gierens *et al*., 2019) after sunrise result in downward mixing of SO_4^{2-} that had formed as a result of long range SO_2 transport. In South Africa, SO_2 is mostly emitted from high stacks (with heights of >200 m being common, ESKOM 2019a and 2019b). Downward mixed SO_2 can then also be oxidised to SO_4^{2-} during daytime. SO_4^{2-} has been linked to secondary aerosol formation in South Africa (Vakkari *et al*., 2015). In addition to the effect of SO_4^{2-}, the deeper PBL during daytime (Gierens *et al*., 2019) also dilutes eBC emitted mostly from near surface sources (e.g. open biomass burning and domestic combustion). Considering Figure 4-13 further, it is evident that the ω_0 diurnal pattern for spring indicated a similar trend to the other seasons, but with a much less significant amplitude difference. This could be due to the first half of spring (September and early October) being the driest (Figure 4-3). Atmospheric moisture is critical for the oxidation of SO_2 to SO_4^{2-}, with significantly less such conversion taking place at RH below 70 % (Seinfeld & Pandis, 2016; Connel, 2005; section 2.2.5.1). Obviously, differences in seasonal circulation patterns could also influence SO_2 and SO_4^{2-} long-range transport, but this was not considered in detail here.

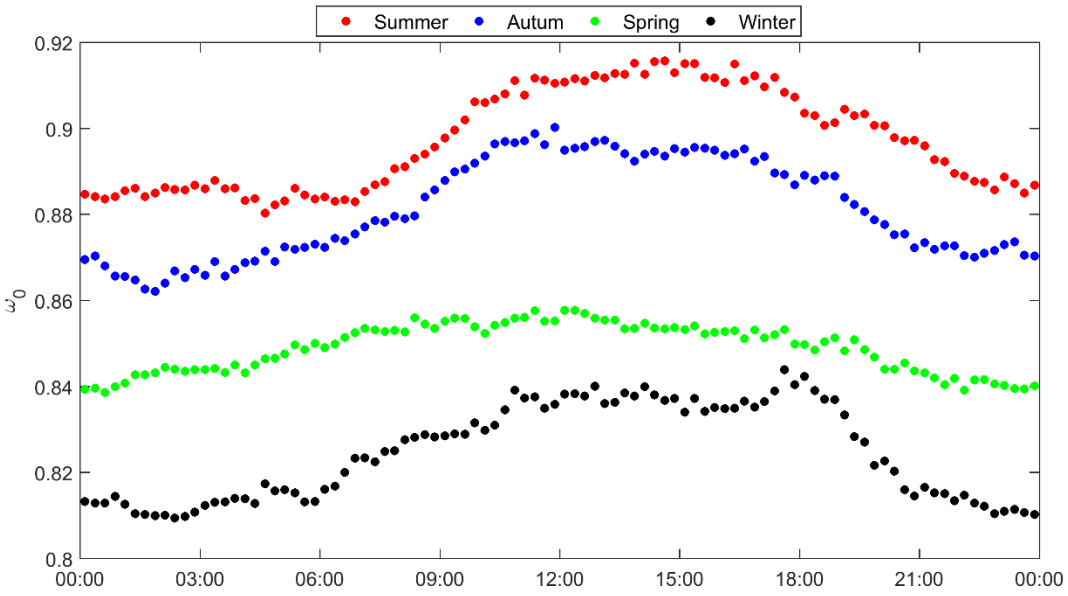

Figure 4-13: Seasonal diurnal patterns of ω_0 measured at Welgegund for the entire measurement period

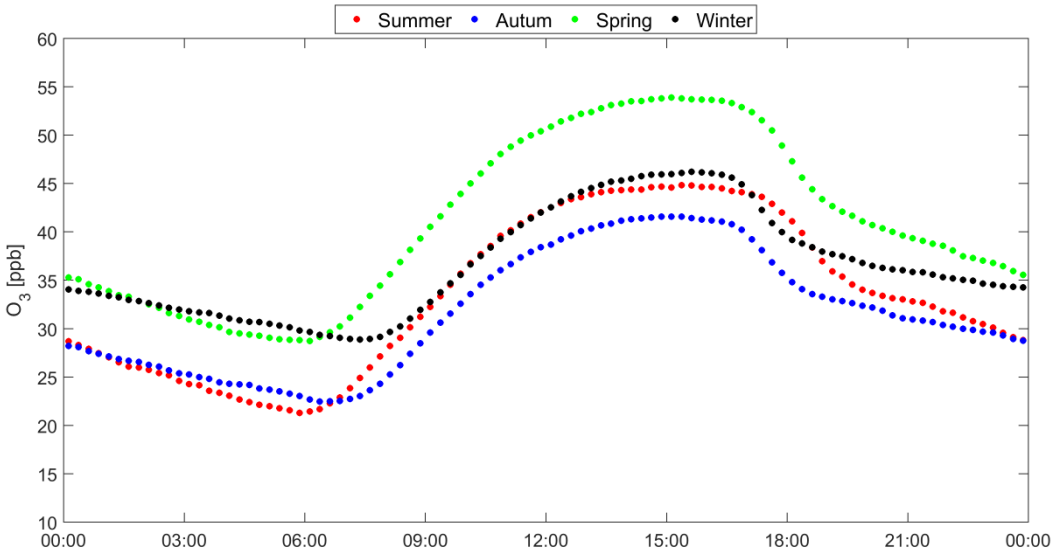

Figure 4-14: Seasonal diurnal patterns of O_3 measured at Welgegund for the entire measurement period

4.4.3 α_{SP}

Figure 4-15 presents the average seasonal diurnal patterns of α_{SP}. All the seasonal diurnal patterns were similar, with the amplitude changes in winter being the largest and in summer the smallest. These α_{SP} seasonal diurnal patterns were compared to the corresponding PM_{10} (PM with aerodynamic diameter less than 10 µm)

concentration patterns, as indicated in Figure 4-16. From this comparison, it is evident that the α_{SP} diurnal patterns are the inverse of the PM_{10} concentration patterns, which makes sense considering that α_{SP} is used to indicate particle size (Schuster *et al*., 2006; Ångström, 1929). Therefore, the PM_{10} patterns needed to be understood. Considering the earlier descriptions of the different layers in the PBL at Welgegund (Gierens *et al*., 2019), the peaks in PM_{10} observed during the mornings and early evenings had to originate from near-surface sources and/or pollution transported in the PBL that are concentrated due to formation of the very low-level thermal inversion at approximately 100 m depth (Gierens *et al*., 2019). Low-level sources could, for instance, be domestic combustion, which becomes a more significant source of PM in the South African interior as seasonal ambient average temperatures decrease (Figure 4-1 presented monthly median temperatures) – due to space heating becoming more important in addition to cooking (Chiloane *et al*., 2017). Additionally, open biomass burning plumes in southern Africa typically stay within the PBL (Labonne *et al*., 2007); therefore, it will also be a significant near surface source for Welgegund.

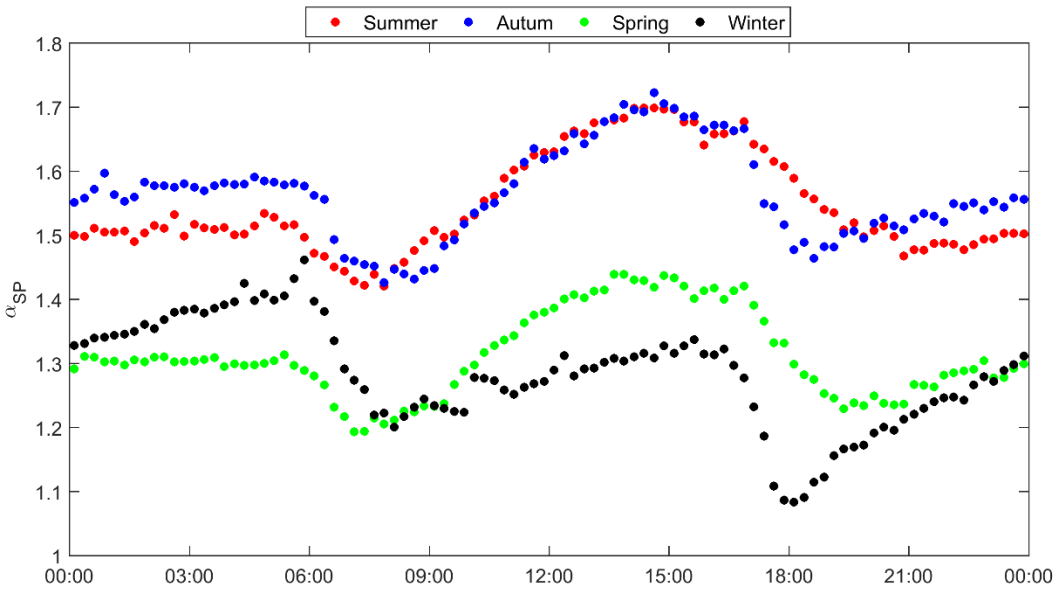

Figure 4-15: Seasonal diurnal patterns of α_{SP} measured at Welgegund for the entire measurement period

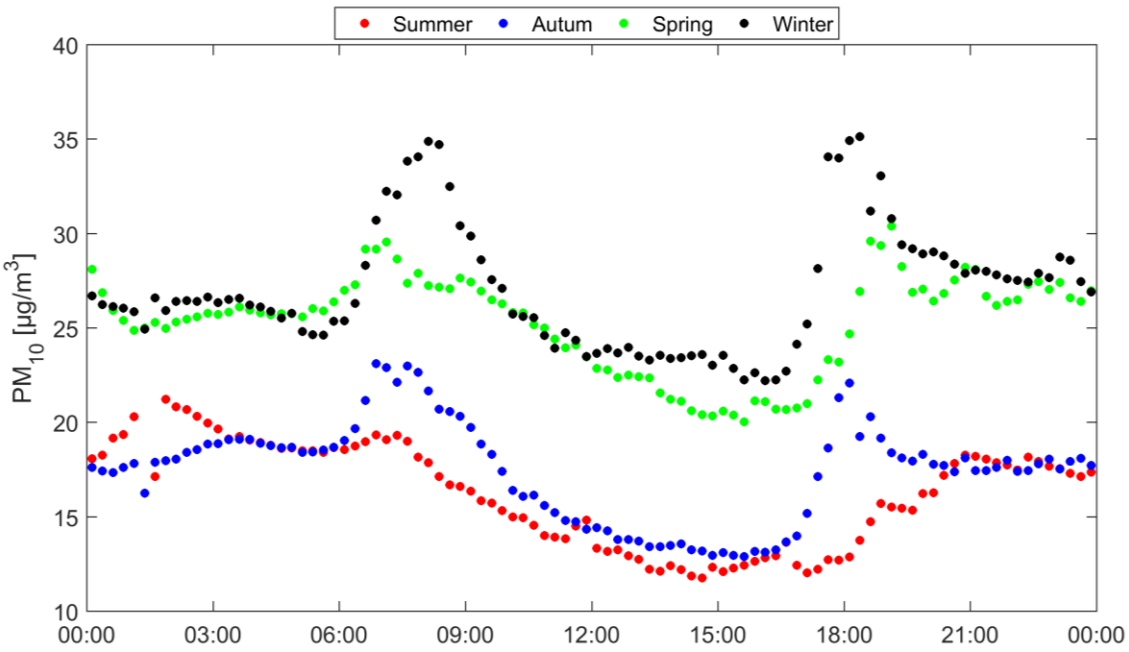

Figure 4-16: Seasonal diurnal patterns of PM_{10} measured at Welgegund for the entire measurement period

4.5 Chapter conclusion

Clear seasonal and diurnal patterns were observed for all the aerosol optical properties. By considering open biomass burning frequencies, meteorological data (temperature, RH, PBL, etc.) and possible sources, some deductions could be made with regard to contributing factors and sources to explain the observed temporal patterns. However, these deductions were mostly indicative.

Chapter 5

Source insights of aerosol optical properties

Several sources and/or meteorological factors contributing to the observed values and patterns of the aerosol optical properties have already been indicated in the previous chapter. In this chapter, possible sources and source regions are explored in greater detail through the use of two different approaches, i.e. auto-generated source maps (section 5.2) and defined source regions (section 5.3). In both these approaches, the entire measurement period, as well as defined periods were considered in order to isolate different sources better. The chapter ends with a short conclusion (section 5.4).

5.1 Introduction

In Chapter 4, some deductions could be made regarding possible contributing factors (e.g. meteorological conditions) and sources (e.g. open biomass burning, domestic combustion, wind-blown dust and industry) influencing the aerosol optical properties, i.e. scattering coefficient (σ_{SP}), absorption coefficient (σ_{AP}), single scattering albedo (ω_0) and Ångström exponent (α_{SP}) considered in this study. However, these deductions were mostly indicative and not unambiguous. In this chapter, the candidate employed various methods to further explore possible sources and/or factors influencing the aerosol optical properties. These methods were divided into two main approaches, i.e.:

i) Source maps that highlight geographical areas, which significantly influence any of the considered aerosol optical properties (Section 5.2). This was achieved by applying the method previously introduced by Vakkari *et al*. (2011, 2013) for aerosol size distribution, but within the context of aerosol optical properties. This technique was done by defining a 0.5 x 0.5 degree grid over the southern African map. For each calculated trajectory, grid cells over which the trajectory passed were assigned the mean of the observed optical property measured at Welgegund. Therefore, for multiple trajectories, the value in each

grid cell represented the mean of the optical property observed for all the trajectories passing over that grid cell. A minimum of 40 trajectory overpasses per grid cell were required in order to ensure that the results are statistically reliable. The geographical areas that were highlighted by this method were not influenced and/or selected by the candidate. In the rest of this study, the term used when referring to such map(s) is defined as “auto-generated source map(s)”. The uncertainty associated with the geographical areas indicated by the auto-generated source maps was at least partially due to the inherent uncertainties associated with the calculated trajectories. However, Vakkari *et al*. (2011, 2013) demonstrated that this method can be used to identify source areas or regions for atmospheric species measured at sites that not in close proximity to large point sources.

ii) Source regions were defined by the candidate (section 5.3), based on prior knowledge and literature, as well as observations from the auto-generated source maps. The source regions were defined in three different methods, which will be explained in the relevant sub-sections, i.e. sections 5.3.1 to 5.3.3. Back trajectories were classified as passing over the defined source regions, for which aerosol optical properties could then be considered. The term “defined source region(s)” will be used when referring to such map(s).

5.2 Auto-generated source maps

5.2.1 Auto-generated source maps for the entire measurement period

Auto-generated source maps for σ_{SP}, σ_{AP}, ω_0 and α_{SP}, measured over the entire measurement period (September 2011 to November 2016), are indicated in Figures 5-1a and 5-1b, 5-3 and 5-4, respectively. The σ_{SP} and σ_{AP} maps are subsequently discussed in sections 5.2.1.1, while the ω_0 and α_{SP} maps are considered in sections 5.2.1.2 and 5.2.1.3, respectively.

5.2.1.1 σ_{SP} and σ_{AP}

Form Figures 5-1a and 5-1b, high σ_{SP} and σ_{AP} were observed in air masses that had passed over eastern Zimbabwe and central Mozambique. This reflects the high

frequency of open biomass burning (section 4.2, Figure 4-5) observed over these areas. The open biomass burning emissions from eastern Zimbabwe and central Mozambique are expected to be higher per unit surface area due to the more productive savannah biome, if compared to the grassland biome that covers a significant portion of the South African interior (section3.1, Figure 3.1). Tiitta *et al*. (2014) showed that organic aerosols (OA) make up the largest fractional contribution of particulate matter with an aerodynamic diameter less than 1 µm (PM_1) measured at Welgegund, especially during the dry and open biomass burning season when biogenic volatile organic compound (BVOC) emissions are at a minimum (Jaars *et al*., 2016). Maritz *et al*. (2019) indicated that the above-mentioned is also similarly true for $PM_{2.5}$ (PM with an aerodynamic diameter ≤ 2.5 µm) particulate organic matter (POM) at a number of sites in the South African interior.

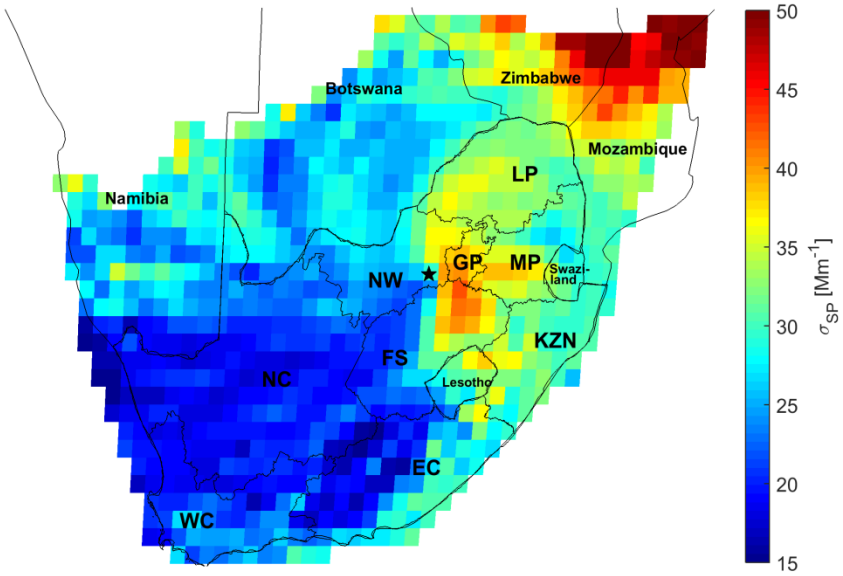

(a)

Figure 5-1: Auto-generated source maps of the average (a) σ_{SP} and (b) σ_{AP} observed at Welgegund for the entire measurement period, according to the method introduced by Vakkari *et al*. (2013, 2011)

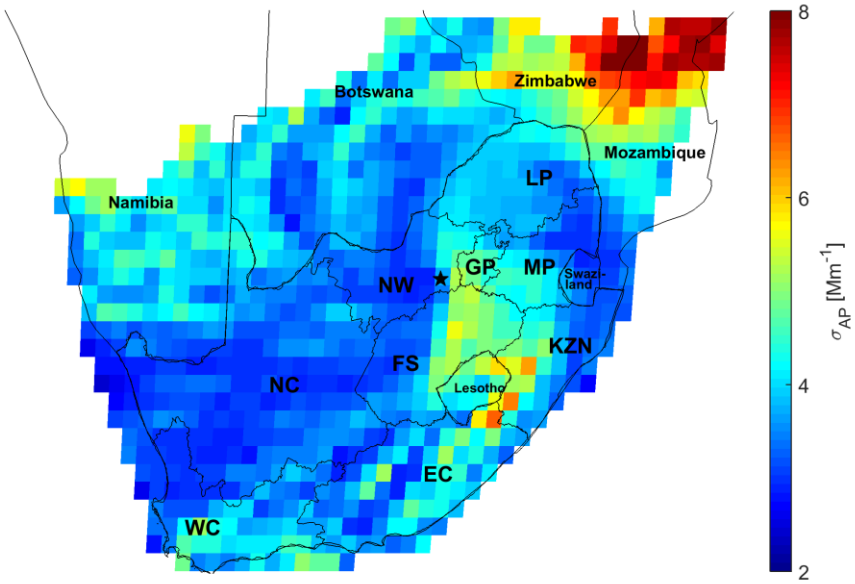

(b)

Figure 5-1: continue; Auto-generated source maps of the average (a) σ_{SP} and (b) σ_{AP} observed at Welgegund for the entire measurement period, according to the method introduced by Vakkari *et al*. (2013, 2011)

For σ_{SP} (Figure 5-1a), higher values were also observed in air masses that had passed over the eastern Free State and the Vaal Triangle. The influence of the Vaal Triangle was expected, since it is one of the most industrialised regions in South Africa. This area, together with the southern portion of the Gauteng Province (section 3.1, Figure 3-1), has been declared an area with significant air quality problems, i.e. a priority area (Government Gazette Republic of South Africa, 2005b). The effect of air masses that had passed over the eastern Free State on the σ_{SP} could possibly be due to this area being the largest maize (staple food in South Africa) producing region (Department: Agriculture, Forestry and Fisheries, 2016). Maize production in the Free State Province is confined to the eastern region, since the western Free State is situated in the Karoo biome (section 3.1, Figure 3-1), which is a dry, less productive biome where maize is not cultivated commercially. For maize cultivation, the planted fields are typically ploughed in preparation for sowing. This exposes large areas that then become susceptible to wind-blown dust generation. To test this theory, a PM with an aerodynamic diameter less than 10 µm (PM_{10}) auto-generated source maps, as presented in Figure 5-2, was generated. This figure clearly indicates that the eastern Free State is a very significant source of PM_{10}. According

to Figure 5-2, other significant PM_{10} source areas for Welgegund are central Mozambique (which correlates with high fire frequency, section 4.2, Figure 4-5) and the central west coast of Namibia (which is a well-known dust source, section 3.1, Figure 3-1) (Bryant, 2003; Barnard, 1998).

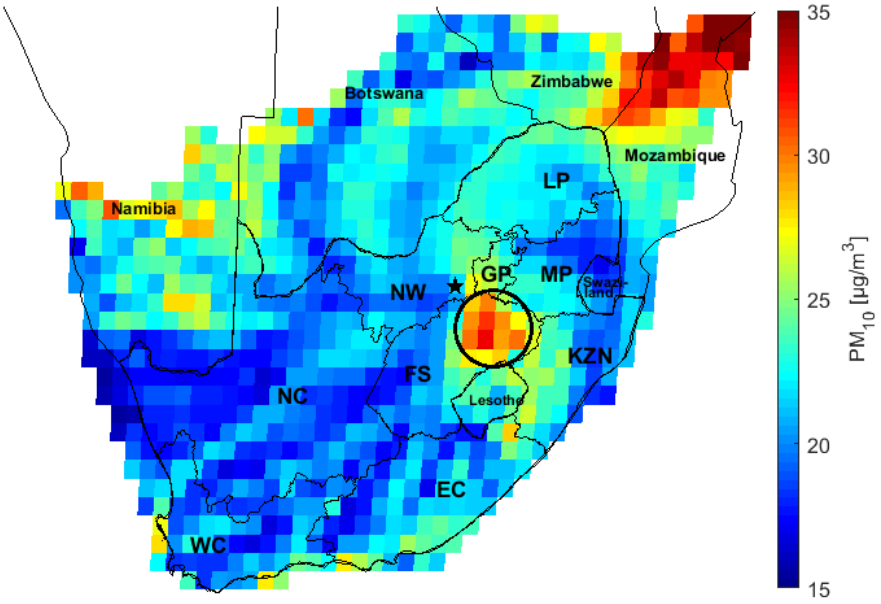

Figure 5-2: Auto-generated source map of average PM_{10} concentrations observed at Welgegund, according to the method by Vakkari *et al*. (2013, 2011). The circled area indicates the eastern Free State.

In addition to the above-mentioned deductions, it is evident from Figures 5-1a and 5-1b that source areas, which are significantly influenced by anthropogenic activities (e.g. Vaal Triangle, Mpumalanga Highveld, Johannesburg-Pretoria megacity) and/or high open biomass burning frequencies (section 4.2, Figure 4-5) and/or higher population density (section 3.1, Figure 3-2) had higher σ_{SP} and σ_{AP} than the relatively clean background in the sector between the west-southwest and south-southwest of Welgegund. It was also interesting to note that KwaZulu-Natal and the Eastern Cape areas that border Lesotho contributed to elevated σ_{AP} levels, more so than for σ_{SP}. These areas are located in escarpment regions, which receive very high rainfall and are prone to relatively high open biomass burning frequencies, as indicated in section 4.2, Figure 4.5. It cannot be speculated from currently available data why open biomass burning in these areas would emit more absorptive (e.g. equivalent

black carbon, eBC) than reflective species (e.g. OA), if compared to other areas. However, this should be investigated in more detail in future.

5.2.1.2 ω_0

From Figure 5-3, presenting the ω_0 auto-generated source map, it is clear that more scattering aerosols originate for areas that have higher open biomass burning frequencies (section 4.2, Figure 4-5), higher population densities (section 3.1, Figure 3-2) and higher concentrations of large point sources (section 3.1, Figure 3-1). The dominant scattering nature of aerosols from these areas results in higher ω_0, than the ω_0 of air masses that have passed over the sector between the west-southwest and south-southwest of Welgegund. In addition, the area over which air masses had passed that had the highest ω_0 corresponds relatively well with the dominant anti-cyclonic recirculation path of air masses that transport emissions from the industrial hub of South Africa (section 3.1, Figure 3-4), which is again evidence of the anthropogenic influence on the aerosol optical properties.

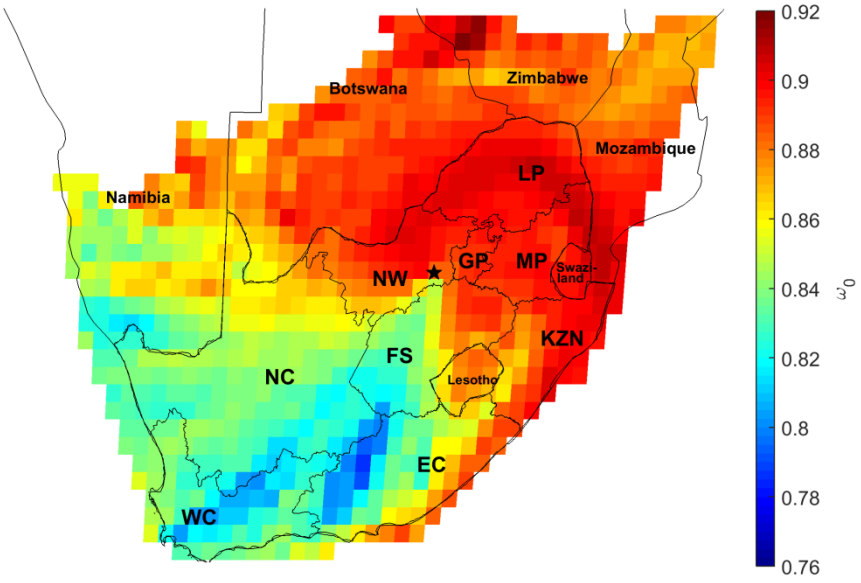

Figure 5-3: Auto-generated source map of the average ω_0 observed at Welgegund for the entire measurement period, according to the method introduced by Vakkari *et al*. (2013, 2011)

5.2.1.3 α_{SP}

Figure 5-4 presents the α_{SP} auto-generated source map for Welgegund. Similar to the deduction made for the ω_0 (section 5.2.1.2, Figure 5-3), it is evident from Figure 5-4 that smaller particles originate from areas that have higher open biomass burning frequencies (section 4.2, Figure 4-5), higher population densities (section 3.1, Figure 3-2), and higher concentrations of large point sources (section 3.1, Figure 3-1), while larger particles are observed in air masses that have passed over the sector between the west-southwest and south-southwest of Welgegund.

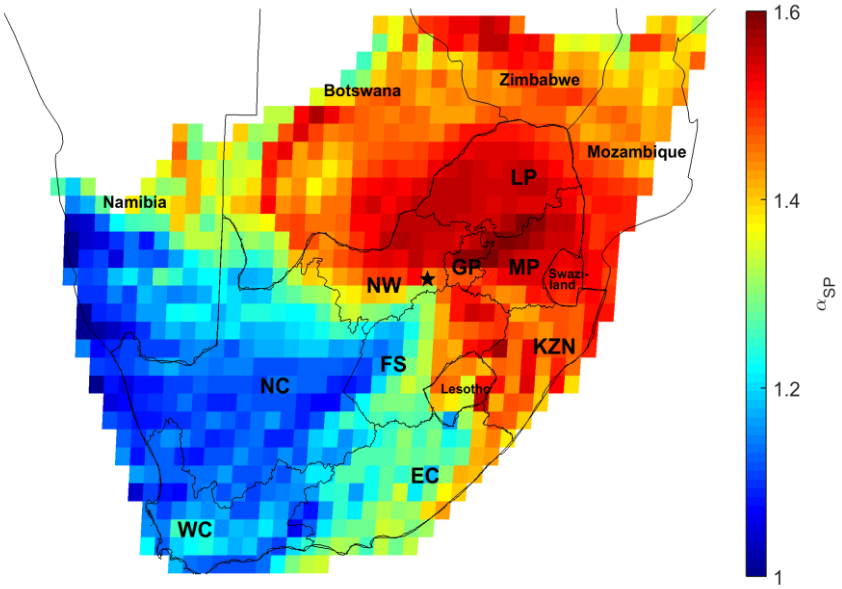

Figure 5-4: Auto-generated source map of the average α_{SP} observed at Welgegund for the entire measurement period, according to the method introduced by Vakkari *et al*. (2013, 2011)

5.2.2 Auto-generated source maps for selected periods

From Figures 5-1, 5-3 and 5-4, source deductions could be made that were relevant for the entire measurement period. In order to isolate the influence of the various sources better, source maps were drawn for σ_{SP} (Figure 5-5), σ_{AP} (Figure 5-6), ω_0 (Figure 5-8) and α_{SP} (Figure 5-9) for three distinct periods:

(a) The warmest (section 4.1, Figure 4-1) and wettest (section 4.1, Figure 4-3) period, i.e. December, January and February, when almost no open biomass

burning occurred (section 4.2, Figure 4-4) and domestic combustion for space heating was insignificant.

(b) The coldest period, i.e. June and July (section 4.1, Figure 4-1), when domestic combustion was most prevalent, while open biomass burning did not yet reach a maximum (section 4.2, Figure 4-4).

(c) The driest period (section 4.1, Figure 4-3), with the highest open biomass burning frequencies (section 4.2, Figure 4-4). The latter was defined as 15 August to 15 October, since June to approximately 15 August is the coldest period, during which significant contributions from domestic space heating can be expected.

5.2.2.1 σ_{SP}

During the warmest/wettest period, the σ_{SP} was highest in air masses that had passed over the Johannesburg-Pretoria (Jhb-Pta) megacity, the Mpumalanga Highveld and the Vaal Triangle (Figure 5-5a), which reflects the contribution of industrial emissions (section 3.1, Figure 3-1). Similar high values were observed for the eastern Free State, which likely represent the influence of wind-blown dust emanating from agricultural activities, as indicated earlier (Figure 5-2). Slightly lower values, but still elevated, were observed in air masses that followed the typical anti-cyclonic recirculation pattern.

During the coldest period (Figure 5-5b), the highest σ_{SP} values were observed in air masses that had passed over a similar, but slightly larger area, than observed for the highest σ_{SP} in the warmest/wettest period (Figure 5-5a). This extended area reflects the population density, which is highest in the Gauteng Province (section 3.1, Figure 3-2). Therefore, although the influence of industrial activities and open biomass burning could not totally be eliminated by focusing on the coldest period, the aforementioned result clearly indicates the regional influence of domestic combustion for space heating.

In contrast to the above-mentioned, σ_{SP} was highest in air masses that had passed over eastern Zimbabwe and central Mozambique during the driest period (Figure 5-

5c) when open biomass burning peaked. Additionally, during the same time, the significant contribution of wind-blown dust from the eastern Free State was evident.

In order to evaluate the σ_{SP} values statistically, a t-test was performed for each period combination. The t-test evaluation between the warmest/wettest and coldest period values, and the warmest/wettest and peak, open biomass burning period values had p-values of 0.11 and 0.61, respectively. This indicated that the σ_{SP} values between the warmest/wettest and coldest periods, and warmest/wettest and peak, open biomass burning periods weren't statistically different. Although not statistically different, a clear visual distinction could be made on the auto-generated source maps between these periods. The t-test evaluation between the coldest and peak, open biomass burning period values resulted in a p-value of 0.05, which indicated that the σ_{SP} values of these two periods were statistically different.

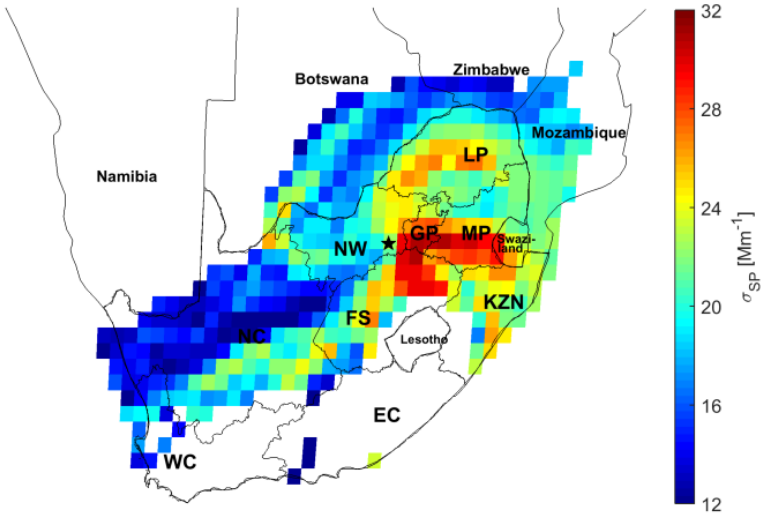

(a)

Figure 5-5: Auto-generated source maps of average σ_{SP} observed at Welgegund for the (a) warmest/wettest, (b) coldest and (c) driest periods, according to the method introduced by Vakkari *et al*. (2013, 2011)

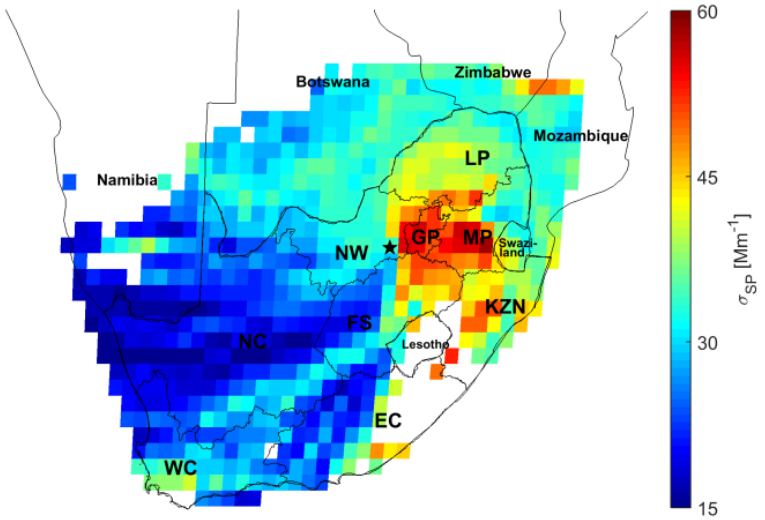

(b)

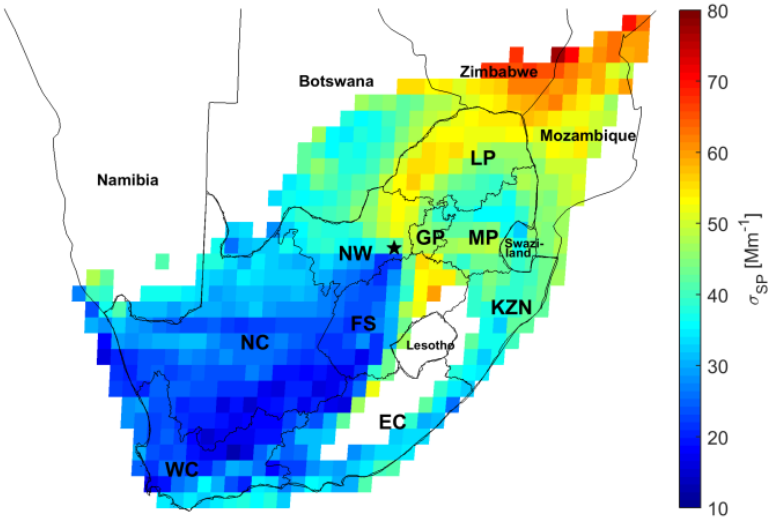

(c)

Figure 5-5: continue; Auto-generated source maps of average σ_{SP} observed at Welgegund for the (a) warmest/wettest, (b) coldest and (c) driest periods, according to the method introduced by Vakkari *et al*. (2013, 2011)

5.2.2.2 σ_{AP}

The σ_{AP} was the highest in air masses that had passed over the Mpumalanga Highveld, Jhb-Pta megacity and KwaZulu-Natal during the wettest/hottest period (Figure 5-6a), indicating the contribution of industrial activities.

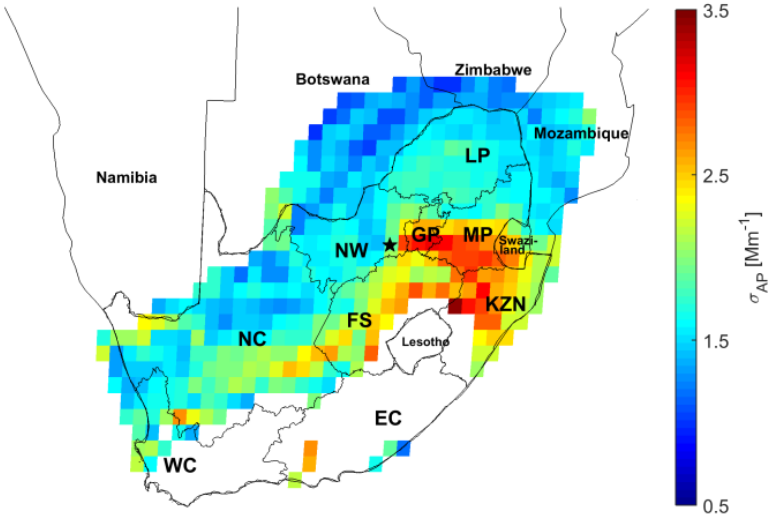

(a)

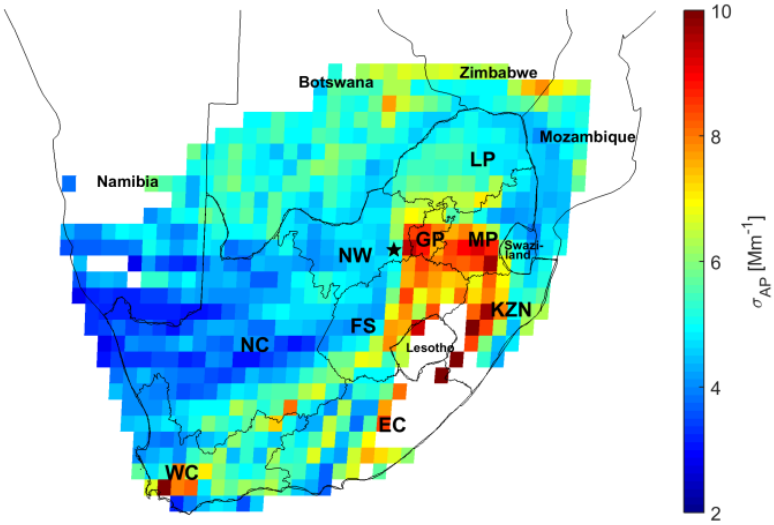

(b)

Figure 5-6: Auto-generated source maps of average σ_{AP} observed at Welgegund for the (a) warmest/wettest, (b) coldest and (c) driest periods, according to the method introduced by Vakkari *et al*. (2013, 2011)

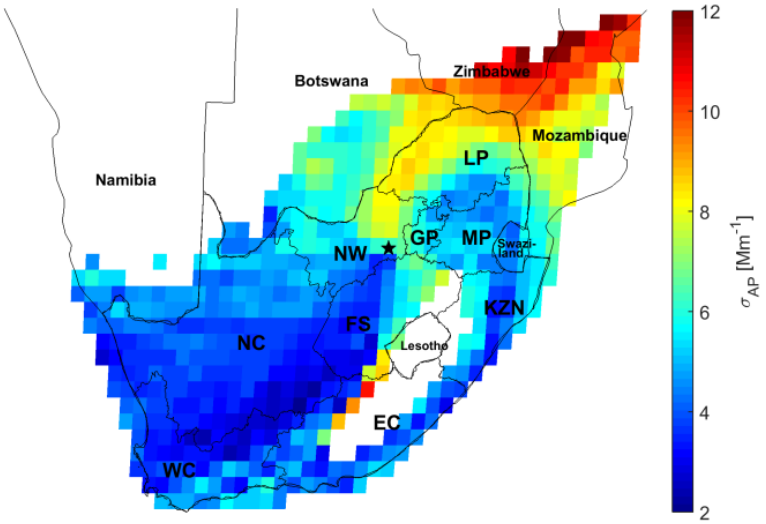

(c)

Figure 5-6: continue; Auto-generated source maps of average σ_{AP} observed at Welgegund for the (a) warmest/wettest, (b) cold and (c) driest periods, according to the method introduced by Vakkari *et al*. (2013, 2011)

Higher values for σ_{AP} in air masses that passed over a similar area as the high values observed during the warmest/wettest period can be observed during the coldest period (Figure 5-6b). This indicates the contribution of domestic combustion for space heating, as mentioned previously, in addition to the industrial activities identified in Figure 5-6a. It was also very interesting to note that the Cape Town area was indicated in Figure 5-6b as a potential source of higher σ_{AP} measured at Welgegund. During the coldest period, it is well known that cold fronts approach South Africa from the southwest (Figure 5.7, Techcentral, 2019). Therefore, although the auto-generated source map (Figure 5-6b) is not conclusive evidence that emissions from the larger Cape Town area contribute to elevated σ_{AP} measured at Welgegund, it supports the notion that it is possible. Additionally, statistically, enough trajectories (section 5.1) had passed over the larger Cape Town area to enable the auto-generated source map to classify it during the coldest period (Figure 5-6b), while this was not the case for the warmest/wettest period (Figure 5-6a). It is also noteworthy to mention that census data indicate a significant population growth for the Cape Town Metropolitan area, from 2.56 to 3.74 million inhabitants between 1996 and 2011 (more recent data were not available) (StatsSA, 2019). Most of this growth can likely be attributed to increasing population in semi- and informal settlements, wherein domestic combustion is prevalent. The possible episodic

transport of pollution from the Cape Town area to Welgegund should be investigated in greater detail in future.

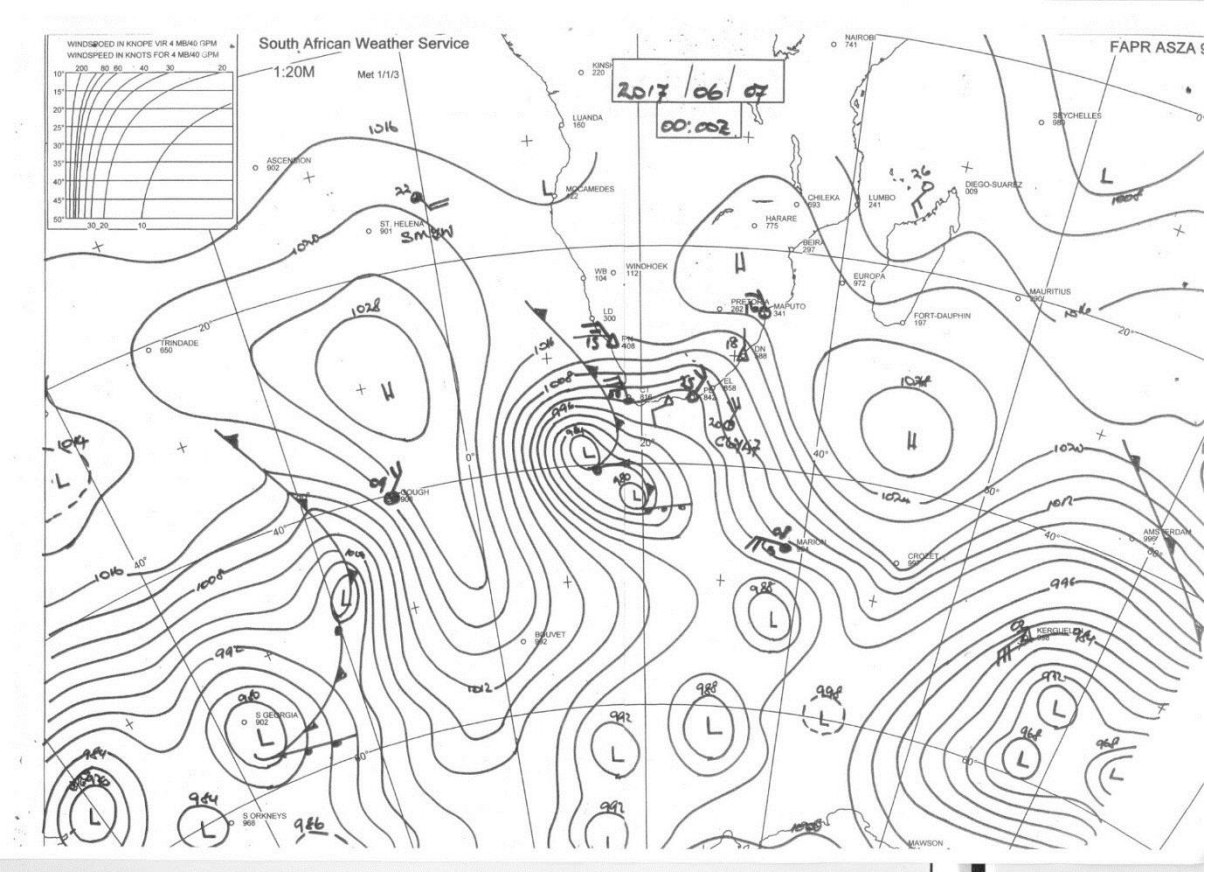

Figure 5-7: Synoptic chart of midnight, 7 June 2017, indicating the presence of a cold front approaching South Africa from the southwest (image: South African Weather Service, Techcentral, 2019)

From Figure 5-6c, which presents the auto-generated source map of σ_{AP} during the driest peak open biomass burning period (15 August to 15 October), it is evident that the highest σ_{AP} values were observed in air masses that had passed over eastern Zimbabwe and central Mozambique. These areas were previously identified as having some of the highest open biomass burning frequencies within the spatial area considered (section 4.2, Figure 4-5). In contrast, the lowest σ_{AP} values were observed in air masses that had passed over the sector west to south-west of Welgegund (i.e. regional background), during this period.

In order to evaluate the σ_{AP} values statistically, a t-test was performed for each period combination. The t-test evaluation between the warmest/wettest and coldest

period values, and the warmest/wettest and peak, open biomass burning period values had p-values of 0.05 and 0.04, respectively. This indicated that the σ_{AP} values between the warmest/wettest and coldest periods, and warmest/wettest and peak, open biomass burning periods were statistically different. The t-test evaluation between the coldest and peak, open biomass burning period values had a p-value of 0.65, which indicated that the σ_{AP} values of these two periods weren't statistically different. Although not statistically different, a clear visual distinction could be made on the auto-generated source maps between these two periods.

5.2.2.3 ω_0

Figure 5-8 presents the ω_0 auto-generated source maps for the three identified periods. As in all other ω_0 discussions, it should be remembered that ω_0 is the combined effect of σ_{SP} and σ_{AP} (Section 3.4.1). Therefore, the σ_{SP} and σ_{AP} auto-generated source maps for the three identified periods should be considered to explain the observed ω_0 source maps. As an example, σ_{SP} and σ_{AP} were highest in air masses that had passed over eastern Zimbabwe and central Mozambique during the driest period (Figures 5-5c and 5-6c); however, in the correlating ω_0 source map (Figure 5-8c), this area had moderate ω_0 values that were lower than the Mpumalanga Highveld. A feature that is common to all the ω_0 auto-generated source maps for the three identified periods is that lower ω_0 values were observed in air masses that had passed over the sector between the west-southwest and south-southwest of Welgegund. In contrast, higher ω_0 values were observed in air masses that had passed over areas that have higher open biomass burning frequencies (section 4.2, Figure 4-5), higher population densities (section 3.1, Figure 3-2) and higher concentrations of large point sources (section 3.1, Figure 3-1).

In order to evaluate the ω_0 values statistically, a t-test was performed for each period combination. The t-test evaluation between the warmest/wettest and coldest period values had p-value of 0.09. This indicated that the ω_0 values between the warmest/wettest and coldest periods were statistically different. The t-test evaluation between the warmest/wettest and peak, open biomass burning period values, and coldest and peak, open biomass burning period values had p-values of 0.38 and 0.38, respectively, which indicated that the ω_0 values of these periods weren't

statistically different. Although not statistically different, a clear visual distinction could be made on the auto-generated source maps between these two periods.

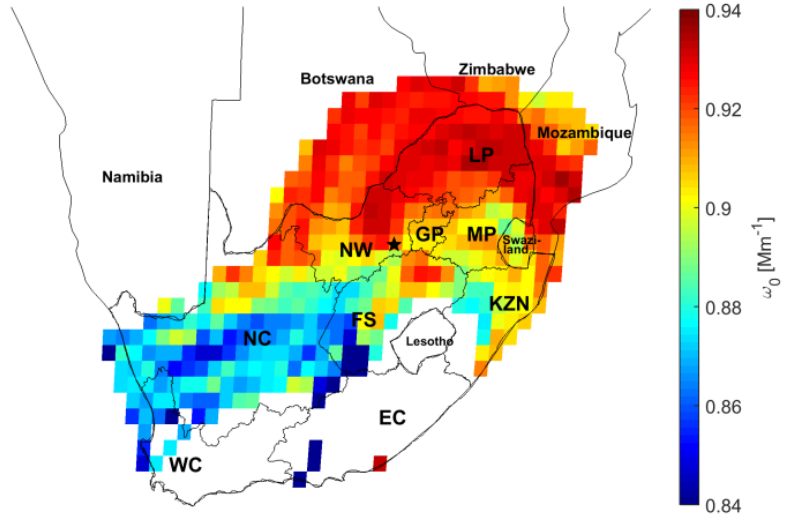

(a)

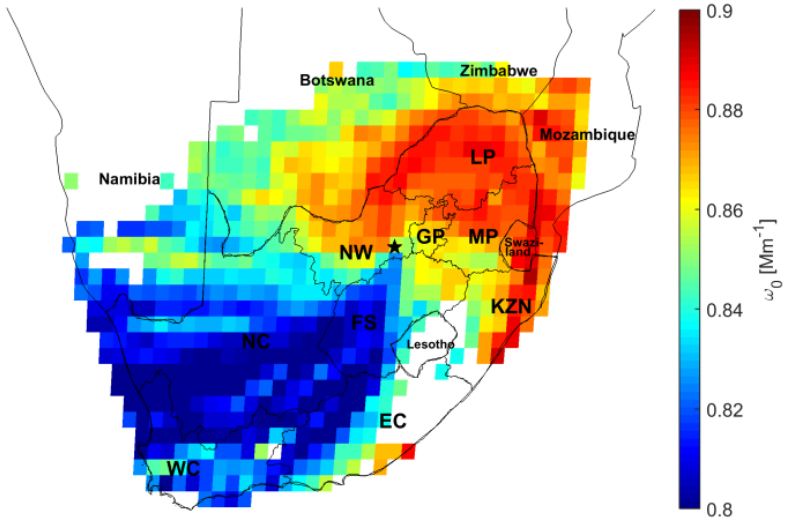

(b)

Figure 5-8: Auto-generated source maps of average ω_0 observed at Welgegund for the (a) warmest/wettest, (b) coldest and (c) driest periods, according to the method introduced by Vakkari *et al*. (2013, 2011)

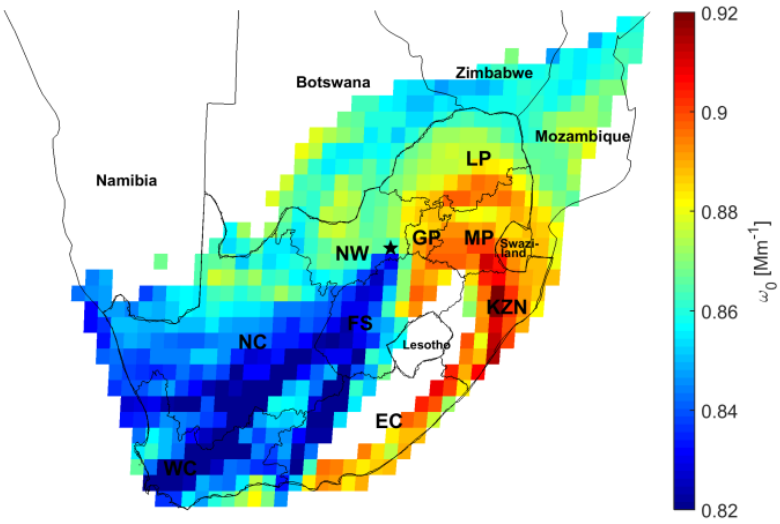

(c)

Figure 5-8: continue; Auto-generated source maps of average ω_0 observed at Welgegund for the (a) warmest/wettest, (b) coldest and (c) driest periods, according to the method introduced by Vakkari *et al*. (2013, 2011)

5.2.2.4 α_{SP}

As was the case for so many of the previous auto-generated source maps, the α_{SP} values observed in air masses that had passed over the sector between the west-southwest and south-southwest of Welgegund were lower (implying larger particles, generally associated with natural sources such as wind-blown dust) for all the three identified periods (Figures 5-9a, b and c). In contrast, higher α_{SP} values (implying smaller particles) were observed in air masses that had passed over areas that have higher open biomass burning frequencies (section 4.2, Figure 4-5), higher population densities (section 3.1, Figure 3-2) and higher concentrations of large point sources (section 3.1, Figure 3-1).

An interesting feature of the α_{SP} source map for the wettest/warmest period (Figure 5-9a) is that elevated α_{SP} values (i.e. smaller particles) were observed in air masses that had passed over Botswana. Although a similar feature was not the most obvious feature in the corresponding σ_{SP} auto-generated source map (Figure 5-5a), it was evident. The only possible explanation for this feature, i.e. increase in small particles that are reflective during the warmest/wettest period, is biogenic emissions in this part of the savannah biome that are converted to OA. The reason(s) why this specific

part of the savannah biome is different could not be explained, but should be investigated in future studies.

For the coldest period (Figure 5-9b), higher α_{SP} values were evident over the entire Gauteng Province (highest population density, section 3.1, Figure 3-2), if compared with the other two periods (Figures 5-9a and c). This indicates the effect of domestic combustion for space heating. Similar to what was observed during the coldest period for σ_{AP} (Figure 5-6b), evidence for possible transport of aerosol pollution from the Western Cape is also observed in Figure 5-9b.

In order to evaluate the α_{SP} values statistically, a t-test was performed for each period combination. The t-test evaluation between all period combinations, i.e. warmest/wettest and coldest period values, the warmest/wettest and peak, open biomass burning period values and coldest and peak, open biomass burning period values, had p-values of 0.19, 0.06 and 0.75, respectively, indicating that the α_{SP} values of these periods weren't statistically different. Although not statistically different, a clear visual distinction could be made on the auto-generated source maps between these two periods.

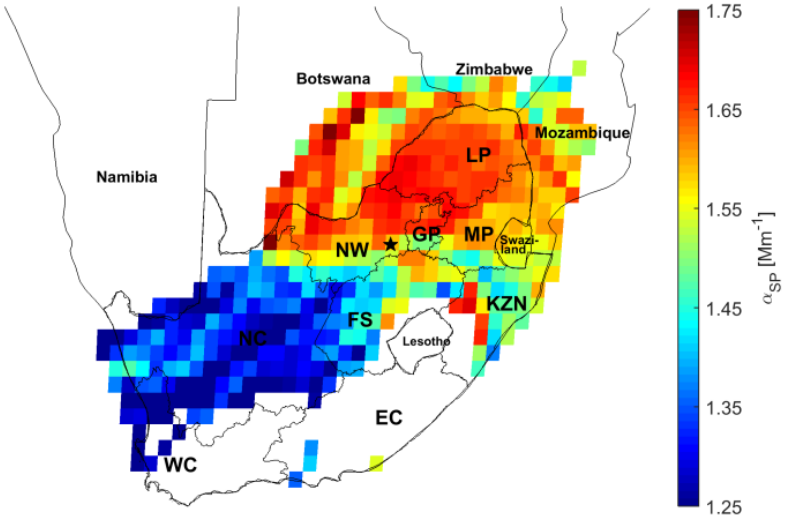

(a)

Figure 5-9: Auto-generated source maps of average α_{SP} observed at Welgegund for the (a) warmest/wettest, (b) coldest and (c) driest periods, according to the method introduced by Vakkari *et al*. (2013, 2011)

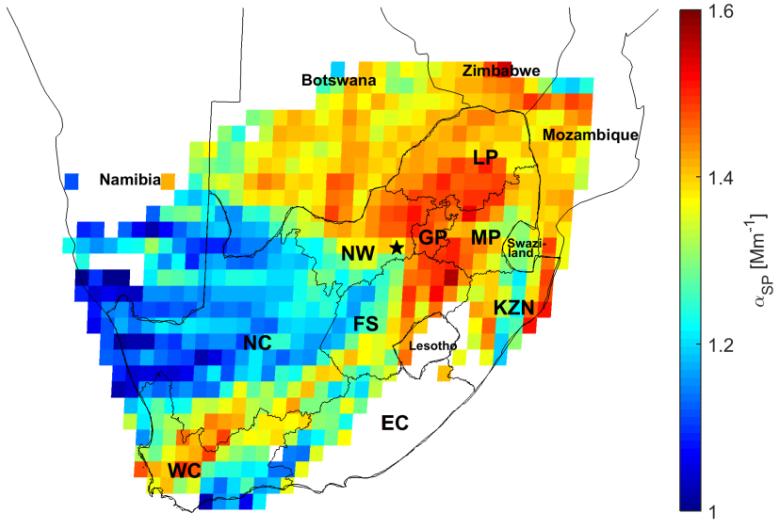

(b)

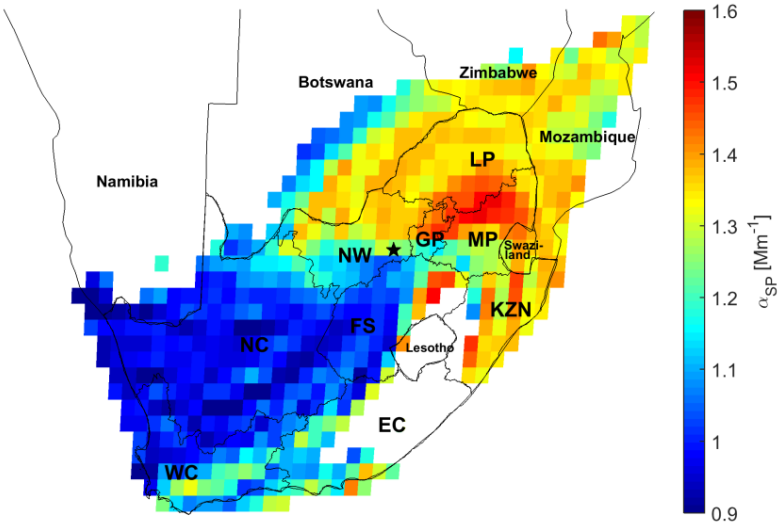

(c)

Figure 5-9: continue; Auto-generated source maps of average α_{SP} observed at Welgegund for the (a) warmest/wettest, (b) coldest and (c) driest periods, according to the method introduced by Vakkari *et al*. (2013, 2011)

5.3 Defined source regions

In this section, defined source regions, based on prior knowledge and information obtained from the auto-generated source maps, i.e. identification of specific source regions such as background and anthropogenic regions, are considered. These source regions were defined by applying three different methods. Firstly, in section 5.3.1, only two source regions were defined. Secondly, in section 5.3.2, the areas

that are influenced most by anthropogenic activities (e.g. high industry and population densities) and where most frequent recirculation of air masses occurs, were defined as source regions. Thirdly, in section 5.3.3, some of the afore-mentioned source regions (section 5.3.2) were combined, while the regional background was divided into two source regions, based on insight obtained from the auto-generated source maps.

5.3.1 Predefined eastern and western sectors

Figure 5-10 presents a map combining population density and open biomass burning frequency (2012 as an example) information. The two solid black lines in this figure indicate how southern Africa can be divided into two sectors, as observed from Welgegund, i.e. eastern and western sectors. The eastern sector contains significantly more anthropogenic point and area sources (section 3.1, Figure 3-1), has a higher population density and significantly more open biomass burning occurs there than in the western sector. In contrast, the western sector has fewer anthropogenic point and area sources, as well as significantly lower population density and open biomass burning frequency.

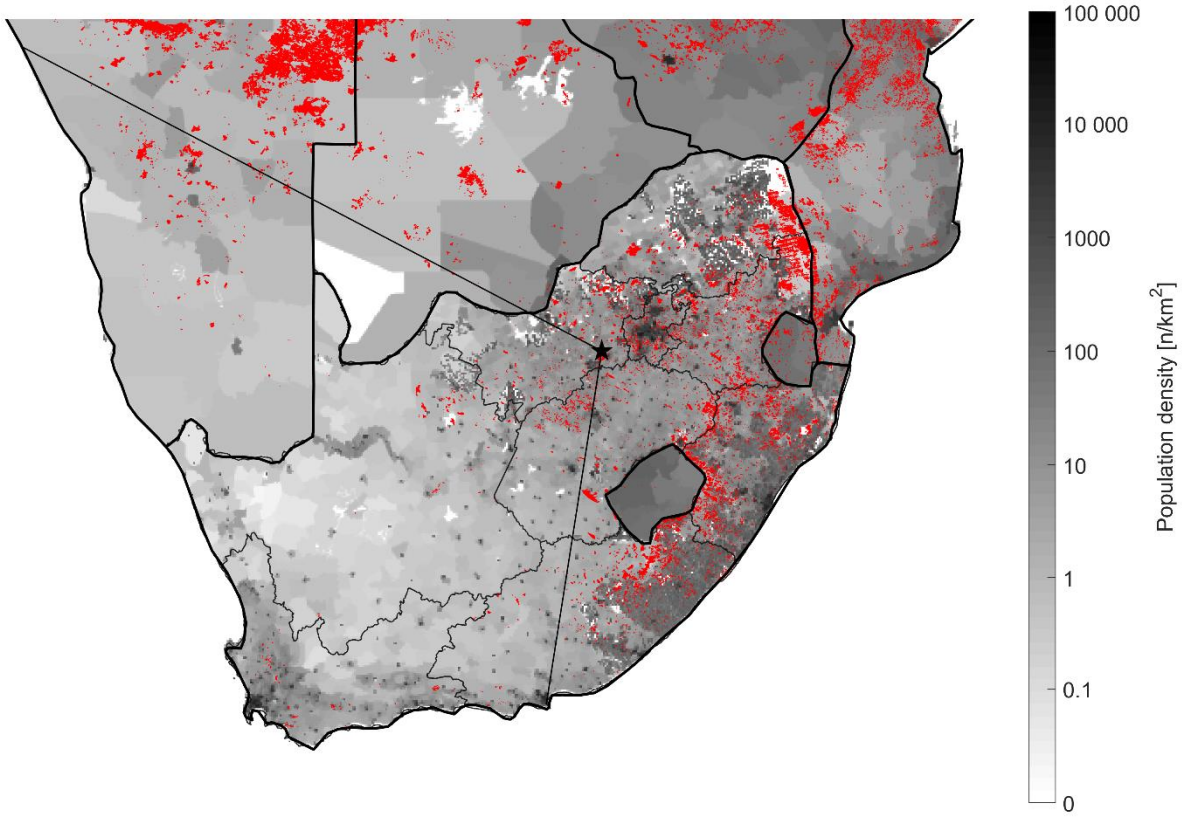

Figure 5-10: A map of southern Africa indicating the population density (CIESIN, 2010) and fire pixels observed for 2012 determined with MODIS collection 5 burned area product (Roy *et al*., 2008). The lines indicate the eastern and western sectors, as defined for observations at Welgegund (black star)

Based on the above-mentioned spatial categorisations, air masses sampled at Welgegund can be classified as passing over these two source sectors. Figure 5-11 presents such overlay back trajectory maps (method described in section 3.4.2) for air masses that were classified as passing over the (a) eastern and (b) western sectors during the warmest/wettest months (December, January and February, section 4.1, Figures 4-1 and 4-3), as well as over the (c) eastern and (d) western sectors during the driest period with the highest open biomass burning frequencies (August to mid-October, section 4.2, Figure 4-4) and high probabilities of wind-blown dust.

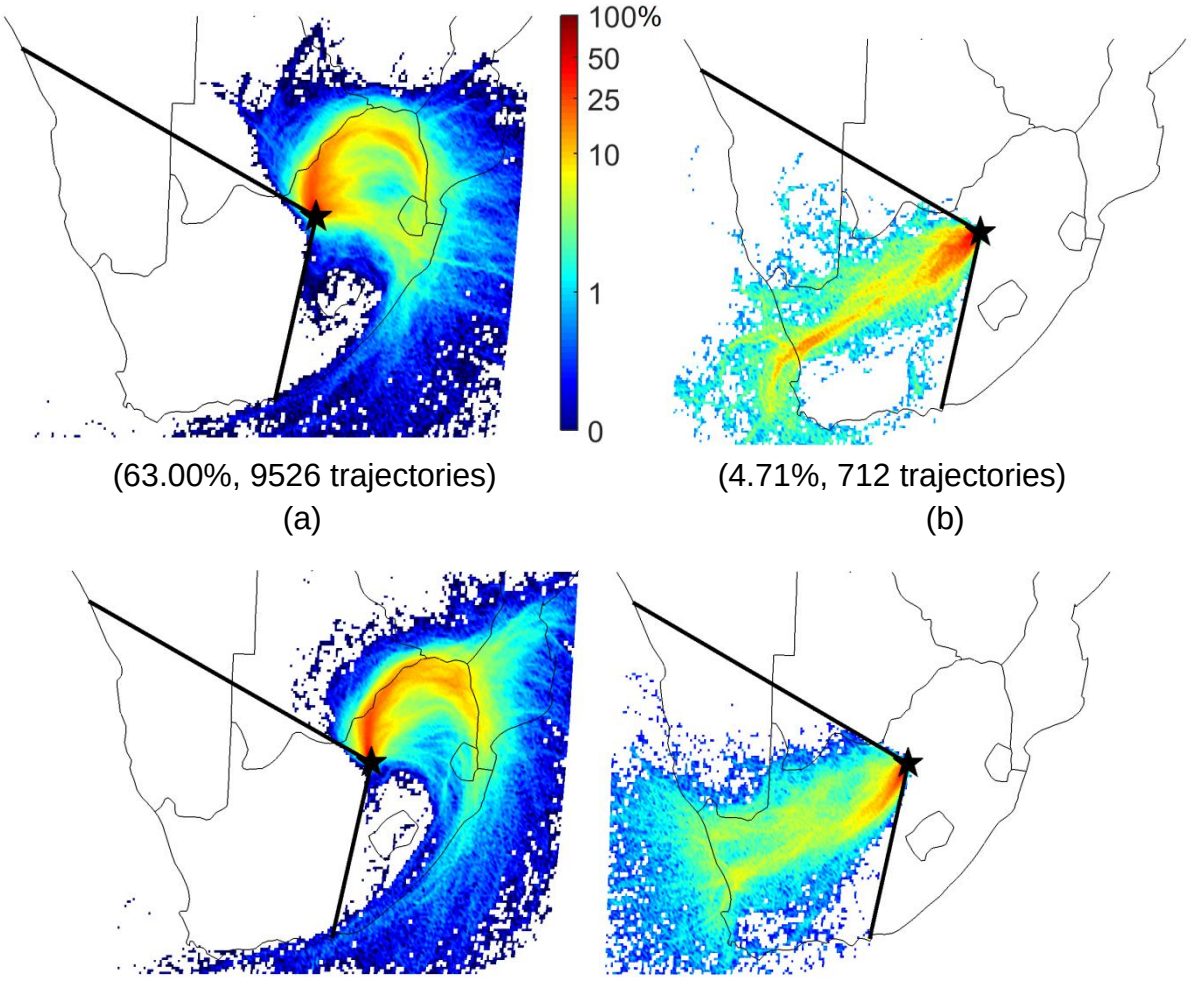

(63.00%, 9526 trajectories)
(a)

(4.71%, 712 trajectories)
(b)

(57.83%, 6067 trajectories)
(c)

(14.06%, 1465 trajectories)
(d)

Figure 5-11: Overlay back trajectory maps of the warmest/wettest period for air masses that had passed over the (a) eastern and (b) western sectors, and the peak open biomass burning period for air masses that had passed over the (c) eastern and (d) western sectors. The percentage values in brackets below each figure indicate what percentage of the overall trajectories could be classified as passing over a specific region, with the actual number of hourly arriving trajectories that this represents next to it

Figures 5-12a and 5-12b, 5-13 and 5-14 present this statistical distribution of the σ_{SP}, σ_{AP}, ω_0 and α_{SP}, respectively, for the air masses that had passed over the eastern and western sectors during the wettest/warmest period and the eastern and western sectors during the peak open biomass burning period.

5.3.1.1 σ_{SP} and σ_{AP}

From Figures 5-12a and b, it is clear that for both the σ_{SP} and σ_{AP}, respectively, air masses that had passed over the eastern sector had significantly higher values than air masses that had passed over the western sector, in corresponding time periods (either comparing warmest/wettest periods with one another, or comparing peak open biomass burning periods with one another). This is due to the eastern sector having considerably more point and area sources (section 3.1, Figure 3-1), having a higher population density and having more productive biomes (section 3.2, Figure 3-1) that lead to more frequent open biomass burning events (Figure 5-10) than the western sector. By comparing the median σ_{SP} and σ_{AP} (Figures 5-12a and b, respectively) of the eastern sector in the warmest/wettest months (σ_{SP} = 18 and σ_{AP} = 1.5 M m^{-1}) with the corresponding values in eastern sector in the peak open biomass burning period (σ_{SP} = 38 and σ_{AP} = 7 M m^{-1}), the contribution of open biomass burning becomes apparent. During the peak open biomass burning period, wind-blown dust can also contribute to the σ_{SP} value due to its scattering nature. Most anthropogenic sources (e.g. industry, vehicles) emit throughout the year, while open biomass burning has a relatively well-defined peak period (section 4.2, Figure 4-4).

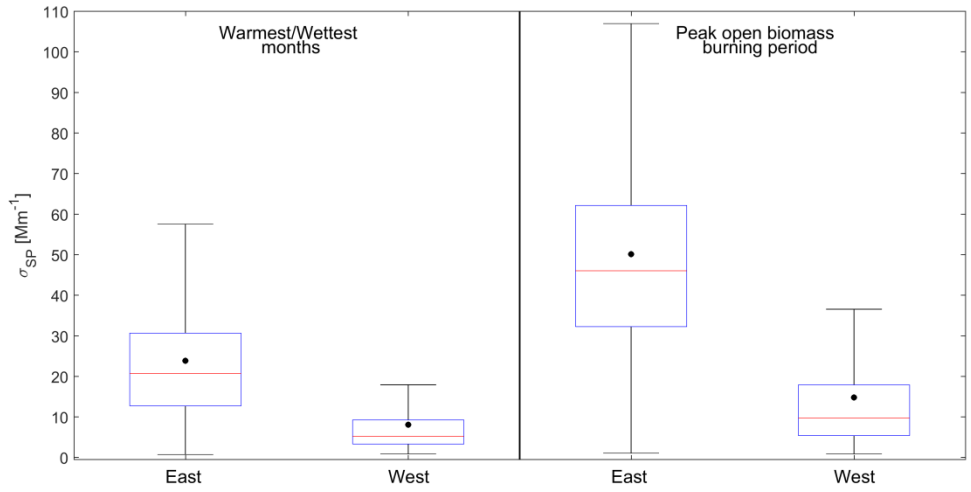

(a)

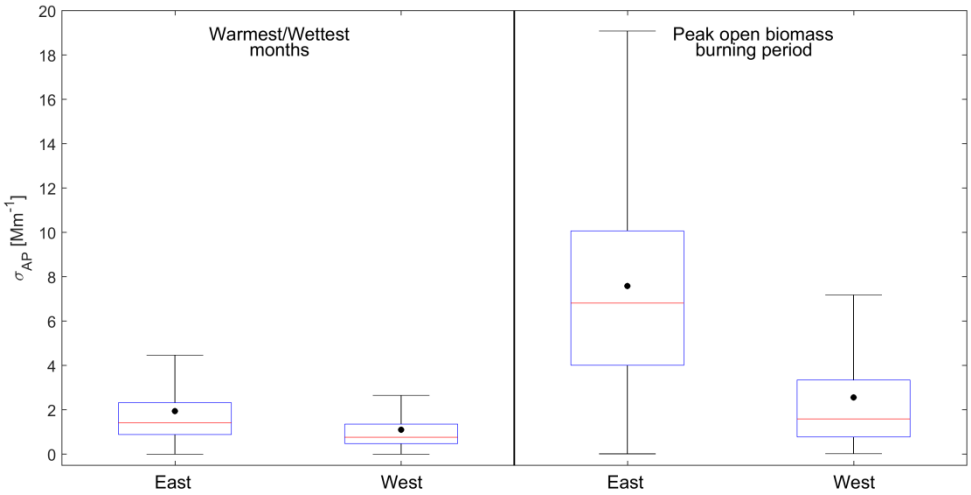

(b)

Figure 5-12: Statistical distribution of the (a) σ_{SP} and (b) σ_{AP} classified according to the warmest/wettest and peak open biomass burning periods, as well as air masses having passed over the eastern and western sectors. The red line represents the median, the black dot the mean, the top and bottom edges of blue boxes the 25th and 75th percentiles and the black whiskers indicate 99.3 % coverage

5.3.1.2 ω_0

From Figure 5-13, it is evident that air masses that had passed over the eastern sector had higher ω_0 values in comparison with air masses that had passed over the western sector in both the warmest/wettest and peak open biomass burning periods. This was expected since more industrial activities and associated polluted aged air masses (containing higher concentration of reflective species such as SO_4^{2-} and

NO_3^-) are observed in the eastern sector. The ω_0 median, i.e. 0.92, of the eastern sector in the warmest/wettest months was significantly higher than the ω_0 median, i.e. 0.85, of the eastern sector in the peak open biomass burning period. As indicated earlier, SO_4^{2-} concentrations are higher during the warmest/wettest months and lower during the drier period (Tiitta *et al.*, 2014) due to lower RH values. More absorptive species, e.g. BC, concentrations are also higher during the dry peak open biomass burning period, which results in a lower ω_0 median in the eastern sector.

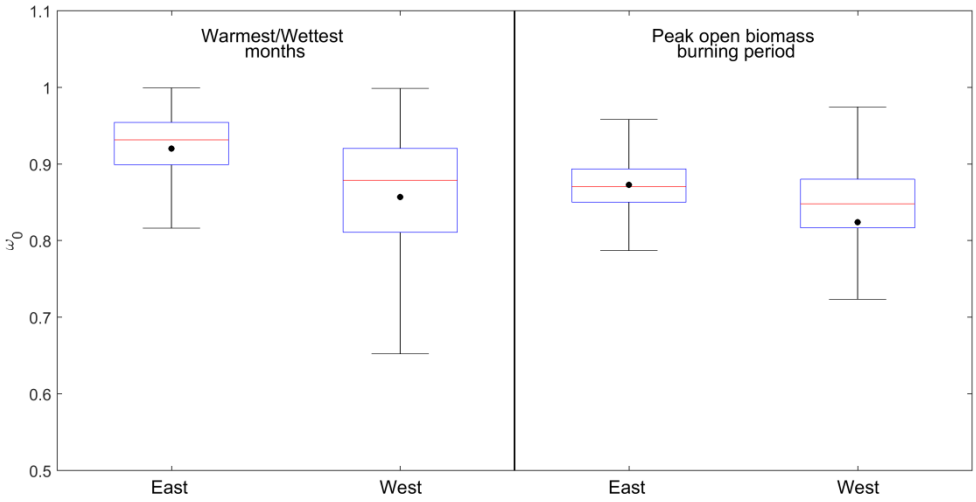

Figure 5-13: Statistical distribution of the ω_0 classified according to the warmest/wettest and peak open biomass burning periods, as well as air masses having passed over the eastern and western sectors. The red line represents the median, the black dot the mean, the top and bottom edges of blue boxes the 25th and 75th percentiles and the black whiskers indicate 99.3 % coverage

5.3.1.3 α_{SP}

From the results in Figure 5-14, presenting the α_{SP}, it is clear that the air masses that had passed over the western sector had larger particle sizes compared to the air masses that had passed over the eastern sector in both the warmest/wettest and the peak open biomass burning periods. This was expected since industrial activities with associated smaller particle size emissions are concentrated in the eastern sector (section 3.1, Figure 3-1), while primary emitted aerosols with larger sizes (e.g. wind-blown dust due to drier biomes, section 3.1, Figure 3-1) contribute fractionally more in the western sector. By comparing the median α_{SP}, 1.6, from the eastern

sector of the warmest/wettest months to the median α_{SP}, 1.3, from the eastern sector of the peak open biomass burning period, it is evident that the eastern sector during the warmest/wettest months had smaller particles. This is likely due to larger fractional contribution of secondary aerosol formation during the warmest/wettest months if compared to the peak open biomass burning periods, and more wind-blown dust particles (that are larger) during the latter period.

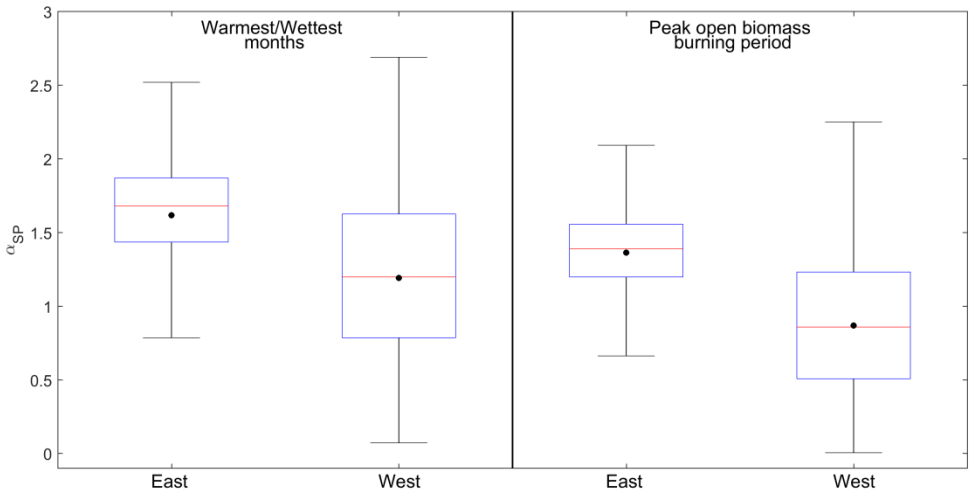

Figure 5-14: Statistical distribution of the α_{SP} classified according to the warmest/wettest and peak open biomass burning periods, as well as air masses having passed over the eastern and western sectors. The red line represents the median, the black dot the mean, the top and bottom edges of blue boxes the 25th and 75th percentiles and the black whiskers indicate 99.3 % coverage

5.3.2 Predefined source and proximity-based source regions

From Figures 5.12a and 5.12b, 5.13 and 5.14 (section 5.3.1), only some source deductions could be made for the eastern and western sectors. To further explore sources in more detail, a significant portion of the eastern sector was divided into five source regions that were defined by Beukes *et al*. (2013), i.e. (a) the Mpumalanga Highveld (HV), (b) the Jhb-Pta megacity (MC), (c) area where air masses moved in an anti-cyclonic recirculation pattern before being measured at Welgegund, which included the Eastern Bushveld Complex (Anti-EBC), (d) Vaal Triangle (VaalT) and (e) Western Bushveld Complex (WBC). Figure 5-15 presents these discernible source regions as observed from Welgegund (mentioned in section 3.1), based on

similarity of sources and proximity of sources to one another (Beukes *et al*., 2013). The regional background (Back) was considered the area not covered by the afore-mentioned source regions. Tiitta *et al*. (2014) and Jaars *et al*. (2014) also applied the source region concept introduced by Beukes *et al*. (2013); therefore, the method used to spatially describe these regions is not repeated here.

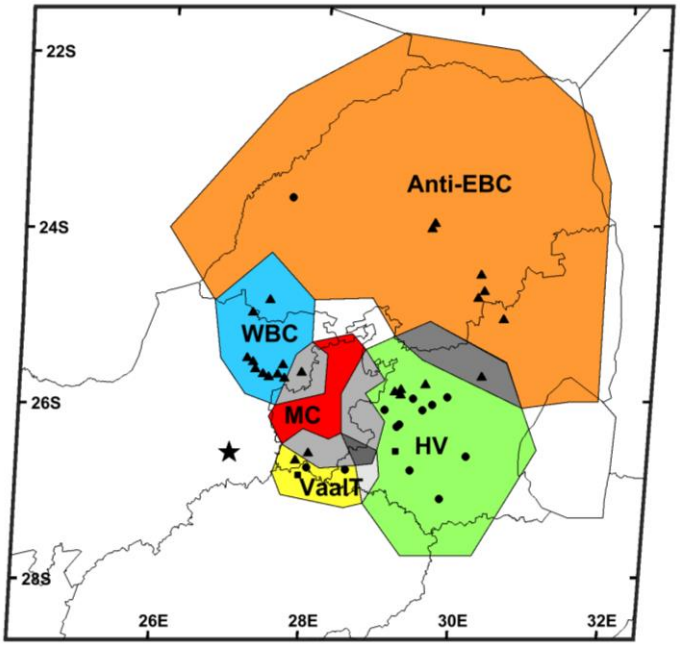

Figure 5-15: The defined five source regions indicated on a regional map. Large point sources in the industrial hub of South Africa are also indicated. The grey areas indicate regions that are classified as 'shared' between neighbouring source regions, according to the method developed by Beukes *et al*. (2013)

Figure 5-16 presents overly back trajectory maps of air mass histories passing over the defined source regions for the entire measurement period. The air mass histories of HV and MC were combined (termed HV-MC), since it was not possible to isolate air masses for one of these source regions without allowing overpass over the other.

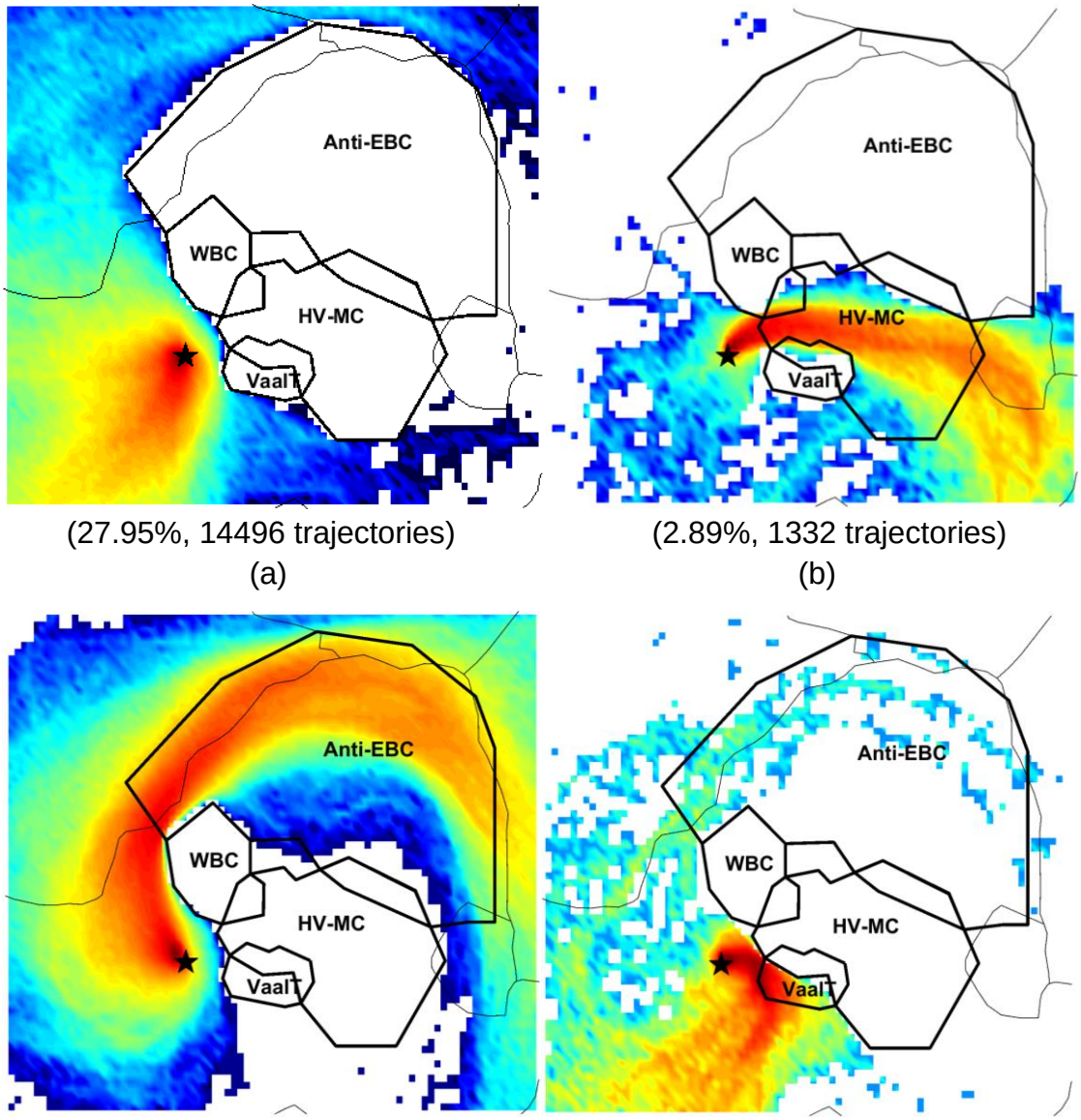

(27.95%, 14496 trajectories)
(a)

(2.89%, 1332 trajectories)
(b)

(19.52%, 10124 trajectories)
(c)

(1.22%, 634 trajectories)
(d)

Figure 5-16: Overlay map of back trajectories passing over the discernible source regions, i.e. (a) regional background (Back), (b) Jhb-Pta megacity and Mpumalanga Highveld (HV-MC), (c) anti-cyclonic recirculation and eastern Bushveld Complex (Anti-EBC), (d) Vaal Triangle (VaalT) and (e) Western Bushveld Complex (WBC), before being measured at Welgegund. The percentage values in brackets below each figure indicate what percentage of the overall trajectories could be classified as passing over a specific region, with the actual number of hourly arriving trajectories that this represents next to it

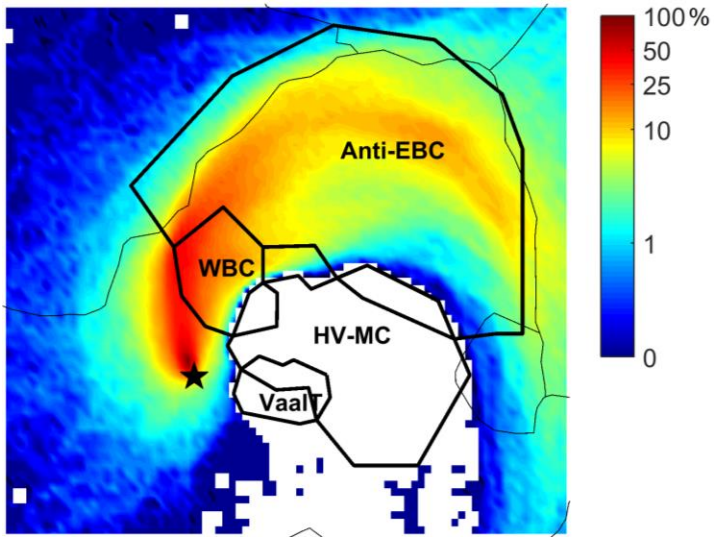

(26.13%, 13554 trajectories)
(e)

Figure 5-16: continue; Overlay map of back trajectories passing over the discernible source regions, i.e. (a) regional background (Back), (b) Jhb-Pta megacity and Mpumalanga Highveld (HV-MC), (c) anti-cyclonic recirculation and eastern Bushveld Complex (Anti-EBC), (d) Vaal Triangle (VaalT) and (e) Western Bushveld Complex (WBC), before being measured at Welgegund. The percentage values in brackets below each figure indicate what percentage of the overall trajectories could be classified as passing over a specific region, with the actual number of hourly arriving trajectories that this represents next to it

Figures 5-17a and 5-17b, 5-18 and 5-19 present the statistical distribution of the σ_{SP}, σ_{AP}, ω_0 and α_{SP}, respectively, for air masses that had passed over the discernible source regions for the entire measurement period.

5.3.2.1 σ_{SP} and σ_{AP}

The median σ_{SP} (Figure 5-17a) was the highest in air masses that passed over the source areas that are most significantly influenced by anthropogenic activities, i.e. HV-MC (23 M m^{-1}), VaalT (28 M m^{-1}) and WBC (25 M m^{-1}). The median σ_{SP} of the Anti-EBC (19 M m^{-1}), which hosts fewer large point (e.g. industries) and area (e.g. informal settlements) sources, was somewhat lower than that of the afore-mentioned source areas, but still higher than that of the Back (9 M m^{-1}). The variance of the σ_{SP}

of the VaalT was the largest, which indicates that the extent of pollution of air masses that pass over this area is variable and additionally it reflects the occurrence of the severe dust storms that travel from the eastern Free State (section 5.2.1.1, Figure 5-2) over the VaalT to Welgegund.

The σ_{AP} that was associated with air mass that had passed over the source regions (Figure 5-17b) indicated a similar pattern to that of the σ_{SP} (Figure 5-17a), with the highest median values for the source areas that are most significantly influenced by anthropogenic activities, i.e. HV-MC (3.5 M m^{-1}) and VaalT (4.1 M m^{-1}), but with WBC (2.9 M m^{-1}) slightly lower. The reason why the median WBC σ_{AP} was lower if compared to σ_{SP} (Figure 5-17a) is because the large point sources in the WBC are mostly pyrometallurgical smelters, which apply reductive (Kleynhans *et al*., 2012) rather than oxidative combustion processes common in the HV-MC and VaalT (Pretorius *et al*., 2015). In addition, a significant number of the afore-mentioned smelters in the WBC are for platinum group metals (PGM), which are known for relatively high SO_2 emissions (Westcott *et al*., 2007). As was the case for the σ_{SP}, the median σ_{AP} of the Anti-EBC (2.1 M m^{-1}) was lower than that of the afore-mentioned source regions, but still higher than that of the Back (1.8 M m^{-1}).

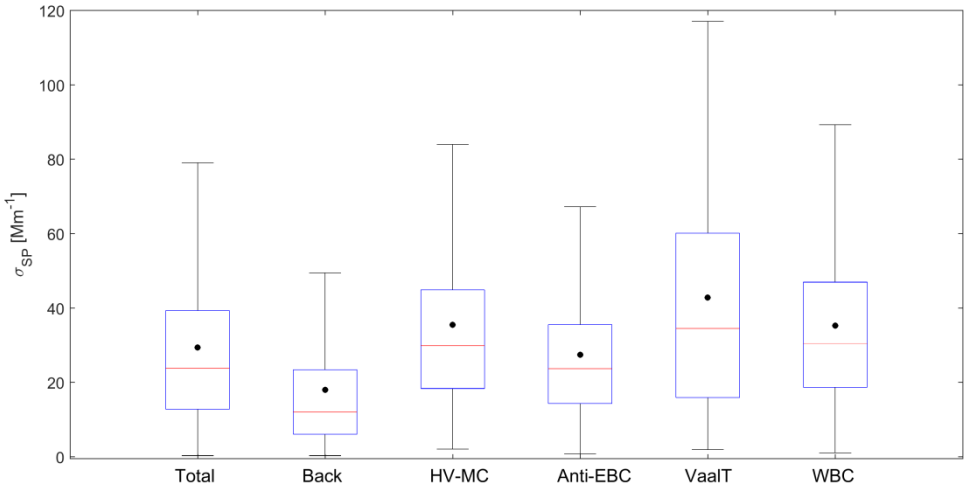

(a)

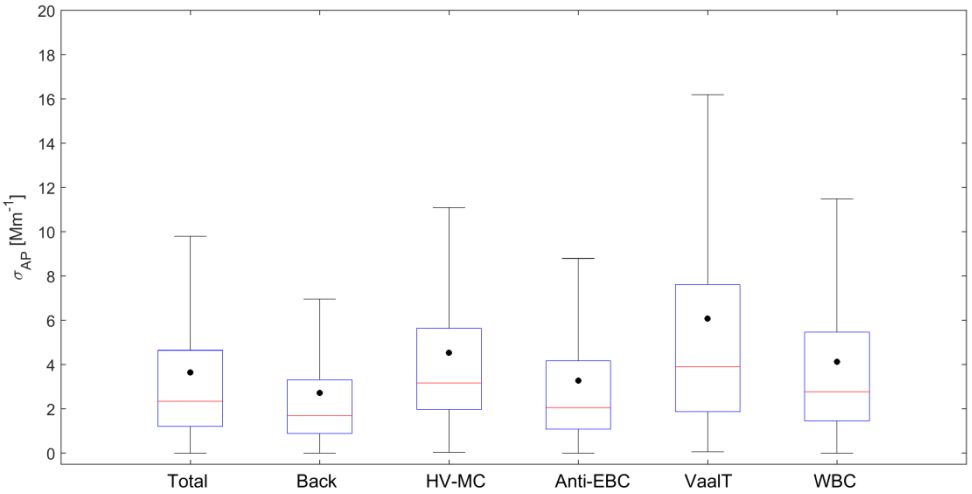

(b)

Figure 5-17: Statistical distribution of (a) σ_{SP} and (b) σ_{AP} for the entire measurement period, which were associated with air mass that had passed over the discernible source regions. The red line represents the median, the black dot the mean, the top and bottom edges of blue boxes the 25th and 75th percentiles and the black whiskers indicate 99.3 % coverage

5.3.2.2 ω_0

Figure 5-18, presenting the ω_0 statistical distribution, indicates that air masses that had passed over Anti-EBC (0.89) and WBC (0.88) were the most reflective. This makes sense, since air masses that had passed over these source regions generally followed an anti-cyclonic recirculation pattern and therefore represent aged polluted

air masses. As previously indicated, the large points sources in these two source regions are mainly pyrometallurgical smelters applying reductive processes (not combustion), but with relatively high SO_2 emissions. SO_4^{2-} is a reflectively species, which forms from SO_2 oxidation. Air mass ageing also results in coating of absorbing particles with OA, increasing the reflectivity thereof. Additionally, recirculated air masses that pass over Anti-EBC and WBC typically also contain aged pollution originating from the HV-MC and the VaalT. In contrast, air masses that travel without significant recirculation from the HV-MC and VaalT to Welgegund had median ω_0 values of 0.87 and 0.85, respectively. The Back had the lowest median ω_0 (0.83). This lower ω_0 median of the Back must not be assumed as natural, since the Back is still significantly impacted by open biomass burning (section 4.2, Figure 4-5), of which a significant fraction of events is anthropogenic (Akagi *et al*., 2011).

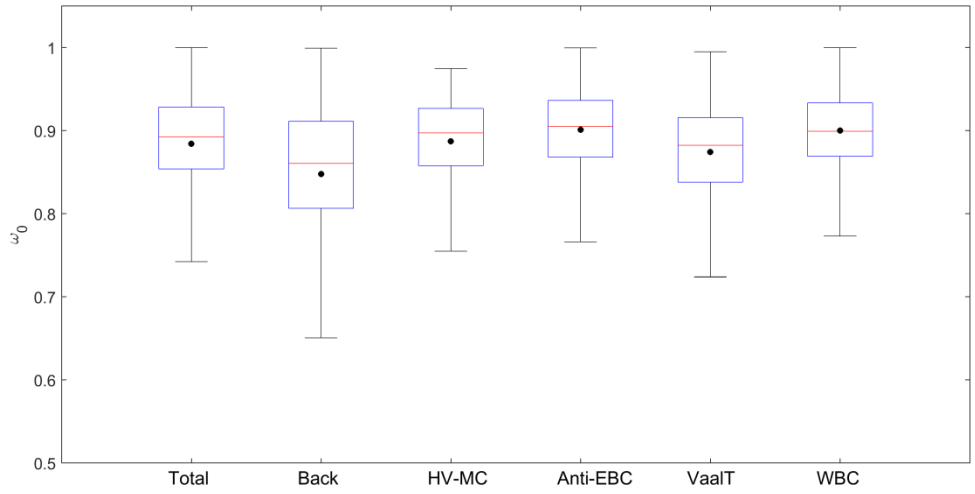

Figure 5-18: Statistical distribution of ω_0 for the entire measurement period, which was associated with air mass that had passed over the five discernible source regions. The red line represents the median, the black dot the mean, the top and bottom edges of blue boxes the 25th and 75th percentiles and the black whiskers indicate 99.3 % coverage

5.3.2.3 α_{SP}

Of the significantly anthropogenically impacted source regions, the α_{SP} median of the VaalT (1.4) was lower than the medians for air masses that had passed over the HV-MC, Anti-EBC and WBC, which were virtually the same (~1.6) (Figure 5-19). The probable reason for the larger median particle size of air masses that had passed

over the VaalT was indicated earlier – severe dust storms that travel from the eastern Free State (section 5.2.1.1, Figure 5-2) pass over the VaalT. The Back had a α_{SP} median (1.3) that was comparable to that of the VaalT, with open biomass burning (that emits larger primary particles than e.g. industrial combustion sources) being the most common source.

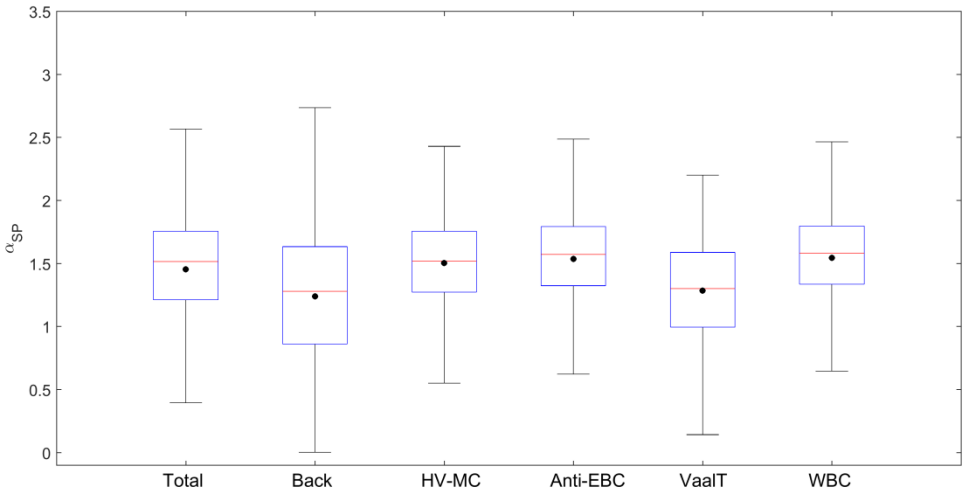

Figure 5-19: A statistical distribution of α_{SP} for the entire measurement period, which was associated with air mass that had passed over the five discernible source regions. The red line represents the median, the black dot the mean, the top and bottom edges of blue boxes the 25th and 75th percentiles and the black whiskers indicate 99.3 % coverage

5.3.3 Combined pre-defined and auto-generated source regions

In this section, insights gained from both the auto-generated source maps (sections 5.2.1 and 5.2.2) and the pre-defined source regions (considered in sections 5.3.1 and 5.3.2) were combined. In the “Predefined source and proximity based source regions” (section 5.3.2) approach, the regional background (Back) was a large undivided area. However, the auto-generated source maps (sections 5.2.1 and 5.2.2) clearly indicated significant differences in aerosol properties of air masses that had passed over the Karoo (west to south-west of Welgegund) and Kalahari (north to west of Welgegund). Therefore, in the current approach, these two background source regions were considered separately. From section 5.3.2, it was evident that air masses that pass over the EBC and WBC before being measured at Welgegund follow the typical anti-cyclonic recirculation pattern. Therefore, these source regions

were considered together as a single source region, termed “anti-cyclonic recirculation pattern”. Lastly, both the auto-generated source maps (sections 5.2.1 and 5.2.2) and the pre-defined source regions (considered in section 5.3.2) showed that the most polluted air masses mostly passed over the HV-MC and VaalT; therefore, these areas were combined and considered as a single source region termed the ‘industrial hub’. Classification of air masses, as having passed over these four source regions during the entire measurement period, is presented in Figure 5-20.

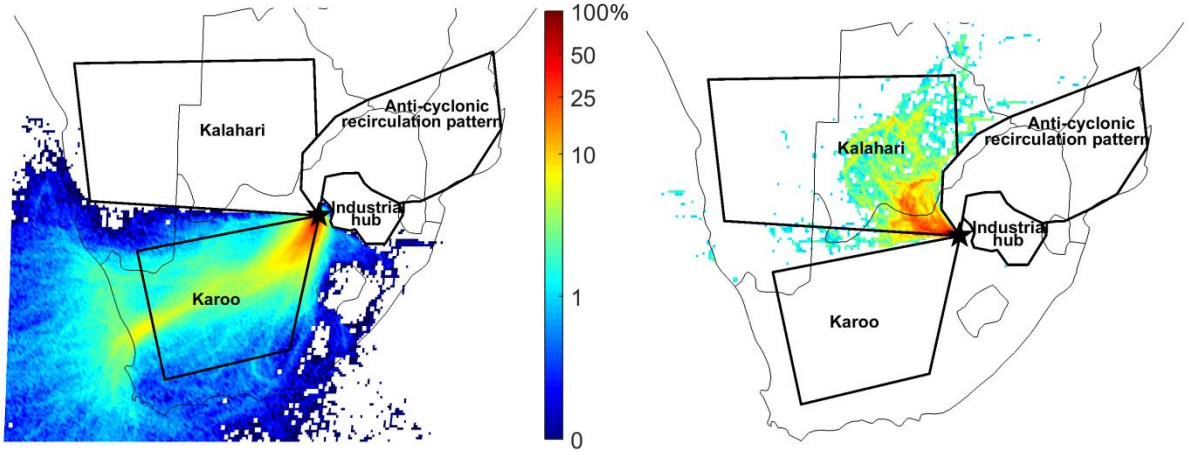

(14.68 %, 6757 trajectories)
(a)

(0.61 %, 279 trajectories)
(b)

Figure 5-20: Overlay back trajectory maps of back trajectories, for the entire measurement period, allocated as passing (spend at least 10 hours) over the (a) Karoo region, (b) Kalahari region, (c) anti-cyclonic recirculation pattern and (d) industrial hub before being sampled at Welgegund. The percentage values in brackets below each figure indicate what percentage of the overall trajectories could be classified as passing over a specific region, with the actual number of hourly arriving trajectories that this represent next to it

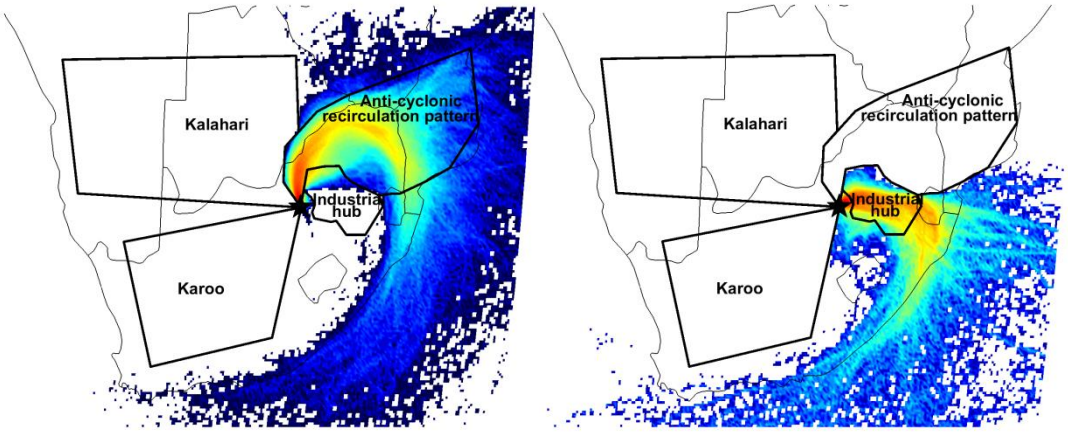

(18.62 %, 8569 trajectories) (c)

(4.79 %, 2203 trajectories) (d)

Figure 5-20: continue; Overlay back trajectory maps of back trajectories, for the entire measurement period, allocated as passing (spend at least 10 hours) over the (a) Karoo region, (b) Kalahari region, (c) anti-cyclonic recirculation pattern and (d) industrial hub before being sampled at Welgegund. The percentage values in brackets below each figure indicate what percentage of the overall trajectories could be classified as passing over a specific region, with the actual number of hourly arriving trajectories that this represent next to it

In the following sections, the statistical distribution of the aerosol optical properties classified according to air masses that had passed over the four defined regions (Figure 5-20) during the three distinct time periods specified, i.e. the warmest/wettest, coldest, as well as driest and peak open biomass burning period, are considered.

5.3.3.1 σ_{SP} and σ_{AP}

From Figure 5-21a, it is evident that the σ_{SP} medians observed for air masses that had passed over the Karoo (6.3 M m^{-1}) and Kalahari (8.3 M m^{-1}) during the warmest/wettest period were similar, while the corresponding medians observed for air masses that had passed over the anti-cyclonic recirculation pattern (20.9 M m^{-1}) and industrial hub (22.5 M m^{-1}) were similar. The σ_{SP} median for the Karoo was approximately 72 % lower than that observed for the industrial hub. During this period (warmest/wettest), low fire frequencies occur (section 4.2, Figure 4-4).

Therefore, this significant difference between the Karoo and the industrial hub (72 % in median σ_{SP}) indicates the dissimilarities in anthropogenic activities (e.g. industrial, traffic, domestic cooking) and biome productivity that are associated with open biomass burning frequencies. Similar observations are evident, from Figure 5-21b, for the σ_{AP} medians during the warmest/wettest period. During this time period, the σ_{AP} median for air masses that had passed over the Kalahari (0.7 M m^{-1}), which were slightly lower than that of the Karoo (1.0 M m^{-1}), was approximately 71 % lower than the σ_{AP} median of air masses passing over the industrial hub (2.3 M m^{-1}).

During the coldest period (Figure 5-21a), air masses that had passed over the industrial hub had the highest σ_{SP} median (53.6 M m^{-1}). This was approximately 82 % higher than the σ_{SP} median observed for air masses that had passed over the Karoo (9.7 M m^{-1}), which had the lowest median. Since open biomass burning frequencies do not yet peak during the coldest period (section 4.2, Figure 4-4), the difference between the afore-mentioned medians reflects the dissimilarity in contribution to σ_{SP} from domestic combustion for space heating and trapping due to lower PBL/stronger inversion layers (Gierens *et al*., 2019; Krohonen *et al*., 2013) between the two regions. Similar observations are evident, from Figure 5-21b, for the σ_{AP} medians during the coldest period. During this time period, σ_{AP} medians for air masses that had passed over the Karoo (2.3 M m^{-1}) and Kalahari (2.2 M m^{-1}) were similar. These medians were approximately 77 to 78 % lower than the σ_{AP} median of air masses passing over the industrial hub (9.7 M m^{-1}).

The σ_{SP} median for air masses that had passed over the Karoo (10.1 M m^{-1}) during the driest, peak open biomass burning period was approximately 80 % lower than the median observed for air masses that had passed over the anti-cyclonic recirculation pattern (50.8 M m^{-1}). In contrast to the previous periods, the σ_{SP} median of the anti-cyclonic recirculation pattern was higher than that of the industrial hub (39.8 M m^{-1}), due to the former region being covered mostly by the more productive (biomass per surface unit) savannah biome, while the latter region is covered by a combination of grassland and savannah biomes (section 3.1, Figure 3-1). The difference between the σ_{SP} medians of the Karoo and the anti-cyclonic recirculation pattern during the driest, peak open biomass burning period, therefore, reflects the dissimilar contributions of the open biomass burning emissions between the two

regions. Similar observations are evident from Figure 5-21b, for the σ_{AP} medians during the driest, peak open biomass burning period. During this time, air masses that had passed over the Karoo (1.8 M m^{-1}) had a σ_{AP} median of approximately 77 % lower than air masses that had passed over the anti-cyclonic recirculation pattern (7.9 M m^{-1}).

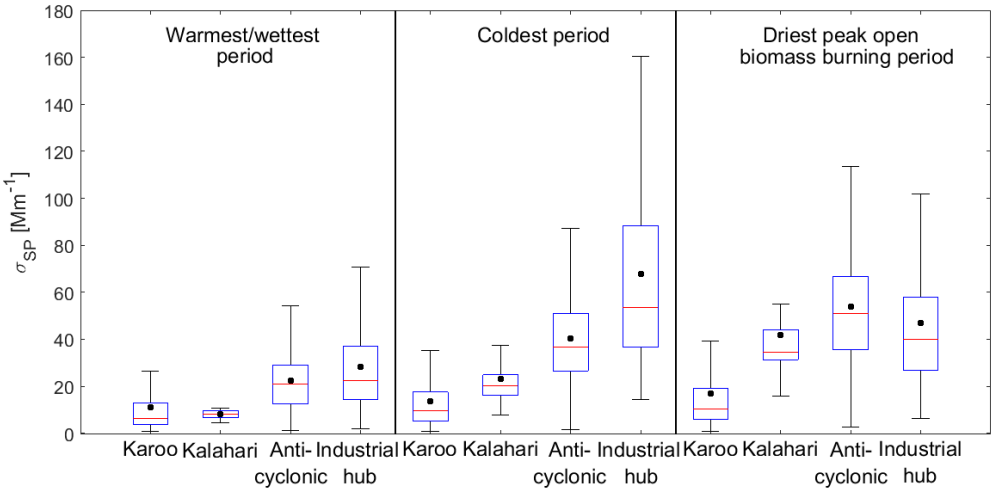

(a)

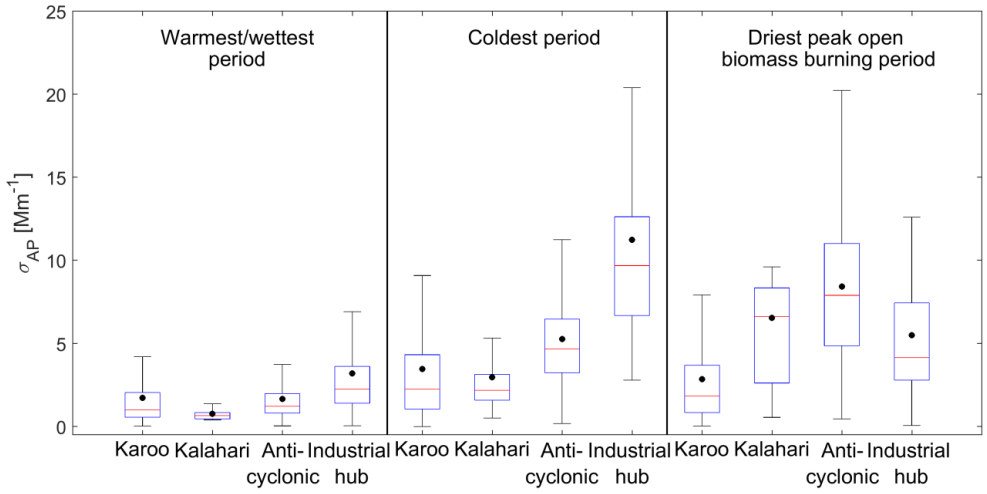

(b)

Figure 5-21: Statistical distribution of the (a) σ_{SP} and (b) σ_{AP} based on air masses that had passed over the area, Karoo region, Kalahari region, the anti-cyclonic recirculation pattern and the industrial hub classified according to the total, warmest/wettest, coldest and driest periods. The red line represents the median, the black dot the mean, the top and bottom edges of blue boxes the 25th and 75th percentiles and the black whiskers indicate 99.3 % coverage

5.3.3.2 ω_0

By considering Figure 5-22, it is evident that the ω_0 medians of air masses that had passed over the Karoo (varying between 0.80 and 0.86) during all the isolated periods (i.e. warmest/wettest; coldest; and driest, peak open biomass burning) were lower than the corresponding medians of the Kalahari (varying between 0.85 and 0.91), anti-cyclonic recirculation pattern (varying between 0.87 and 0.94) and industrial hub (varying between 0.86 and 0.91). For the different time periods, the Karoo ω_0 medians were 9, 12 and 7 % lower than the area with the highest ω_0 median, in the warmest/wettest, coldest, and driest, peak open biomass burning periods, respectively. The difference between the ω_0 medians of the Karoo and the other regions reflects the dissimilar contributions of anthropogenic, fire and biogenic emissions between the Karoo and the other regions during the different time periods.

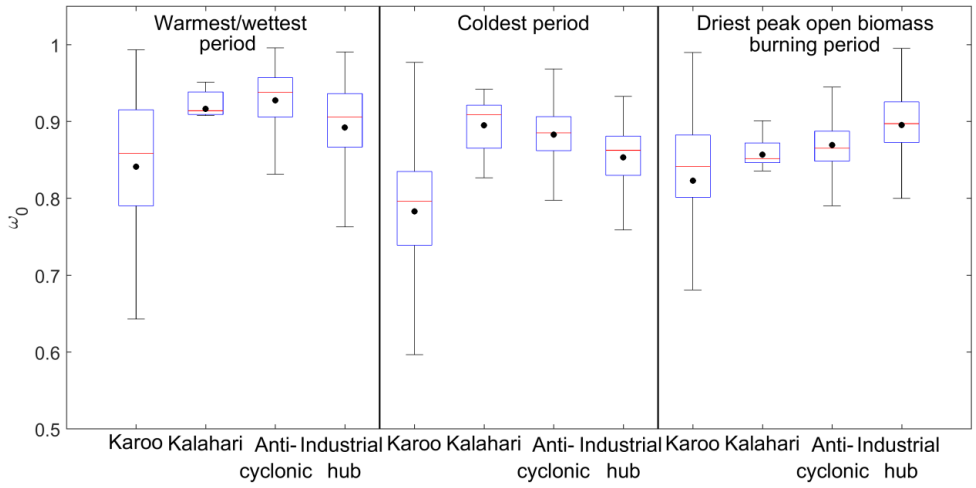

Figure 5-22: Statistical distribution of the ω_0 based on air masses that had passed over the area, Karoo region, Kalahari region, the anti-cyclonic recirculation pattern and the industrial hub classified according to the total, warmest/wettest, coldest and driest periods. The red line represents the median, the black dot the mean, the top and bottom edges of blue boxes the 25th and 75th percentiles and the black whiskers indicate 99.3 % coverage.

5.3.3.3 α_{SP}

In a similar manner as the ω_0 (Figure 5-22), α_{SP} medians (Figure 5-23) of the Karoo (varying between 0.91 and 1.20) were smaller than the corresponding α_{SP} medians of the Kalahari (varying between 1.12 and 1.62), anti-cyclonic recirculation pattern (varying between 1.50 and 1.68) and the industrial hub (varying between 1.28 and 1.54) during all the considered time periods. For the different time periods, the Karoo α_{SP} medians were 29, 29 and 35 % lower than the anti-cyclonic recirculation pattern, which had the highest α_{SP} medians, in the warmest/wettest, coldest, and driest, peak open biomass burning periods, respectively. The afore-mentioned proves that larger particles are typically observed in air masses that had passed over the Karoo, if compared to air masses that had passed over the other defined regions. As previously stated, larger particles are typically associated with natural processes (e.g. wind-blown dust), while finer particles are typically associated with anthropogenic activities and/or biomass burning. Furthermore, the longer aging time of gaseous pollutants present in air masses that had passed over the anti-cyclonic recirculation pattern results in a larger fraction contribution from secondary aerosols, which are smaller than primary particles.

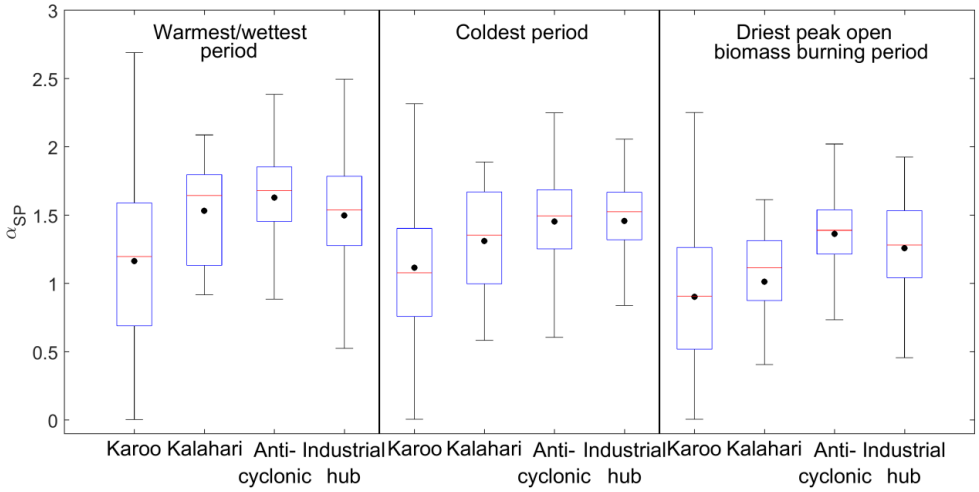

Figure 5-23: Statistical distribution of the α_{SP} based on air masses that had passed over the area, Karoo region, Kalahari region, the anti-cyclonic recirculation pattern and the industrial hub classified according to the total, warmest/wettest, coldest and driest periods. The red line represents the median, the black dot the mean, the top and bottom edges of blue boxes the 25th and 75th percentiles and the black whiskers indicate 99.3 % coverage.

5.4 Chapter conclusion

From the auto-generated source maps, considering the entire measurement period, source areas and/or contribution sources affecting the aerosol optical properties at Welgegund were identified. Auto-generated source maps, considering defined periods, i.e. warmest/wettest, coldest and driest (also peak open biomass burning) gave a better quantification of contributions from sources and/or source areas. The quantification of aerosol optical properties was further improved by considering defined source regions, within the context of air mass histories.

Chapter 6

Contextualisation of aerosol optical properties measured at Welgegund

In this chapter, the mean aerosol optical properties measured at Welgegund for the entire measurement period, for different periods and defined source regions, are compared with mean and/or median optical properties measured at other sites.

6.1 Introduction

In Table 6-1, the mean aerosol optical properties, i.e. scattering coefficient (σ_{SP}), absorption coefficient (σ_{AP}), single scattering albedo (ω_0) and Ångström exponent (α_{SP}), for the entire measurement period, for the different periods (introduced in Chapter 5, section 5.2.2 (a) warmest/wettest, (b) coldest and (c) driest, peak biomass burning periods) and the defined regions (introduced in Chapter 5, section 5.3.3, (a) Karoo, (b) Kalahari, (c) anti-cyclonic recirculation pattern and (d) industrial hub), measured at Welgegund are presented. Some of these values are then compared with mean or median optical properties measured at other sites (including industrialised areas, arid regions, as well as urban and rural areas), which are presented in Table 6-2, to contextualise the Welgegund aerosol optical properties.

6.2 Contextualisation of σ_{SP}

6.2.1 Entire measurement period

The mean σ_{SP} measured at Welgegund for the entire measurement period was 23.8 M m^{-1}. This is comparable to the mean σ_{SP} (20.8 M m^{-1}) of coastal air masses reported for Mace Head, Ireland (Kleefeld *et al*., 2002). Although Welgegund is not a coastal site, this confirms that Welgegund receives air masses from the regional background. In contrast, the afore-mentioned Welgegund mean σ_{SP} is lower than the corresponding mean σ_{SP} (49.5 M m^{-1}) reported for Elandsfontein, South Africa, which is directly affected by nearby large point sources that mostly do not de-SO_x and de-NO_x their off-gas (e.g. coal-fired power stations, petrochemical operations and

metallurgical smelters) (Laakso *et al*., 2012; Collet *et al*., 2010). The emissions from the afore-mentioned source are so significant that the area wherein Elandsfontein lies is regarded as an NO_2 hotspot, as observed with satellite observations (Lourens *et al*., 2012; Collett *et al*., 2010). Additionally, the Welgegund mean σ_{SP} for the entire measurement period is significantly lower than values reported for highly polluted areas such as Xinken, Shangdianzi, Lin'an, Yulin and Beijing (all in China), which had σ_{SP} means between 158 and 488 M m^{-1} (Cheng *et al*., 2008; Yan *et al*., 2008; Xu *et al*., 2002; Xu *et al*., 2004; Bergin *et al*., 2001).

6.2.2 Different periods and source regions

During the warmest/wettest, coldest, as well as driest peak open biomass burning periods, the σ_{SP} means for air masses that had passed over the Karoo were 6.3, 9.7 and 10.1 M m^{-1}, respectively, which are comparable to σ_{SP} means reported for true background sites such as Barrow Alaska, USA (10.4 M m^{-1}) (Delene & Ogren, 2002), Pallas-Sodankylä, Finland (4.9 M m^{-1}) (Lihavainen *et al*., 2015) and Andøya Island, Norway (5.4 M m^{-1}) (Montilla *et al*., 2011). The highest σ_{SP} mean for all defined source areas over all the investigated time periods was observed in air masses that had passed over the industrial hub during the coldest period, which had a mean of 53.6 M m^{-1}. This compares to the σ_{SP} mean reported for Elandsfontein (South Africa) (49.5 M m^{-1}), but it is significantly lower than σ_{SP} means reported for polluted sites in China (ranging between 158 and 488 Mm^{-1}) (Cheng *et al*., 2008; Yan *et al*., 2008; Xu *et al*., 2002; Xu *et al*., 2004; Bergin *et al*., 2001).

6.3 Contextualisation of σ_{AP}

6.3.1 Entire measurement period

The mean σ_{AP} measured at Welgegund for the entire measurement period was 2.4 M m^{-1} and is comparable to the mean σ_{AP} (2.47 M m^{-1}) reported for Lamont, Oklahoma, USA (Delene & Ogren, 2002). This site is situated distant from large point sources, but is occasionally impacted by plumes from industry (Delene & Ogren, 2002). As for σ_{SP}, this similarly also confirms that Welgegund is a regional background site that is not directly impacted by large point sources. Similar to σ_{SP}, the mean σ_{AP} reported for Welgegund for the entire measurement period was lower than the corresponding mean σ_{AP} (8.3 M m^{-1}) reported for Elandsfontein, South

Africa (Laakso *et al*., 2012). The Welgegund mean σ_{AP} is also significantly lower than values reported for highly polluted areas such as Xinken, Shangdianzi, Lin'an and Beijing in China, which had σ_{AP} mean values between 17.5 and 83 M m^{-1} (Cheng *et al*., 2008; Yan *et al*., 2008; Xu *et al*., 2002, Bergin *et al*., 2001).

6.3.2 Different periods and source regions

The σ_{AP} means for all the defined source regions and during all the considered time periods were higher than σ_{AP} means reported for true background sites such as Barrow Alaska, USA (0.4 M m^{-1}) (Delene & Ogren, 2002), Pallas-Sodankylä, Finland (0.6 Mm^{-1}) (Lihavainen *et al*., 2015) and Andøya Island, Norway (0.4 M m^{-1}) (Montilla *et al*., 2011). The lowest σ_{AP} means observed were during the warmest/wettest period for air masses that had passed over the Karoo (1.0 M m^{-1}) and Kalahari (0.7 M m^{-1}). The highest σ_{AP} means observed were for the industrial hub during the coldest period (9.7 M m^{-1}), which were similar to the σ_{AP} mean reported for Elandsfontein, South Africa (8.3 M m^{-1}, Laakso *et al*., 2012), but substantially lower than σ_{AP} means reported for polluted sites in China (ranging between 17.5 and 83.0 M m^{-1}) (Cheng *et al*., 2008; Yan *et al*., 2008; Xu *et al*., 2002; Xu *et al*., 2004; Bergin *et al*., 2001).

6.4 Contextualisation of ω_0

6.4.1 Entire measurement period

The mean ω_0 for Welgegund over the entire period was 0.89. Elandsfontein, which is also located in the South African Highveld Grassland biome, is the only South African site for which *in situ* ground level ω_0 data have been reported. For this site, a mean ω_0 over a period of two years was reported as 0.84 (Laakso *et al*., 2012). As previously stated, Elandsfontein is relatively close to various large point sources; therefore, it will generally sample fresher industrial emissions than Welgegund, which will be affected more by aged air masses. Previous authors have proven that Welgegund is significantly affected by air masses that are recirculated anti-cyclonically, which include emissions from the area wherein Elandsfontein lies (Venter *et al*., 2016; Jaars *et al*., 2014). Therefore, although the mean ω_0 values for Welgegund and Elandsfontein are relatively similar, the factors affecting the ω_0 values at the two sites are different. The Welgegund mean ω_0 can further be

contextualised with mean and median ω_0 values from various sites in Table 6-2. However, since the climatological effect of ω_0 also dependents on the albedo of the underlying surface (e.g. Haywood & Boucher, 2000; Haywood & Shine, 1995), it is not that straightforward to directly compare the ω_0 of different sites. For example, for a typical 0.2 surface reflectance of grass, aerosols may heat the atmosphere if the ω_0 is less than 0.75 and *vice versa* for cooling (e.g. Betts & Ball, 1997). This implies that, in general, aerosols at Welgegund have a net cooling effect, which makes sense, considering it is a regional background site for which the aerosol composition is dominated by scattering species (Tiitta *et al*., 2014).

6.4.2 Different periods and source regions

Although the impact of ω_0 depends on the underlying surface albedo, some comparisons were made for the different periods and source regions. The ω_0 means of air masses that have passed over the Karoo were substantially lower than ω_0 means of air masses that had passed over the other defined regions during all the considered time periods. The ω_0 means observed for the Karoo (0.80 and 0.86) were lower (more absorbing) than true background sites such as Barrow Alaska, USA (0.96) (Delene & Ogren, 2002), Pallas-Sodankylä, Finland (0.90) (Lihavainen *et al*., 2015) and Andøya Island, Norway (0.91) (Montilla *et al*., 2011). ω_0 means for polluted sites in China have been reported to vary between 0.81 and 0.95 (Cheng *et al*., 2008; Yan *et al*., 2008; Xu *et al*., 2002; Xu *et al*., 2004; Bergin *et al*., 2001). The surface reflectance of the defined source regions will differ, with, for instance, the Karoo and Kalahari being much more sandy with less vegetation cover, than for instance the anti-cyclonic and industrial hub. However, it was beyond the scope of work to investigate the reflectance of the surface types occurring in the defined source areas, and consequently it was not considered further.

6.5 Contextualisation of α_{SP}

6.5.1 Entire measurement period

The mean α_{SP} measured at Welgegund for the entire measurement period was 1.52, which is comparable to previous mean and median α_{SP} values reported for Elandsfontein (1.5) in the NO_2 hotspot (Laakso *et al*., 2012) and Skukuza (1.4) in the Kruger National Park (Queface *et al*., 2011), both in South Africa. The Welgegund

mean α_{SP} was, however, significantly higher than sites that are directly impacted mainly by wind-blown dust, e.g. Cape Verde (0.36) and Saudi Arabia (0.41) (Dubovik *et al*., 2001). However, the Welgegund value was lower than sites that are directly impacted by anthropogenic activities such as Paris, France (1.8) and Mexico City, Mexico (1.8) (Dubovik *et al*., 2001).

6.5.2 Different periods and source regions

During all the considered time periods, the α_{SP} means for air masses that had passed over the Karoo (0.9 and 1.2) were equal and lower (larger particles) than α_{SP} means reported for true background sites such as Barrow Alaska, USA (1.2) (Delene and Ogren, 2002), Pallas-Sodankylä, Finland (1.7) (Lihavainen *et al*., 2015) and Andøya Island, Norway (1.4) (Montilla *et al*., 2011), and higher than α_{SP} means reported for sites that are directly impacted mainly by wind-blown dust, e.g. Cape Verde (0.36) and Solar village, Saudi Arabia (0.41) (Dubovik *et al*., 2001). The highest α_{SP} mean was observed for air masses that had passed over the anti-cyclonic recirculation pattern (1.68) during the warmest/wettest period, which was lower than α_{SP} means reported for sites that are directly impacted by anthropogenic activities (smaller particles) such as Bondville, Illinois, USA (2.0) (Delene & Ogren, 2002), Paris, France (1.8) and Mexico City, Mexico (1.8) (Dubovik *et al*., 2001).

Table 6-1: The mean aerosol optical properties measured at Welgegund for the entire measurement period and for the different periods (warmest/wettest, coldest and, driest, peak open biomass burning) over the defined source regions (Karoo, Kalahari, anti-cyclonic recirculation pattern, industrial hub)

Welgegund					
Different periods	**Defined region**	**σ_{SP} (M m^{-1})**	**σ_{AP} (M m^{-1})**	**ω_0**	**α_{SP}**
Entire measurement period	All regions	23.77	2.36	0.89	1.52
Warmest/wettest	Karoo	6.27	1.01	0.86	1.20
	Kalahari	8.25	0.66	0.91	1.64
	Anti-cyclonic recirculation pattern	20.90	1.22	0.94	1.68
	Industrial hub	22.47	2.25	0.91	1.54
Coldest	Karoo	9.72	2.25	0.80	1.08
	Kalahari	20.10	2.18	0.91	1.35
	Anti-cyclonic recirculation pattern	36.74	4.67	0.89	1.50
	Industrial hub	53.56	9.69	0.86	1.53
Peak, driest open biomass burning	Karoo	10.12	1.84	0.84	0.91
	Kalahari	34.49	6.62	0.85	1.12
	Anti-cyclonic recirculation pattern	50.76	7.9	0.87	1.39
	Industrial hub	39.81	4.14	0.90	1.28

Table 6-2: The mean and median aerosol optical properties measured at other international sites; only the Skukuza (SA) and Mongu (Zambia) (Queface et al., 2011) values were reported as medians

Other sites									
Sites	**σ_{SP} (M m^{-1})**	**σ_{AP} (M m^{-1})**	**ω_0**	**α_{SP}**	**Sites**	**σ_{SP} (M m^{-1})**	**σ_{AP} (M m^{-1})**	**ω_0**	**α_{SP}**
Bondville, Illinois (USA) (Delene & Ogren, 2002)	57.00	4.62	4.62	2.03	Yulin (China) (Xu *et al*., 2004)	158.00	6.00	0.95	
Sable Island, Nova Scotia (Canada) (Delene & Ogren, 2002)	40.70	1.89	1.89	0.83	Beijing (China) (Bergin *et al*., 2001)	488.00	83	0.81	
Barrow, Alaska (Canada) (Delene & Ogren, 2002)	10.40	0.38	0.38	1.20	Goddard Space Flight Center Greenbelt (USA) (Dubovik *et al*., 2001)			0.97	1.90
Lamont, Oklahoma (USA) (Delene and Ogren, 2002)	46.7	2.47	2.47	1.90	Paris (France) (Dubovik *et al*., 2001)			0.93	1.80
Pallas-Sodankylä, (Finland) (Aaltonen *et al*., 2006)	4.60			1.80	Mexico City (Mexico) (Dubovik *et al*., 2001)			0.88	1.80
Pallas-Sodankylä, (Finland) (Lihavainen *et al*., 2015)	4.90	0.57	0.57	1.70	Maldives (Dubovik *et al*., 2001)			0.89	1.55
Elandsfontein (SA) (Laakso *et al*., 2012)	49.50	8.30	8.30	1.50	Amazonian forest Brazil and Bolivia (Dubovik *et al*., 2001)			0.93	1.95
Mace head (Ireland) (Kleefeld *et al*., 2002)	20.80				Cerrado Brazil (Dubovik *et al*., 2001)			0.89	1.85
Cape grim, (Tasmania) (Carrico *et al*., 1998)	15.40				Zambia (Dubovik *et al*., 2001)			0.84	1.95

Table 6-2: continue; The mean and median aerosol optical properties measured at other international sites; only the Skukuza (SA) and Mongu (Zambia) (Queface *et al*., 2011) values were reported as medians

International sites									
Sites	**σ_{SP} (M m^{-1})**	**σ_{AP} (M m^{-1})**	**ω_0**	**α_{SP}**	**Sites**	**σ_{SP} (M m^{-1})**	**σ_{AP} (M m^{-1})**	**ω_0**	**α_{SP}**
Mace head (Ireland) (Marine) (Junker *et al*., 2006)		0.31	0.31		Canada (Dubovik *et al*., 2001)			0.94	1.96
Mace head (Ireland) (Continental) (Junker *et al*., 2006)		3.93	3.93		Bahrain/Persian Gulf (Dubovik *et al*., 2001)			0.95	1.10
AndØya Island, (Norway) (Montilla *et al*., 2011)	5.42	0.40	0.40	1.37	Solar-village (Saudi Arabia) (Dubovik *et al*., 2001)			0.96	0.41
Skukuza (SA) (Queface *et al*., 2011)				1.41	Cape Verde (Dubovik *et al*., 2001)			0.98	0.36
Mongu (Zambia) (Queface *et al*., 2011)				1.73	Lanai (Hawaii) (Dubovik *et al*., 2001)			0.97	1.40
Xianghe (China) (Li *et al*., 2008)					Alta Floresta Brazil (Reid *et al*., 1999)			0.86	0.97
Xinken (China) (Cheng *et al*., 2008)	333.00	61.00	61.00	1.60	Cuiaba Brazil (Reid *et al*., 1999)			0.85	1.08
Shangdianzi (China) (Yan *et al*., 2008)	174.60	17.54	0.88		Ji Parana Brazil (Reid *et al*., 1999)			0.87	0.82
Lin'an (China) (Xu *et al*., 2002)	353.00	23.00	0.93						

6.6 Chapter conclusion

The σ_{SP} and σ_{AP}, which combined determine the ω_0, measured in air masses that had passed over the Karoo were similar to values measured at true background sites. These coefficients were highest in air masses that had passed over the industrial hub, or the anti-cyclonic recirculation pattern. However, these reported values were significantly lower than values reported for highly polluted areas. The mean ω_0 for Welgegund over the entire measurement period was comparable to the mean ω_0 reported for Elandsfontein, located in the Mpumalanga Highveld, South Africa. However, the factors affecting the ω_0 values at the two sites were different. It was also not that straightforward to contextualise the Welgegund ω_0 values with other sites, since the climatological effect of ω_0 depends on the albedo of the underlying surface. During all the considered time periods, the α_{SP} means for air masses that had passed over the Karoo were equal, or lower (larger particles) than α_{SP} means reported for true background sites, and higher than means reported for sites that are mainly impacted by wind-blown dust. The highest α_{SP} mean was observed in air masses that had passed over the anti-cyclonic recirculation pattern during the warmest/wettest period, which was lower than α_{SP} means reported for sites that are directly impacted by anthropogenic activities.

Chapter 7

Mathematical confirmation of factors and sources contributing to aerosol optical properties

In section 7.1, it was proven that conventional 1:1 correlation of parameters cannot be used to explain the optical parameter observations. Thereafter, a statistical approach was used to consider more parameters in an attempt to explain the observed aerosol optical property results better (section 7.2), and to independently verify deductions made in Chapters 4 and 5.

7.1 Conventional correlation of parameters

Conventional 1:1 correlation of parameters (e.g. y *vs*. x graphs) does not always lead to a better understanding, or explanation of results. An example can be illustrated by considering Figure 7-1, presenting the Moderate Resolution Imaging Spectroradiometer (MODIS) fire pixels observed within 100 and 250 km radii around Welgegund. From this data, 2014 and 2016 can be identified as the years with the highest and lowest average open biomass burning frequencies, respectively.

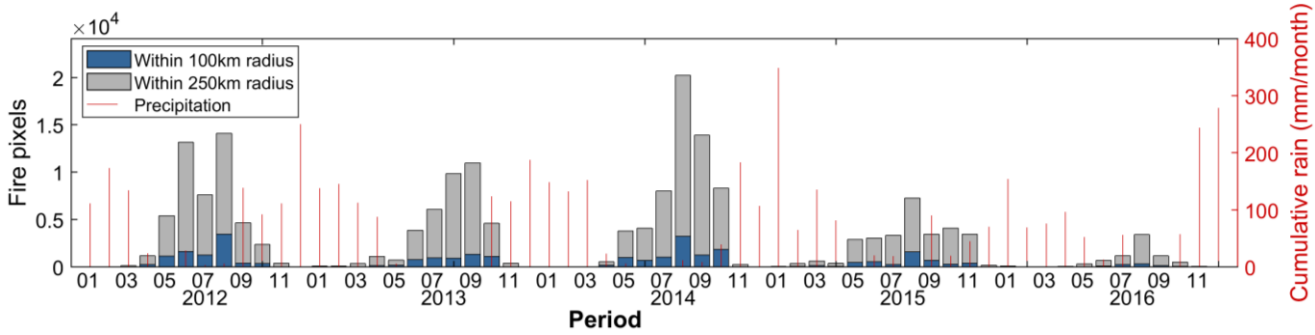

Figure 7-1: Fire burnt scar pixel counts within 100 and 250 km radii around Welgegund, determined with MODIS collection 5 burned area product (Roy *et al*., 2008), and monthly cumulative rain measured at Welgegund, for the entire measurement period

Figure 7-2 presents the scattering coefficient (σ_{SP}) for (a) 2014 and (b) 2016, as well as the absorption coefficient (σ_{AP}) for (c) 2014 and (d) 2016, respectively. If the σ_{SP} and σ_{AP} values measured during the driest, peak open biomass burning period (August to mid-October) during 2014 and 2016 depended only on open biomass burning frequencies, a significant difference in median values, i.e. σ_{SP} (average 33.86 and 36.03 M m^{-1} for 2014 and 2016, respectively) and σ_{AP} (average 5.16 and 3.81 M m^{-1} for 2014 and 2016, respectively), would have been observed. However, this was not the case, which proves that σ_{SP} and σ_{AP} are not only dependent on a single factor/parameter (such as open biomass burning frequency). Similarly, multiple factors/parameters influence the other aerosol optical properties, i.e. single scattering albedo (ω_0) and Ångström exponent (α_{SP}).

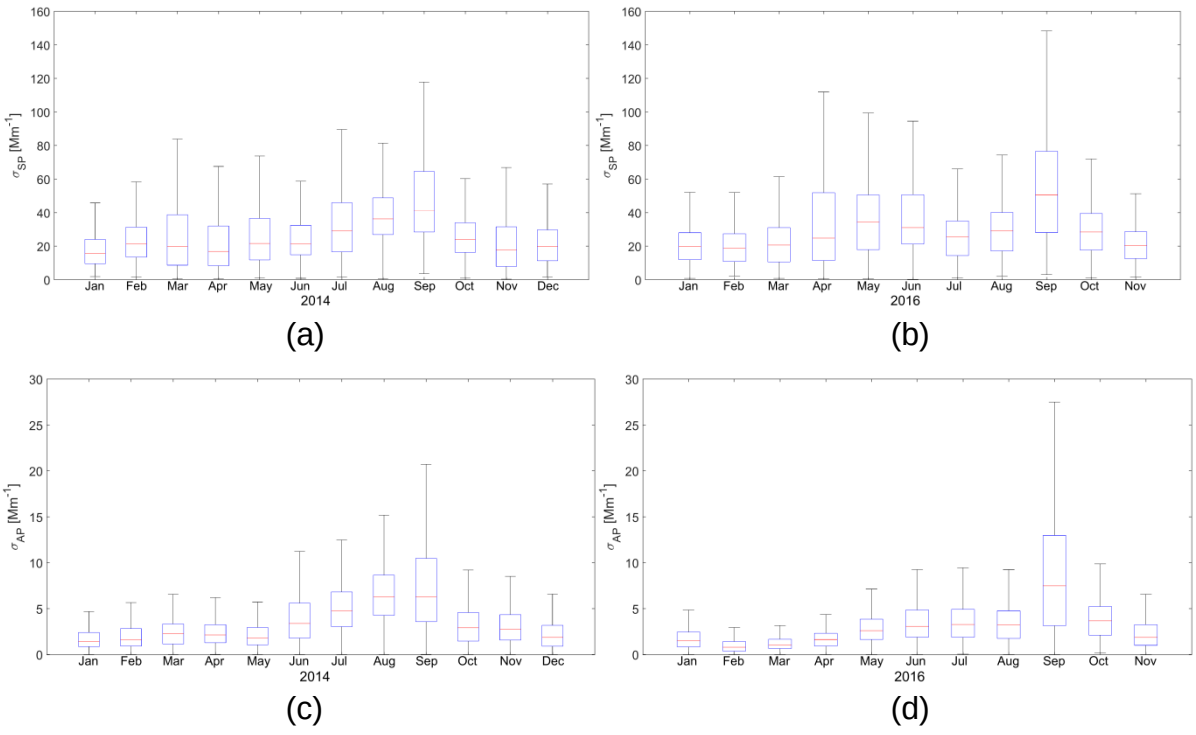

Figure 7-2: Monthly statistical distribution of σ_{SP} for (a) 2014 and (b) 2016 and σ_{AP} for (c) 2014 and (d) 2016 measured at Welgegund. The red lines represent the median, the top and bottom edges of blue boxes the 25th and 75th percentiles and the black whiskers indicate 99.3 % coverage.

Therefore, to explain the observed aerosol optical results better, more parameters should be considered, e.g. precipitation, relative humidity (RH), temperature (T),

wind speed and direction, pollutant levels. Consequently, the candidate decided to use a statistical method, i.e. multiple-linear regression (MLR), which combines all the available parameters, measured at Welgegund, to explain the aerosol optical results/observations better. A statistical approach such as MLR analysis is not without flaws, but it can serve as an additional independent analysis of the results, which is not guided by preconceptions of the candidate.

7.2 MLR

Within the context of this thesis, each aerosol optical property (σ_{SP}, σ_{AP}, ω_0, or α_{SP}) was considered separately as a dependent parameter in an MLR calculation, and all other non-optical parameters measured at Welgegund (precipitation, RH, T, wind speed and direction, pollutant levels, etc.) considered as independent parameters. Figures 7-3a, b, c and d present the root mean square error (RMSE) differences of the σ_{SP}, σ_{AP}, ω_0, and α_{SP}, respectively, between the calculated and measured values as a function of the number of independent variables included in the optimum MLR solution. It is evident from Figure 7-3 that the RMSE for σ_{SP}, σ_{AP}, ω_0, and α_{SP} was ~13, 2.12, 0.071 and 0.396, respectively, if only one independent variable was included in the optimum MLR solution. If more independent variables were included in the optimum MLR solution, the RMSE reduced. Negligible improvement in RMSE occurred after 8, 9, 7 and 9 independent parameters were included in the optimum MLR equation for σ_{SP}, σ_{AP}, ω_0, and α_{SP}, respectively.

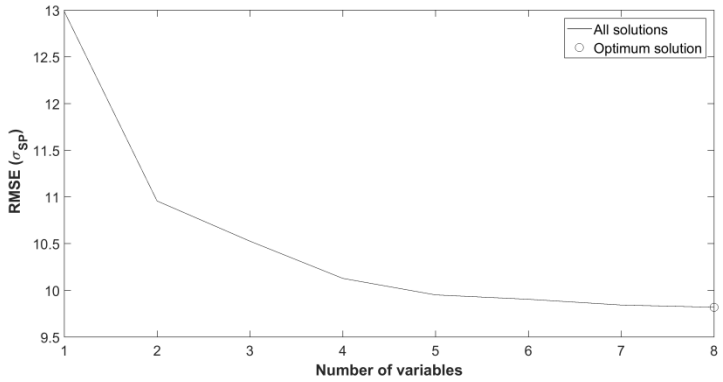

(a)

Figure 7-3: The RMSE difference between the calculated and actual optical properties (a) σ_{SP}, (b) σ_{AP}, (c) ω_0, and (d) α_{SP} values measured at Welgegund for the entire measurement period

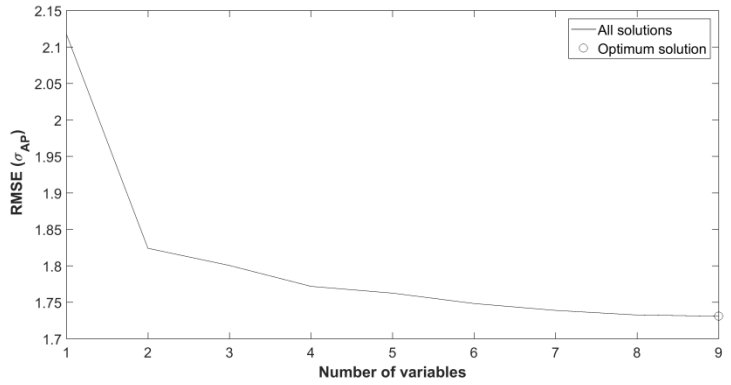

(b)

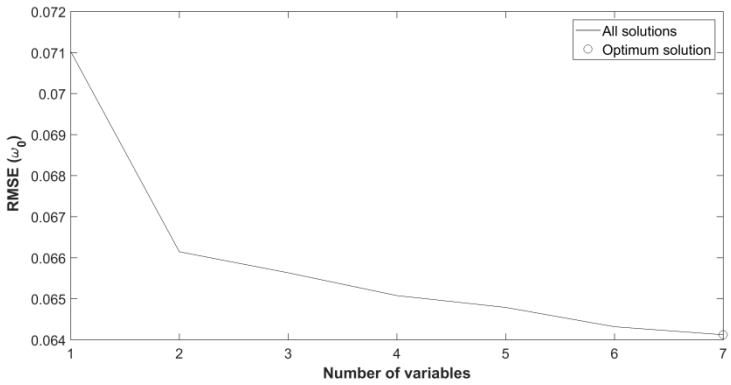

(c)

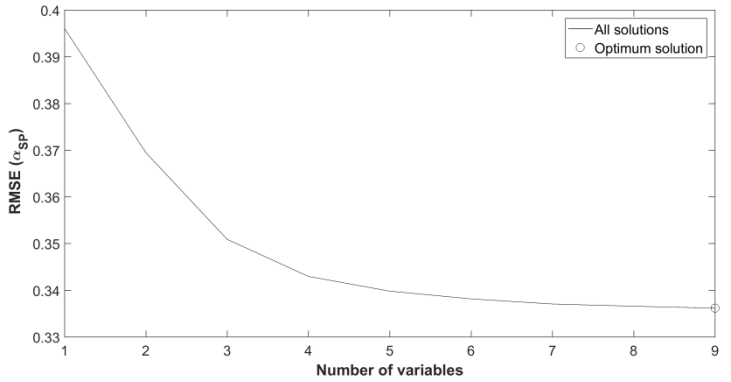

(d)

Figure 7-3: continue; The RMSE difference between the calculated and actual optical properties (a) σ_{SP}, (b) σ_{AP}, (c) ω_0, and (d) α_{SP} values measured at Welgegund for the entire measurement period

Essentially, it is the combination of parameters, and not individual parameters, in the optimum MLR equation that enables a relatively accurate calculation of the aerosol optical properties. Furthermore, the independent parameters considered in the MLR calculation were limited to the species/parameters measured at Welgegund, and these independent parameters might not be representative of contributing sources

and/or meteorological parameters influencing the aerosol optical properties. Notwithstanding these limitations, the independent statistical evaluation conducted with MLR confirmed the earlier deductions with regard to contributing sources and/or meteorological patterns (Chapters 4 and 5), as indicated in the subsequent sections.

7.2.1 σ_{SP}

The optimum MLR equation obtained from the MLR analysis for σ_{SP} is presented in Eq. 7.1. Comparison between the actual and calculated (using Eq. 7.1) σ_{SP} values over the entire measurement period is presented in Figure 7-4.

$$\sigma_{SP} = -32.601 + (2.952E\text{-}1 \times O_3 \text{ ppb}) + (5.033E\text{-}1 \times SO_2 \text{ ppb}) + (1.28548 \times NO_2 \text{ ppb}) - (2.142 \times NO \text{ ppb}) + (1.462E\text{-}1 \times CO \text{ ppb}) + (0.148 \times T\ °C) + (2.395E\text{-}1 \times \%RH) + (5.315E\text{-}1 \times PM_{10}\ \mu g\ m^{-3}) \quad (7.1)$$

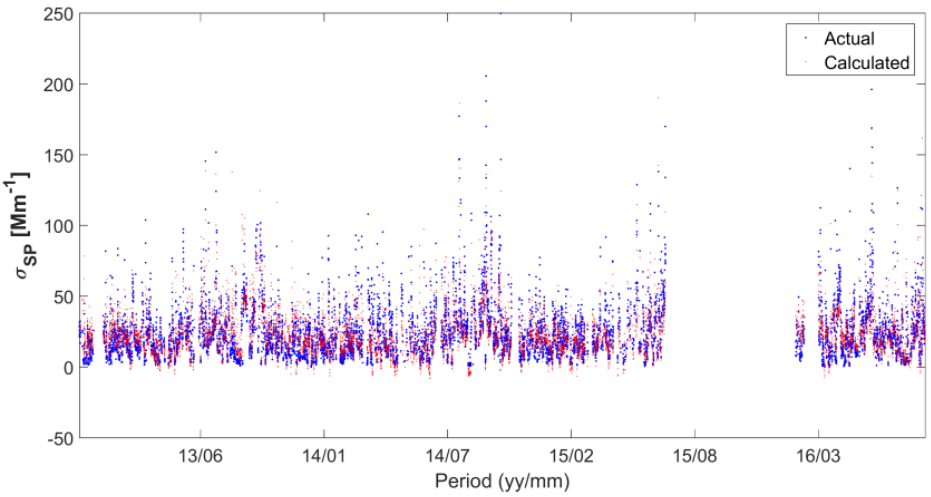

Figure 7-4: Comparison between the actual (blue) and calculated (red) σ_{SP} values, using Eq. 7.1, over the entire measurement period

From Figure 7-4, it is evident that the optimum MLR equation can be used to relatively accurately calculate σ_{SP} at Welgegund. However, instead of proposing that Eq. 7.1 be used to calculate σ_{SP}, it was more important to assess whether the optimum MLR equation, which was calculated without input or bias from the candidate, supported the source deductions made in Chapters 4 and 5. As is evident from Eq. 7.1, increased ozone (O_3) concentrations (indicated by the positive sign) lead to higher σ_{SP} values, indicating that aged air masses and/or more oxidising conditions result in more reflective aerosols, which was proposed in sections 4.3.1,

4.4.2, 5.2.1.2, 5.2.2.1, 5.3.1.2, 5.3.2 and 5.3.3. Air masses with higher (positive sign) sulphur dioxide (SO_2) and nitrogen dioxide (NO_2) concentrations also led to higher σ_{SP}, supporting the earlier deductions (sections 4.3.1, 4.3.2, 4.4.2, 5.3.2.2) that sulphate (SO_4^{2-}) and nitrate (NO_3^-) formation from SO_2 and NO_2, respectively, contribute to higher σ_{SP}. Increased nitrogen monoxide (NO) concentrations that would typically be associated with freshly emitted plumes decrease (negative sign) σ_{SP}, which correlates with the earlier deduction that higher σ_{SP} is rather associated with aged air masses. Increased carbon monoxide (CO) concentrations (positive sign) could also indicate the detection of fresher open biomass burning plumes (e.g. Venter *et al*., 2012). However, at a regional background site such as Welgegund, increased regional open biomass burning is indicated by increased CO concentrations (Laakso *et al*., 2008). Therefore, the positive sign associated with CO in Eq. 7.1 supports the earlier deduction that regional (aged) open biomass burning leads to higher σ_{SP} (sections 5.2.1.1, 5.2.2.1, 5.3.1.1). Higher T and RH (positive signs) also led to higher σ_{SP}, which supports the notion that increased oxidation of especially SO_2 to sulphate (SO_4^{2-}) in the warmer/wettest months leads to more scattering aerosols (sections 4.1, 4.3.2, 4.4.2, 5.3.1.2). Higher T (positive sign) is in general also associated with higher O_3 concentrations (Laban *et al*., 2018), which yet again supports the suggestion that the scattering of aerosols is higher in aged air masses and/or in more oxidising conditions (sections 4.3.1, 4.4.2, 5.2.1.2, 5.2.2.1, 5.3.1.2, 5.3.2, 5.3.3), which also correlated with higher σ_{SP} values observed in the warmer months, with lower σ_{SP} values in the colder months. Lastly, particulate matter with an aerodynamic diameter less than 10 µm (PM_{10}) concentrations (positive sign) correlates with an increase in σ_{SP} values, which indicates the contribution of wind-blown dust (sections 4.3.1, 5.2.1.1, 5.2.2.1, 5.3.1.1) as well as open biomass burning (sections 4.3.1, 5.2.1.1, 5.2.2.1, 5.3.1.1, 5.3.3.1) and domestic combustion (4.3.1 and 5.3.3.1).

7.2.2 σ_{AP}

The optimum MLR equation obtained from the MLR analysis for σ_{AP} is presented in Eq. 7.2. Comparison between the actual and calculated (using Eq. 7.2) σ_{AP} values over the entire measurement period is presented in Figure 7-5.

$$\sigma_{AP} = -1.0542 + (2.960E\text{-}2 \times O_3 \text{ ppb}) + (3.564E\text{-}2 \times CO \text{ ppb}) - (1.093E\text{-}1 \times NO \text{ ppb}) + (2.426E\text{-}1 \times NO_2 \text{ ppb}) + (6.472E\text{-}2 \times PM_{10} \text{ µg m}^{-3}) - (7.756E\text{-}2 \times SO_2 \text{ ppb}) - (9.193E\text{-}2 \times T \text{ °C}) - (1.590E\text{-}2 \times \%RH) - (1.9516 \times \text{T-gradient K m}^{-1}) \quad (7.2)$$

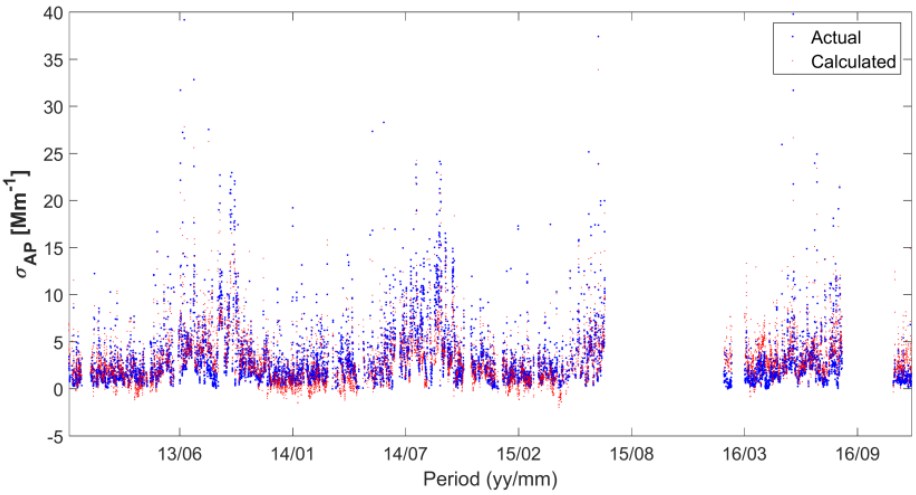

Figure 7-5: Comparison between the actual (blue) and calculated (red) σ_{AP} values, using Eq. 7.2, over the entire measurement period

Figure 7-5 indicates that the optimum Eq. 7.2 can be used to relatively accurately calculate σ_{AP} at Welgegund. From Eq. 7.2, it is evident that an increase in O_3 concentrations led to an increase (positive sign) in σ_{AP} values. O_3 concentrations are mostly associated with aged air masses and reflective aerosols (higher σ_{SP}). However, regional open biomass burning emissions result in both reflective (e.g. organic aerosols, OA) and absorptive (black carbon, BC) species (sections 4.3.1, 5.2.1.1, 5.2.2.1, 5.2.2.2). In the South African interior, the annual peaks of CO and O_3 concentrations coincide, which correlates with the peak open biomass burning period. Therefore, the positive sign associated with O_3 and CO concentrations could indicate the contribution of open biomass burning. Typically, increased NO concentrations indicate fresher plumes that are especially relevant to nearby open biomass burning. As indicated by Vakkari *et al*. (2018, 2014), fresher open biomass burning plumes are measured at Welgegund occasionally, but in general, aged biomass burning have a much larger fractional contribution to the aerosol chemistry at Welgegund (Tiitta *et al*., 2014). Therefore, the negative sign associated with NO concentrations could indicate more absorptive species (e.g. BC) that are measured in aged biomass burning plumes at Welgegund (sections 4.3.2, 5.3.1.2, 5.3.3.2).

This also correlates with the positive sign associated with NO_2 concentrations. For the $\sigma_{SP,}$ the positive sign for PM_{10} concentrations can possibly be associated with wind-blown dust. However, for the σ_{AP}, increased (positive sign) PM_{10} concentrations could indicate the contribution from regional open biomass burning, which led to higher σ_{AP} values (sections 5.2.1.1, 5.2.2.2, 5.3.1.1). Peak PM_{10} concentrations measured at Welgegund correlate with the peak biomass burning period (Cogho *et al*., 2019 – in preparation). The negative sign associated with SO_2 concentrations indicates that absorbing aerosols are mixed with scattering aerosols, which can alter the optical properties of absorbing aerosols; i.e., SO_4^{2-} and volatile organic compounds (VOCs) can deposit as a coating on BC particles, thereby resulting in lower σ_{AP} values. Higher T and RH also led to decreased (negative sign) σ_{AP} due to less open biomass burning during the warmest/wettest period, which supports the deductions from sections 4.3.1, 5.2.2.2, 5.3.1.1, 5.3.3.1. Higher T-gradients, as typically observed in unstable summer conditions, led to lower σ_{AP} values, which supports the T and RH deductions.

7.2.3 ω_0

Eq. 7.3 presents the optimum MLR equation obtained from the MLR analysis for ω_0. The comparison between the actual and calculated (using Eq. 7.3) ω_0 values over the entire measurement period is presented in Figure 7-6.

$$\omega_0 = 6.788E\text{-}1 + (1.142E\text{-}3 \times O_3 \text{ ppb}) + (2.233E\text{-}3 \times SO_2 \text{ ppb}) - (2.748E\text{-}4 \times CO \text{ ppb}) + (5.170E\text{-}3 \times T\ ^\circ C) + (1.655E\text{-}3 \times \%RH) - (1.888E\text{-}3 \times \text{Wind speed m s}^{-1}) + (6.871E\text{-}4 \times PM_{10}\ \mu g\ m^{-3}) \quad (7.3)$$

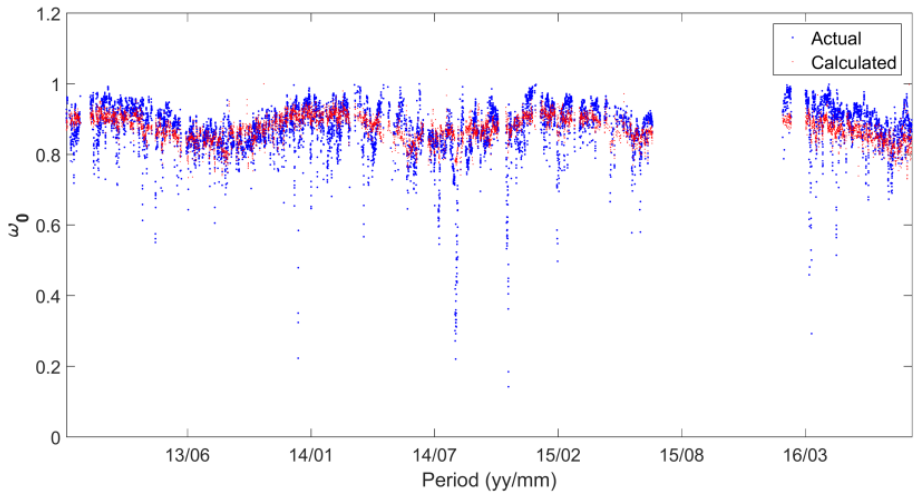

Figure 7-6: Comparison between the actual (blue) and calculated (red) ω_0 values, using Eq. 7.3, over the entire measurement period

The ω_0 is the combined effect of the σ_{SP} and σ_{AP}, as stated on multiple occasions in Chapters 4 and 5 (sections 4.4.2, 5.2.2.3). Therefore, it can be quite challenging to interpret the ω_0 in isolation. Since σ_{SP} and σ_{AP} were already considered within the context of MLR calculations, the candidate did not attempt to explain the meaning of each parameter included in the optimum equation for ω_0. However, it is evident that six out of the seven parameters included in optimum MLR equation correlated in identification and sign of the optimum MLR equation for σ_{SP}. This indicates and supports the findings that ω_0 is in general more scattering than absorbing (sections 6.2, 6.3).

7.2.4 α_{SP}

The optimum MLR equation obtained from the MLR analysis for α_{SP} is presented in Eq. 7.4. Figure 7-7 presents the comparison between the actual and calculated (using Eq. 7.4) α_{SP} values over the entire measurement period.

$$\alpha_{SP} = 6.315E\text{-}2 + (1.834E\text{-}2 \times O_3 \text{ ppb}) + (7.421E\text{-}3 \times SO_2 \text{ ppb}) + (1.896E\text{-}2 \times NO_2 \text{ ppb}) - (3.537E\text{-}2 \times NO \text{ ppb}) - (4.976E\text{-}3 \times PM_{10} \text{ µg m}^{-3}) - (1.643E\text{-}2 \times \text{Wind speed m s}^{-1}) + (2.457E\text{-}2 \times T \text{ °C}) + (8.9757E\text{-}3 \times \%RH) - (3.987E\text{-}1 \times \text{T-gradient K m}^{-1}) \quad (7.4)$$

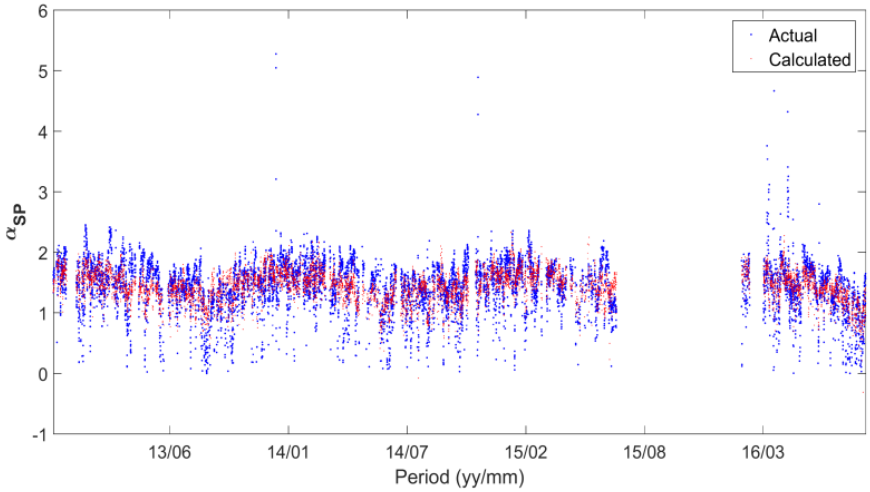

Figure 7-7: Comparison between the actual (blue) and calculated (red) α_{SP} values, using Eq. 7.4, over the entire measurement period

Figure 7-7 indicates that the optimum Eq. 7.4 can be used to relatively accurately calculate α_{SP} at Welgegund. As is evident from Eq. (7.4), increased O_3 concentrations (positive sign) led to increased α_{SP} values, indicating that aged air masses and/or more oxidising conditions contain secondary formed particles, which have smaller diameters (sections 4.3.3, 5.2.2.4, 5.3.1.3, 5.3.3.3). Similar to O_3, air masses with higher (positive sign) SO_2 and NO_2 concentrations result in higher α_{SP} values, also indicating that SO_4^{2-} and NO^- are secondary formed from SO_2 and NO_2, respectively. As indicated earlier, higher NO concentrations indicate fresher open biomass burning plumes. Therefore, fresher open biomass burning plumes led to lower α_{SP} values (indicated by the negative sign), which correlated with larger particles. Higher PM_{10} concentrations correlated with lower (negative sign) α_{SP} values (larger particles), which indicated the contribution of wind-blown dust, proposed in sections 4.3.3, 5.2.2.4, 5.3.1.3, 5.3.3.3. The contribution of wind-blown dust can also be observed in the negative sign associated with wind speed, where an increase in wind speed leads to lower α_{SP} values. An increased T-gradient, associated with more unstable conditions, usually observed during the warmer/wettest months, leads to lower (negative sign) α_{SP} values, which also supports the wind speed deductions. Higher T and RH (positive signs) led to higher α_{SP} values, supporting the earlier deductions made from sections 4.3.3, 5.2.2.4, 5.3.3.3, which indicated that smaller particles are secondary formed, e.g. SO_4^{2-}, during the warmest/wettest months.

7.3 Chapter conclusion

Instead of using the optimum MLR equations to calculate optical parameters, it was used to support the source deductions made in Chapters 4 and 5. Although the interpretations of the meaning of parameters included in the optimum MLR equations, and the signs (positive or negative) associated with them, were somewhat speculative, it did indicate that the source deductions made in Chapters 4 and 5 were plausible.

Chapter 8

Main findings and conclusions, project evaluation and future perspectives

In this chapter, the main findings and conclusions are presented, followed by an evaluation of the successes and/or shortcomings of the project by considering each of the objectives listed in Chapter 1. This highlights the outcome of the study and contributes to a better understanding of aerosol optical properties in South Africa. The future perspectives are also presented in this chapter, focusing on the possible key areas that need to be addressed.

8.1 Main findings and conclusions

For this thesis, long continuous (approximately 6 years), *in situ*, ground-level scattering and absorption measurements over the South African interior were reported from September 2011 to November 2016. The results (Chapters 4 to 7) presented the temporal patterns of aerosol optical properties, investigated the contribution of possible sources, source areas and meteorological effects on aerosol optical properties, contextualised the mean aerosol optical properties with other sites, and confirmed deductions with regard to possible sources by using a statistical approach.

In Chapter 4, it was indicated that the aerosol optical properties (scattering coefficient, σ_{SP}, absorption coefficient, σ_{AP}, single scattering albedo, ω_0, and Ångström exponent, α_{SP}) had relatively well-defined seasonal and diurnal patterns that indicated the influence of fire frequencies, possible sources (e.g. industrial emissions, domestic combustion, wind-blown dust) and meteorological effects (e.g. temperature, relative humidity (RH), and especially the planetary boundary layer (PBL) daily evolution and air mass circulation patterns). The seasonal patterns indicated more absorbing aerosols during the annual driest and coldest periods, which although not definitive, could be due to increased domestic combustion for

space heating and open biomass burning. More scattering aerosols were observed during the annual warmest/wettest period. The α_{SP} seasonality indicated larger particles during the coldest and driest period, which were associated with wind-blown dust. Considering the diurnal pattern for the $\omega_{0,}$ it was deduced that ozone (O_3) formation during the daytime, as well as downward mixing of industrial high-stack emissions after the break-up of low level inversion layers, contributes to the formation of mostly scattering secondary aerosols, which led to increased ω_0 during daytime. In addition, increasing mixing heights during daytime dilutes low-level emitted black carbon (BC) (absorbing aerosols). Although some source deductions could be made from the temporal patterns, it was mostly indicative.

In Chapter 5, two main approaches, i.e. auto-generated source maps (section 5.2) and defined source regions (section 5.3), were used to identify more unambiguous sources and source areas that influenced the aerosol optical properties. From these two approaches, the contributions of seasonal sources (e.g. open biomass burning, domestic combustion for space heating, wind-blown dust) and continuous emission sources (e.g. industrial emissions and domestic combustion for cooking) were observed. From the auto-generated source maps (section 5.2), considering all aerosol optical properties for the entire measurement period, anthropogenic activities such as emissions from the Vaal Triangle, Mpumalanga Highveld and Johannesburg-Pretoria megacity, as well as the aging and recirculation of pollution over the dominant anti-cyclonic recirculation pattern, in addition to high open biomass burning frequencies (especially over eastern Zimbabwe and central Mozambique) had the most significant effects on the aerosol optical properties, if compared to the background sector between west-southwest and south-southwest of Welgegund. The auto-generated source maps for defined periods, i.e. warmest/wettest, coldest and driest, peak open biomass burning, indicated the contributions from sources and/or source areas even better. From the warmest/wettest period for all aerosol optical properties, the contribution of air masses that had passed over industrial activities and the dominant anti-cyclonic recirculation pattern were evident. The coldest period mostly indicated the contribution of higher population densities (more domestic combustion for space heating) in addition to industrial activities that contribute year-round. Additionally,

evidence of possible transport of aerosols from the Western Cape was observed in the auto-generated source maps for the σ_{AP} and α_{SP} during the coldest period. From the driest period, the contributions of open biomass burning frequencies of air masses that had passed over eastern Zimbabwe and central Mozambique were evident for all aerosol optical properties.

The defined source region approach (section 5.3) was subdivided into three different methods that further improved the understanding of possible sources and source regions influencing aerosol optical properties. The predefined eastern and western sector method (section 5.3.1) allowed the comparison of aerosol optical properties for air masses that had passed over the eastern (higher industry population densities and open biomass burning frequencies), and western (very few industries, lower population densities and lower open biomass burning frequencies) sectors during the warmest/wettest and driest periods. From this comparison, the significant differences between the two defined sectors and contributions of open biomass burning to all aerosol optical properties during the driest period were evident. The predefined source- and proximity-based source regions approach (section 5.3.2) allowed the comparison of aerosol optical properties for air masses that had passed over the anthropogenic source regions in the eastern sector. From this approach, it was evident that the aerosol optical properties were significantly altered (if compared to the regional background) in air masses that had passed over the anthropogenic influenced source regions in the South African interior. For example, the σ_{SP} and α_{SP} indicated the extent of pollution of air masses that had passed over the Vaal Triangle (VaalT), as well as the occurrence of wind-blown dust that travelled over the VaalT from the eastern Free State to Welgegund. In the last method (section 5.3.3), information obtained by the predefined and auto-generated source maps region methods was applied, which allowed the comparison between two separate background regions, i.e. Karoo and Kalahari, and two anthropogenically influenced regions, i.e. anti-cyclonic recirculation pattern and the industrial hub, during different periods, i.e. warmest/wettest, coldest and driest periods. From these aerosol optical property results, it was evident that air masses that had passed over the Karoo were typically cleaner (e.g. lower σ_{SP} and σ_{AP}) than air masses that had passed over the

Kalahari and that air masses that had passed over the industrial hub during the coldest period were the most polluted (e.g. highest σ_{SP} and σ_{AP}).

In Chapter 6, the mean aerosol optical properties measured at Welgegund for the entire measurement period, for different periods (warmest/wettest, coldest and peak, driest open biomass burning) and defined source regions (Karoo, Kalahari, anti-cyclonic recirculation pattern and industrial hub) were compared with mean and/or median optical properties measured at other sites. The highest mean aerosol optical property values during all periods were lower than the mean values reported for polluted sites. The mean aerosol optical property values measured in air masses that had passed over the Karoo region during all periods were similar and/or higher to mean values reported for true background sites. The mean ω_0 for Welgegund over the entire measurement period was comparable with the mean ω_0 reported for Elandsfontein. However, it was not that straightforward to contextualise the Welgegund ω_0 values with other sites, since the climatological effect of ω_0 depends on the albedo of the underlying surface.

Lastly, in Chapter 7, a statistical approach, i.e. multi-linear regression (MLR) analysis, was applied to serve as an additional, independent analysis to support the source deductions made in the earlier chapters. Although the interpretations of the meaning of parameters included in the optimum MLR equations, and the signs (positive or negative) associated with them, were somewhat speculative, it did indicate that the source deductions made in Chapter 4 to 6 were plausible.

8.2 Project evaluation

This thesis was evaluated by considering the objectives presented in Chapter 1, and secondly considering the overall project success.

Objective I: ***"Obtain a suitable long-term dataset measured in the South African interior, which can be used to evaluate the aerosol optical properties"***

The dataset used in this thesis was measured at Welgegund (section 3.1), which is situated approximately 100 km west of Johannesburg. The candidate was co-responsible for collecting this dataset. Welgegund can be considered as

representative of the regional background of the interior of South Africa, as there are no significant anthropogenic pollution sources nearby and most of the large point sources are situated in the sector between north to south-east from Welgegund. A long-term dataset of approximately six years (September 2011 to November 2016) was obtained.

Objective II: ***"Process the raw data to calculate scattering (σ_{SP}) and absorption (σ_{AP}) coefficients, single scattering albedo (ω_0) and Ångström exponent (α_{SP}) for the entire dataset"***

The raw high-resolution 1 min scattering and absorption data, measured with a three-wavelength nephelometer and multi-angle absorption photometer (MAAP), respectively (section 3.2), were processed to account for maintenance and calibrations, as well as power failures and recovery periods after power failures (section 3.3). Thereafter, the 1 min data were converted to 15 min averages. The α_{SP} was calculated for the entire wavelength range (450, 525, 635 nm), by fitting the logarithm of the σ_{SP} and the respective wavelengths to the proposed equation in section 3.4.1 The ω_0 was calculated by, firstly, using the α_{SP} to logarithmically interpolate the wavelength (635 nm) of the σ_{SP} to correlate with the wavelength of the σ_{AP} at 637 nm, and secondly, by using the σ_{SP} and σ_{AP} from the equation presented in section 3.4.1.

Objective III: ***"Determining temporal patterns, i.e. diurnal and seasonal, for all the aerosol optical properties and make general deductions with regard to contributing sources and/or factors influencing the aerosol optical properties"***

Clear seasonal cycles and diurnal patterns were observed for all the aerosol optical properties (σ_{SP}, σ_{AP}, ω_0 and α_{SP}) (sections 4.3 and 4.4) indicating the influence of meteorological conditions (e.g. temperature, relative humidity, planetary boundary layer, precipitation) and possible sources (e.g. industrial emissions, domestic combustion, open biomass burning, wind-blown dust). Some general source deductions could be made with regard to contributing factors and sources to explain the observed temporal patterns, but such deductions were not unambiguous.

Objective IV: "Use more advanced data analysis techniques to investigate possible sources and/or factors influencing the aerosol optical properties"

Two different approaches were explored in order to investigate possible sources and/or factors influencing the aerosol optical properties, i.e. auto-generated source (section 5.2) maps and defined source regions (section 5.3). These methods showed that air masses that had passed over certain source areas and/or during periods were significantly different (in terms of optical properties) than air masses that had passed over the regional background. Furthermore, it was proven that the Karoo is likely the cleanest (in terms of aerosol optical properties) regional background.

Objective V: "Contextualise the aerosol optical properties (overall, seasonal and for specific source regions) within local and international perspectives"

In Chapter 6, the mean aerosol optical properties for the entire sampling period, for different periods (i.e. warmest/wettest, coldest and driest, peak open biomass burning period) and defined source regions (i.e. Karoo, Kalahari, anti-cyclonic recirculation pattern and industrial hub) were contextualised with mean/median aerosol optical properties from 34 different local and international sites.

Objective VI: "Use a statistical tool to independently (without prejudice of candidate) evaluate source deductions made in (iii) and (iv)"

In Chapter 7, multi-linear regression (MLR) was used to independently evaluate the source deductions made from aerosol optical properties in Chapters 4 to 6.

Overall project success

Although all the set objectives were achieved as indicated above, it does not imply the study was perfect. In fact, the candidate experienced several limitations and/or frustrations. For instance, it was stated several times that secondary aerosol formation and specifically sulphate (SO_4^{2-}) played an important role in the PM_{10} aerosol properties reported in this study (e.g. Chapter 2, section 2.2.5.1 and Chapter 4, section 4.3.2). However, size resolved aerosol chemical composition data were not available to verify this statement. Shorter-term (~18 months) aerosol mass

spectrometer (AMS) data were available (Tiitta *et al*., 2014), but only for PM_1, which could not be correlated with the PM_{10} aerosol optical properties. PM_1 DMPS data could also not be compared with aerosol size deductions made from PM_{10} α_{SP}. Aerosol optical properties could also only be determined at a single wavelength (i.e. 637 nm), since the MAAP used to quantify absorption was a single wavelength instrument. As previously stated (sections 4.3 and 4.4) meteorological conditions and specifically PBL and the formation of a low-level inversion layer(s) influenced the aerosol optical properties. It would, therefore, have been beneficial to for instance have the vertical structure data of the lower troposphere to better explain the results. Gierens *et al*. (2019) recently published such a two-year dataset for Welgegund, but this data became available too late to consider in this study, and it also did not cover the full six-year measurement period. The above-mentioned limitations and/or frustrations were mostly due to financial constraints, which ultimately determine the measurement suite (equipment and staff employed) at Welgegund. These aspects were beyond the control of the candidate.

8.3 Future perspectives

Although the study was successful (section 8.2), the candidate has certainly not fully exhausted the use of the dataset. In fact, a study such as this typically answers some scientific questions, but also raises new and/or alternative questions. These new and/or alternative questions do not necessarily indicate deficiencies of the current study, but are, in fact, a product of the current study and could guide future studies. It is therefore important that future perspectives be considered. The following recommendations with regard to future studies, within the limitations of the current dataset, can be made:

1. Although the aerosol optical properties were quantified and sources considered, it would be advantageous to also identify and quantify impacts of the aerosol optical properties. The most obvious impact would be to quantify climatic effect(s).
2. In this study, significant deductions with regard to sources and source regions were made. In future studies, many of these deductions could be investigated

in greater detail by, for instance, considering case studies. Examples of such case studies are:

a. Isolating biomass burning plumes and quantifying the change in aerosol optical properties with plume age (travel time) and/or oxidative conditions (e.g. differences between travel during day- and night-time).
b. Further verifying the significant influence of open biomass burning occurring in eastern Zimbabwe and central Mozambique on aerosol optical properties in the interior of South Africa.
c. Results presented in section 5.2.1.1, Figure 5-1, suggested that σ_{AP} values were elevated more than σ_{SP}, if air masses had passed over the KwaZulu-Natal and the Eastern Cape areas that border Lesotho. This somewhat contradicts the general observation that aged biomass burning plumes had higher σ_{SP} than σ_{AP}. It is therefore suggested that specific case studies should be considered to clarify the results.
d. In section 5.2.2.2, Figure 5-6b, the Cape Town area was indicated to be a potential source of pollution contributing to elevated σ_{AP} measured at Welgegund, during the coldest periods. It was suggested that such pollution was transported by cold fronts from the Cape Town area to the interior, which should be confirmed via further investigation.
e. It would be good to verify the origin of significant dust storms measured at Welgegund, with the eastern Free State being suggested as a significant source area from the current results.

3. It is also suggested to evaluate inter-annual variability of the aerosol optical properties measured at Welgegund.
4. Multiple-linear regression (MLR) was used in Chapter 7 as a tool for mathematical confirmation of factors and sources contributing to aerosol optical properties. In future non-linear method should also be considered.

Bibliography

Aaltonen, V., Lihavainen, H., Kerminen, V. -M., Komppula, M., Hatakka, J., Eneroth, K., Kulmala, M., and Viisanen, Y. 2006. Measurements of optical properties of atmospheric aerosols in Northern Finland, Atmospheric Chemistry and Physics, 6, 1155-1164, https://doi.org/10.5194/acp-6-1155-2006

Akagi, S. K., Yokelson, R. J., Wiedinmyer, C., Alvarado, M. J., Reid, J. S., Karl, T., Crounse, J. D., and Wennberg, P. O. 2011. Emission factors for open and domestic biomass burning for use in atmospheric models, Atmospheric Chemistry and Physics, 11, 4039-4072, doi:10.5194/acp-11-4039-2011

Anderson, J. O., Thundiyil, G. J. and Stolbach, A. 2012. Clearing the air: a review of the effects of particulate matter air pollution on human health, Journal of Medical Toxicology, 8, 166-175, doi:10.1007/s13181-011-0203-1

Anderson, T. L, Covert, D. S, Marshall, S. F., Laucks, M. L., Charlson, R. J., Waggoner, A. P., Orgen, J. A., Caldow, R., Holm, R. L., Quant, F.R., Sem, G. J., Wiendensohler, A., Ahlquist, N. A. and Bates, T.S. 1996. Performance Characteristics of a High-Sensitivity, Three-Wavelength, Total Scatter/Backscatter Nephelometer, American Meteorological Society, 13, 967-986, https://doi.org/10.1175/1520-0426(1996)013<0967:PCOAHS>2.0.CO;2

Anderson, T. L. and Ogren, J. A. 1998. Determining aerosol radiative properties using the TSI 3563 integrating nephelometer, Aerosol Science and Technology, 29, 57-69, https://doi.org/10.1080/02786829808965551

Andersson, S. M, Martinsson, B. G, Friberg, J., Brenninkmeijer, C. A. M., Rauthe-Schöch, A., Hermann, M., van Velthoven, P. F. J. and Zahn, A. 2013. Composition and evolution of volcanic aerosol from eruptions of Kasatochi, Sarychev and Eyjafjallajökull in 2008–2010 based on CARIBIC observations, Atmospheric Chemistry and Physics, 13, 1781-1796, https://doi.org/10.5194/acp-13-1781-2013

Andreae, M. O., 1995. Climate effects on chaning atmospheric aerosol levels. In: Henderson-Sellers, A., eds., World Survey of Climatology. Amsterdam: Elsevier, pp 341 - 392

Ångström, A. 1929. On the atmospheric transmission of sun radiation and on dust in the air, Geografiska Annaler A., 156-166, doi:10.2307/519399

Apostolovski-Trujic, T., Gardic, V. and Ivanovic, S. 2007. Pollution prevention and control techniques in the copper industry, Metalurgija – journal of metallurgy, 121, 215-222

Archibald, S., Roy, D.P., Van Wilgen, B.W., Scholes, R.J. 2008. What limits rire? An examination of driver's of burnt area in southern Africa. Global Change Biology, doi:10.1111/j.1365-2486.2008.01754.x

Arimoto, R. 2003. Sources and composition of aerosol particles. In: Potter, T. D. and Colman B. R., eds, Handbook of weather, climate, and water: atmospheric chemistry, hydrology, and societal impacts. New Jersey: Wiley Interscience, pp. 193-214

Atkinson, R. and Arey, J. 2003. Atmospheric Degradation of Volatile Organic Compounds, Chemical Reviews, 12, 4605-4638, https://doi.org/10.1021/cr0206420

Aurela, M., Beukes, J. P., Van Zyl, P. G., Vakkari, V., Teinilä, K., Saarikoskii, S., and Laakso, L. 2016. The composition of ambient and fresh biomass burning aerosols at a savannah site, South Africa, South African Journal of Science, 112, 1-8, http://dx.doi.org/10.17159/sajs.2016/20150223

Awang, N. R., Ramli, N. A., Yahaya, A. S. and Elbayoumi, M. 2015. Multivariate methods to predict ground level ozone during daytime, nighttime, and critical conversion time in urban areas, Atmospheric Pollution Research, 6, 726-734, https://doi.org/10.5094/APR.2015.081

Baek, B. H., Aneja, V. P. and Tong, Q. 2004. Chemical coupling between ammonia, acid gases, and fine particles, Environmental Pollution, 129, 89-98, https://doi.org/10.1016/j.envpol.2003.09.022

Baltensperger, U. and Furger, M. 2008. Aerosol Chemistry in Remote Locations. In: Colbeck, I.,ed, Environmental chemistry of aerosols. Oxford: Blackwell Publishing, pp. 217-252

Banerjee, G. K., Srivastava, K. K. and Chakraborty, M. K. 2001. SPM is the major pollution in open cast mining – a case study. Journal of Scientific and Industrial Research, 60, 416-420, http://nopr.niscair.res.in/handle/123456789/26491

Barnard, P. 1998. Biological diversity in Namibia: a clash of sea and land, fog and dust, Biodiversity and Conservation, 7, 415-417, https://doi.org/10.1023/A:1008840031391

Barry, R. G. and Hall-McKim, E. A. 2014. Essentials of the Earth's climate system. New York: Cambridge University Press.

Bergin, M., West, J., Keating, T., Russell, A. and Comer, J. 2005. Regional atmospheric pollution and Transboundary air quality management, Annual Review of Environment and Resources, 30, 1-37, https://doi.org/10.1146/annurev.energy.30.050504.144138

Bergin, M., Cass, G. R., Xu, J., Fang, F., Zeng, L. M., Yu, T., Salmon, L. G., Kiang, C. S., Tang, X. Y., Zhang, Y. H. and Chameides, W. L. 2001. Aerosol radiative, physical, and chemical properties in Beijing during June 1999, Journal of Geophysical Research - Atmospheres, 106, 17969–17980, https://doi.org/10.1029/2001JD900073

Betts, A. K. and Ball, J. H. 1997. Albedo over the boreal forest. Journal of Geophysical Research, 102, 28901-28909, doi:10.1029/96JD03876

Beukes, J. P, Van Zyl, P. G., Venter, A. D., Josipovic, M., Jaars, K., Tiitta, P., Pienaar, J. J., Laakso, L., Vakkari, V., Kulmala, M. and Worsnop, D. 2013. Source region plume characterisation of the interior of South Africa as observed at Welgegund, Clean Air Journal, 23, 7-10

Beukes, J. P., Venter, A. D., Josipovic, M., Van Zyl, P. G., Vakkari, V., Jaars, K., Dunn, M. and Laakso, L. 2015. In: Automated continuous air monitoring, in: Comprehensive Analytical Chemistry: Monitoring of air pollutants – Samling, sample, preparation and analytical techniques, Forbes, P.,ed. United Kingdom Elsevier, pp. 183-206

Boko, M., Niang, I., Nyong, A., Vogel, C., Githeko, A., Medany, M., Osman-Elasha, B., Tabo, R. and Yanda, P. 2007. Africa. In: Climate change 2007- impacts, adaptation and vulnerability, Parry, M., Canziani, O., Palutikof, J., Van der Linden, P., and Hanson, C., eds. Cambridge

Bond, T. C., Anderson, T. L. and Campbell, D. 1999. Calibration and intercomparison of filter-based measurements of visible light absorption by aerosols, Aerosol Science and Technology., 30, 582–600, https://doi.org/10.1080/027868299304435

Bond, T.C., Doherty, S.J., Fahey, D.W., Forster, P.M., Berntsen, T., Deangelo, B.J., Flanner, M.G., Ghan, S., *et al*. 2013. Bounding the role of black carbon in the climate system: A scientific assessment, Journal of Geophysical Research, 118, 5380-5552, https://doi.org/10.1002/jgrd.50171

Bond, T. C., Covert, D. S. and Müller, T. 2009. Truncation and Angular Scattering Corrections for Absorbing Aerosols in the TSI 3563 Nephelometer, Aerosol Science and Technology, 43, 866-871, doi:10.1080/02786820902998373

Bond, T. C., Streets, D. G., Yarber, K. F., Nelson, S. M., Woo, J.-H. and Klimont, Z. 2004. A technology-based global inventory of black and organic carbon emissions from combustion, 109, D14203, doi:10.1029/2003JD003697

Boschetti, L., Roy, D., Hoffmann, A.A. 2009. MODIS Collection 5 Burned Area Product - MCD45. User's Guide Version 2.0

Boschetti, L., Roy, D., Hoffmann, A.A., Humber, M. 2013. MODIS Collection 5.1 Burned Area Product - MCD45. User's Guide Version 3.0.1

Boucher, O. 2015. Atmospheric Aerosols: Properties and Climate Impacts. New York: Springer, doi:10.1007/978-94-017-9649-1

Bryant, R. G. 2003. Monitoring hydrological controls on dust emissions: preliminary observations from Etosha Pan, Namibia, Geographical Journal, 169, 131-141, https://doi.org/10.1111/1475-4959.04977

Campbell, J. R., Welton, E. J., Spinhirne, J.,D., Ji, Q., Tsay, S., Piketh, S. J., Barenburg, M. and Holben, B. N. 2003. Micropulse lidar observations of tropospheric aerosols over northeastern South Africa during the ARREX and SAFARI 2000 dry season experiments, Journal of Geophysical Research - Atmospheres, 108, 8497, doi:10.1029/2002JD002563

Carrico, C. M., Rood, M. J. and Ogren, J. A. 1998. Aerosol light scattering properties at Cape Grim, Tasmania, during the first aerosol characterization experiment (ACE 1). Journal of Geophysical Research - Atmospheres, 103, 16565-16574, https://doi.org/10.1029/98JD00685

Center for International Earth Science Information Network (CIESIN), Columbia University, United Nations Food and Agriculture Programme (FAO), and Centro Internacional de Agricultura Tropical (CIAT), 2005, Gridded Population of the World: Future Estimates (GPWFE), Palisades, NY: Socioeconomic Data and

Applications Center (SEDAC), Columbia University, http://sedac.ciesin.columbia.edu/gpw, 2016.

Cheng, Y. F., Wiedensohler, A., Eichler, H., Su, H., Gnauk, T., Brüggemann, E., Herrmann, H., Heintzenberg, J., Slanina, J., Tuch, T., Hu, M. and Zhang, Y. H. 2008. Aerosol optical properties and related chemical apportionment at Xinken in Pearl River Delta of China, Atmospheric Environment, 42, 6351-6372, doi:10.1016/j.atmosenv.2008.02.034

Chiloane, K.E., Beukes, J.P., Van Zyl, P.G., Maritz, P., Vakkari, V., Josipovic, M., Venter, A.D., Jaars, K., Tiitta, P., Kulmala, M., Wiedensohler, A., Liousse, C., Mkhatshwa, G.V., Ramandh, A. and Laakso, L. 2017. Spatial, temporal and source contribution assessments of black carbon over the northern interior of South Africa, Atmospheric Chemistry and Physics, 17, 6177-6196, doi:10.5194/acp-17-6177-2017

Chin, M, Kahn, R. A., Remer, L. A., Yu, H., Rind, D., Feingold, G., Quinn, P. K., Schwartz, S. E., Streets, D. G., DeCola, P. and Halthore, R. 2009. Atmospheric aerosol properties and climate impacts. Washington: U.S. climate change science program. 118p

Claes, M., Gysels, K., Van Grieken, R. and Harrison, R. M. 1998. Inorganic composition of atmospheric aerosols. In: Harrison, R. M and Van Grieken, E. E., eds, Atmospheric Particles, Wiley, Chichester

Cogho, E., Beukes, J. P., Van Zyl, P. G. 2019. An air quality assessment at Welgegund, a regional background site in the interior of South Africa. *In preparation*.

Collet, K. S., Piketh, S. and Ross, K., E. 2010. An assessment of the atmospheric nitrogen budget on the South African Highveld, South African Journal of Science, 106, 1-9, doi:10.4102/sajs.v106i5/6.220

Connell, D. W. 2005. Basic Concepts of Environmental Chemistry. 2nd ed. Boca Raton: Tylor and Francis Group

Conradie, E.H., Van Zyl, P.G., Pienaar, J.J., Beukes, J.P., Galy-Lacaux, C., Venter, A.D., and Mkhatshwa, G.V. 2016. The chemical composition and fluxes of atmospheric wet deposition at four sites in South Africa. Atmospheric Enviroment, 146, 113-131, doi:10.1016/j.atmosenv.2016.07.033

Crippa, M., Canonaco, F., Slowik, J. G., El Haddad, I., Decarlo, P. F., Mohr, C., Heringa, M. F., Chirico, R., Marchand, N., Temime-Roussel, B., Abidi, E., Poulain, L., Wiedensohler, A., Baltensperger, U. and Prevot, A. S. H. 2013. Primary and secondary organic aerosol origin by combined gas-particle phase source apportionment, Atmospheric Chemistry and Physics, 13, 8411-8426, doi:10.5194/acp-13-8411-2013

Csavina, J., Field, J., Taylor, M. P., Gao, S., Landázuri, A., Betterton E. A. and Sáez, A. E. 2012. A Review on the Importance of Metals and Metalloids in Atmospheric Dust and Aerosol from Mining Operations, Science of the Total Environment, 433C, 58-73, doi10.1016/j.scitotenv.2012.06.013

Delene, D. J. and Ogren, J. A. 2017. 2002. Variability of aerosol optical properties at four North American surface monitoring sites, Journal of the Atmospheric Scienices, 59, 1135-1150, http://dx.doi.org/10.1175/1520-0469(2002)059<1135:VOAOPA>2.0.CO;2

Department: Agriculture, Forestry and Fisheries: https://www.daff.gov.za, last access: 7 June 2017

Di Biagio, C., Formenti, P, Doppler, L., Gaimoz, C., Grand, N., Ancellet, G., Attié, J. -L., Bucci, S., Dubuisson, P., Fierli, F., Mallet, M. and Ravetta, F. 2016. Continental pollution in the Western Mediterranean basin: large variability of the aerosol single scattering albedo and influence on the direct shortwave radiative effect, Atmospheric Chemistry and Physics, 16, 10591-10607, doi:10.5194/acp-16-10591-2016

Diner, D. J., Abdou, W. A., Bruegge, C. J., Conel, J. E., Crean, K. A., Gaitley, B. J., Helmlinger, M. C., Kahn, R. A., Martonchik, J. V., Pilorz, S. H. and Holben, B. N. 2001. MISR aerosol optical depth retrievals over southern Africa during the SAFARI-2000 Dry Season Campaign, Geophysical Research Letters, 28, 3127-3130, https://doi.org/10.1029/2001GL013188

Draxler, R. R. and Hess, G. D. 2004. Description of the HYSPLIT 4 Modelling System. NOAA Technical Memorandum ERL ARL-224

Droughtsa: http://www.droughtsa.org.za/about-the-drought/rainfall-data.html, accessed 5 August 2019

Dubovik., O., Holben, B. N., Eck, T. F., Smirnov, A., Kaufman, Y. J., King, M. D., Tanré, D. and Slutsker, I. 2001. Variability of absorption and optical properties

of key aerosol types observed in worldwide locations, Journal of the Atmospheric Sciences, 59, 590-608, https://doi.org/10.1175/1520-0469(2002)059<0590:VOAAOP>2.0CO;2

Du Preez, S. P., Beukes, J. P. and Van Zyl, P. G. 2015. Cr(VI) Generation during flaring of CO-rich off-gas from closed ferrochromium submerged arc furnaces, Metallurgical and Materials Transactions B, 46, 1002-1010, https://doi.org/10.1007/s11663-014-0244-3.

Eck, T., Holben, B. N., Reid, J., Dubovik, O., Smirnov, A., O'neill, N., Slutsker, I. and Kinne, S. 1999. Wavelength dependence of the optical depth of biomass burning, urban, and desert dust aerosols, Journal of Geophysical Research, 104, 31333-31349, doi:10.1029/1999JD900923

Eck, T., Holben, B., Ward, D., Mukelabai, M., Dubovik, O., Smirnov, A., Schafer, J., Hsu, N., Piketh, S. and Queface, A. 2003. Variability of biomass burning aerosol optical characteristics in southern Africa during the SAFARI 2000 dry season campaign and a comparison of single scattering albedo estimates from radiometric measurements, Journal of Geophysical Research - Atmospheres, 108, doi:10.1029/2002JD002321

Ervens, B., Turpin, B. J. and Weber R. J. 2011. Secondary organic aerosol formation in cloud droplets and aqueous particles (aqSOA): a review of laboratory, field and model studies, Atmospheric Chemistry and Physics, 11, 11069-11102, https://doi.org/10.5194/acp-11-11069-2011

ESKOM: http://www.eskom.co.za/sites/heritage/Pages/Duvha.aspx [accessed 5 August 2019]

ESKOM: http://www.eskom.co.za/sites/heritage/Pages/MATLAPOWERSTATION.aspx [accessed 5 August 2019]

Facchini, M. C., Finessi, E., Decesari, S. and Fuzzi, S. 2010. Primary and secondary organic aerosols, Environmental quality, 3, 15-20

Fishman, J. 2003. Overview: Atmospheric chemistry. In: Potter, T. D. and Colman, B. R., eds. Handbook of weather, climate and water: Atmospheric chemistry, hydrology and societal impacts. New Jersey: Wiley-Interscience, pp. 3-28

Formenti, P., Winkler, H., Fourie, P., Piketh, S., Makgopa, B., Helas, G. and Andreae, M. O. 2002. Aerosol optical depth over a remote semi-arid region of

South Africa from spectral measurements of the daytime solar extinction and the nighttime stellar extinction, Atmospheric Research, 62, 11-32, https://doi.org/10.1016/S0169-8095(02)00021-2

Freiman, M. T. and Piketh, S. J. 2002. Air Transport into and out of the Industrial Highveld Region of South Africa, Journal of Applied Metereology, 42, 994-1002, https://doi.org/10.1175/1520-0450(2003)042<0994:ATIAOO>2.0.CO;2

Garland, R. M., Yang, H., Schmid, O., Rose, D., Nowak, A., Achtert, P., Wiedensohler, A., Takegawa, N., Kita, K., Miyazaki, Y., Kondo, Y., Hu, M., Shao, M., Zeng, L. M., Zhang, Y. H., Andreae, M. O. and Pöschl, U. 2008. Aerosol optical properties in a rural environment near the mega-city Guangzhou, China: implications for regional air pollution, radiative forcing and remote sensing, Atmospheric Chemistry and Physics, 8, 5161-5186, doi:10.5194/acp-8- 5161-2008

Garstang, M., Tyson, M., Swap, R., Edwards, M., Kållberg, P. and Lindesay, J. A. 1996. Horizontal and vertical transport of air over southern Africa, Journal of Geophysical Research, 101, 23721-23736, https://doi.org/10.1029/95JD00844

Gierens, R. T., Henriksson, S., Josipovic, M., Vakkari, V., Van Zyl, P. G., Beukes, J. P., Wood, C. R. and O'connor, E. J. 2019. Observing continental boundary-layer structure and evolution over the South African savannah using a ceilometer, Theoretical and Applied Climatology, 1-14, doi:10.1007/s00704-018-2484-7

Goldstein, A. H and Galbally, I. E. 2007. Known and Unexplored Organic Constituents in the Earth's Atmosphere, Environmental Science and Technology, 41, 1514-1521, https://doi.org/10.1021/es072476p

Gong, W., Zhang, M., Han, G., Ma, X. and Zhu, Z. 2015. An Investigation of Aerosol Scattering and Absorption Properties in Wuhan, Central China. Atmosphere-Basel, 6, 503-520, doi:10.3390/atmos6040503

Grythe, H., Ström, J., Krejci, R. Quinn, P. and Stohl, A. 2014. A review of sea-spray aerosol source functions using a large global set of sea salt aerosol concentration measurements, Atmospheric Chemistry and Physics, 14, 1277-1297, https://doi.org/10.5194/acp-14-1277-2014

Hänel, G. 1987. Radiation budget of the boundary layer: Part II. Simultaneous measurement of mean solar volume absorption and extinction coefficients of particles, Beitr. Phys. Atmos., 60, 241–247

Hansen, A. D. A., Rosen, H. and Novakov, T. 1984. The aethalometer – an instrument for the real-time measurement of optical absorption by aerosol particles, Science of the Total Environment, 36, 191–196

Haywood, J. M. and Boucher, O. 2000. Estimates of the direct and indirect radiative forcing due to tropospheric aerosols: A review, Reviews of Geophysics 38, 513-543, https://doi.org/10.1029/1999RG000078

Haywood, J. M. and Shine, K. P. 1995. The effect of anthropogenic sulphate and soot aerosol on the clear sky planetary radiation budget, Geophysical Research Letters, 22, 603-606, https://doi.org/10.1029/95GL00075

Hersey, S. P., Garland, R. M., Crosbie, E., Shingler, T., Sorooshian, A., Piketh, S. and Burger, R. 2015. An overview of regional and local characteristics of aerosols in South Africa using satellite, ground, and modelling data, Atmospheric Chemistry and Physics, 15, 4259-4278, doi:10.5194/acp-15-4259-2015

Heintzenberg, J. and Wiedensohler, A. 2006. Intercomparisons and Aerosol Calibrations of 12 Commercial Integrating Nephelometers of Three Manufacturers, American Metereological Society, 23, 902-914, https://doi.org/10.1175/JTECH1892.1

Hirsikko, A., Vakkari, V., Tiitta, P., Manninen, H., Gagné, S., Laakso, H., Kulmala, M., Mirme, A., Mirme, S. and Mabaso, D. 2012. Characterisation of sub-micron particle number concentrations and formation events in the western Bushveld Igneous Complex, South Africa, Atmospheric Chemistry and Physics, 12, 3951-3967, doi:10.5194/acp-12-3951-2012

Hirsikko, A.,Vakkari, V., Tiitta, P., Hatakka, J., Kerminen, V. –M., Sundström, A. –M., Beukes, J. P., Manninen, H. E., Kulmala, M. and Laakso, L. 2013. Multiple daytime nucleation events in semi-clean savannah and industrial environments in South Africa: analysis based on observations, Atmospheric Chemistry and Physics, 13, 5523-5532, doi:10.5194/acp-13-5523-2013

Intergovernmental Panel on Climate Change (IPCC). 2013. Climate Change 2013: The Physical Science Basis. http://www.ipcc.ch/report/ar5/wg1/ [accessed 12 November 2018]

Jaars, K., Beukes, J., Van Zyl, P., Venter, A., Josipovic, M., Pienaar, J., Vakkari, V., Aaltonen, H., Laakso, H. and Kulmala, M. 2014. Ambient aromatic hydrocarbon measurements at Welgegund, South Africa, Atmospheric Chemistry and Physics, 14, 7075-7089, doi:10.5194/acp-14-7075-2014

Jaars, K., Van Zyl, P. G., Beukes, J. P., Hellen, H., Vakkari, V., Josipovic, M., Venter, A. D., Räsänen, M., Knoetze, L., Cilliers, D. P., Siebert, S. J., Kulmala, M., Rinne, J., Guenther, A., Laakso, L. and Hakola, H. 2016. Measurements of biogenic volatile organic compounds at a grazed savannah grassland agricultural landscape in South Africa, Atmospheric Chemistry and Physics, 16, 15665-15688, https://doi.org/10.5194/acp-16-15665-2016

Jaars, K., Vestenius, M., Van Zyl, P. G., Beukes, J. P., Hellén, H., Vakkari, V., Venter, M., Josipovic, M., and Hakola, H. 2018. Receptor modelling and risk assessment of volatile organic compounds measured at a regional background site in South Africa. Atmospheric Environment, 172, 133-148, https://doi.org/10.1016/j.atmosenv.2017.10.047

Jacobson, M. 2002. Atmospheric pollution. Cambridge: Cambridge University Press.

Jayaratne, E. R. and Verma, T. S. 2001. The impact of biomass burning on the environmental aerosol concentration in Gaborone, Botswana, Atmospheric Environment, 35, 1821-1828, doi:10.1016/S1352-2310(00)00561-6

Jimenez, J. L., Canagaratna, M. R., Donahue, N. M., Prevot, A. S. H., Zhang, Q., Kroll, J. H., DeCarlo, P. F., Allan, J. D, *et al*. 2009. Evolution of Organic Aerosols in the Atmosphere, Science, 326, 1525, doi:10.1126/science.1180353

Junker, C., Jennings, S. G. and Cachier, H. 2006. Aerosol light absorption in the North Atlantic: trends and seasonal characteristics during the period 1989 to 2003, Atmospheric Chemistry and Physics, 6, 1913-1926, https://doi.org/10.5194/acp-6-1913-2006

Kamens, R. M. and Jaoui M. 2001. Modelling aerosol formation from α-pinene + NOx in the presence of natural sunlight using gas-phase kinetics and gas-particle partitioning theory, Environmental Science and Technology, 35, 1394-1405, https://doi.org/10.1021/es001626s

Kleefeld, C., O'dowd, C. D., O'reilly, S., Jennings, S. G., Aalto, P., Becker, E., Kunz, G. and De Leeuw, G. 2002. Relative contribution of submicron and supermicron particles to aerosol light scattering in the marine boundary layer, Journal of Geophysical Research, 107, 8103, doi:10.1029/2000JD000262

Kleynhans, E. L. J., Beukes, J. P., Van Zyl, P. G., Kestens, P. H. I. and Langa, J. M. 2012. Unique challenges of clay binders in a pelletised chromite pre-reduction process, Minerals Engineering, 34, 55-62, doi:10.1016/j.mineng.2012.03.021

Korhonen, K., Giannakaki, E., Mielonen, T., Pfüller, A., Laakso, L., Vakkari, V., Baars, H., Engelmann, R., Beukes, J. P., Van Zyl, P. G., Ramandh, A., Ntsangwane, L., Josipovic, M., Tiitta, P., Fourie, G., Ngwana, I., Chiloane, K. and Komppula, M. 2014. Atmospheric boundary layer top height in South Africa: measurements with lidar and radiosonde compared to three atmospheric models, Atmospheric Chemistry and Physics, 14, 4263-4278, doi:10.5194/acp-14-4263-2014

Kulmala, M., Suni, T., Lehtinen, K. E. J., Dal Maso, M., Boy, M., Reissell, A., Rannik, Ü., Aalto, P., Keronen, P., Hakola, H., Bäck, J., Hoffmann, T., Vesala, T. and Hari, P. 2004. A new feedback mechanism linking forests, aerosols, and climate, Atmospheric Chemistry and Physics, 4, 557-562, https://doi.org/10.5194/acp-4-557-2004

Kumar, K. R., Sivakumar, V., Reddy, R. R., Gopal, K. R. and Adesina, A. J. 2014. Identification and classification of different aerosol types over a subtropical rural site in mpumalanga, South Africa: seasonal variations as retrieved from the AERONET sunphotometer, Aerosol and Air Quality Research, 14, 108-123, doi:10.4209/aaqr.2013.03.0079

Laakso, L., Vakkari, V., Virkkula, A., Laakso, H., Backman, J., Kulmala, M., Beukes, J. P., Van Zyl, P. G., Tiitta, P., Josipovic, M., Pienaar, J. J., Chiloane, K., Gilardoni, S., Vignati, E., Wiedensohler, A., Tuch, T., Birmili, W., Piketh, S., Collett, K., Fourie, G. D., Komppula, M., Lihavainen, H., De Leeuw, G. and Kerminen, V. -M. 2012. South African EUCAARI measurements: seasonal variation of trace gases and aerosol optical properties, Atmospheric Chemistry and Physics, 12, 1847-1864, doi:10.5194/acp-12-1847-2012

Laban, T. L., Van Zyl, P. G., Beukes, J. P., Vakkari, V., Jaars, K., Borduas-Denekind, N., Josipovic, M., Thompson, A. M., Kulmala, M. and Laakso, L. 2018.

Seasonal influences on surface ozone variabiliby, Atmospheric Chemistry and Physics., 18, 15491-15514, https://doi.org/10.5194/acp-18-15491-2018

Labonne, M., Bréon, F. -M, and Chevallier, F. L. 2007. Injection height of biomass burning aerosols as seen from a spaceborne lidar, Geophysical. Research Letters, 34, 1-5, https://doi.org/10.1029/2007GL029311

Langmann, B., Duncan, B., Textor, C., Trentmann, J. and Van der Werf, G. R. 2009. Vegetation fire emissions and their impact on air pollution and climate. Atmospheric Environment, 43, 107-116, doi:10.1016/j.atmosenv.2008.09.047

Langner, J. and H. Rodhe. 1991. A global three-dimensional model of the tropospheric sulphur cycle, Journal of Atmospheric Chemistry, 13, 225-263, https://doi.org/10.1007/BF00058134

Lazaridis, M. 2008. Organic aerosols. In: Colbeck, I., ed, Environmental chemistry of aerosols. Oxford: Blackwell Publishing, pp. 91-115

Lee, R. G. M., Coleman, P., Jones, J. L., Jones, K. C. and Lohmann, R. 2005. Emission factors and importance of PCDD/Fs, PCNs, PAHs and PM10 form the domestic burning of coal and wood in the U.K. Environmental Science and Technology, 39, 1436-1447, https://doi.org/10.1021/es048745i

Li, Z., Xia, X., Cribb, M., Mi, W., Holben, B., Wang, P., Chen, H., Tsay, S. -C., Eck, T. F., Zhao, F., Dutton, E. G. and Dickerson, R. E. 2008. Aerosol optical properties and their radiative effects in northern China, Journal of Geophysical Research - Atmospheres, 112, 1-11, doi:10.1029/2006JD007382

Lihavainen, H., Hyvärinen, A., Asmi, E., Hatakka, J. and Viisanen, J. 2015. Long-term variability of aerosol optical properties in northern Finland, Boreal Environment Research 20, 526-541

Lighty, J. S., Veranth, J. M. and Sarofim, A. F. 2000. Combustion Aerosols: Factors Governing Their Size and Composition and Implications to Human Health, Journal of the Air and Waste Management Association, 1565-1618, https://doi.org/10.1080/10473289.2000.10464197

Lockwood, J. 2009. The climate of the earth. In: Hewit, C. N. and Jackson, A. V., eds. Atmospheric science for environmental scientists. West-Sussex: Wiley-Blackwell, pp. 1-25

Loock-Hattingh, M. M., Beukes, J. P., Van Zyl, G. P. and Tiedt, L. R. 2015. Cr(VI) and conductivity as indicators of surface water pollution from ferrochrome

production in South Africa: Four case studies, Metallurgical and Materials Transactions B., 46, 2315-2325, https://doi.org/10.1007/s11663-015-0395-x

Lourens, A. S., Beukes, J. P., Van Zyl, P. G., Fourie, G. D., Burger, J. W., Pienaar, J. J., Read, C. E. and Jordaan, J. H. 2011. Spatial and temporal assessment of gaseous pollutants in the Highveld of South Africa, South African Journal of Science, 107, 1-8, doi:10.4102/sajs.v107i1/2.269

Lourens, A. S., Butler, T. M., Beukes, J. P., Van Zyl, P. G., Beirle, S., Wagner, T. K., Heue, K. -P., Pienaar, J. J., Fourie, G. D. and Lawrence, M. G. 2012. Re-evaluating the NO_2 hotspot over the South African Highveld, South African Journal of Science, 108, 83-91, http://dx.doi.org/10.4102/sajs.v108i11/12.1146

Ludwig, J., Marufu, L. T., Huber, B., Andreae, M. O. and Helas. G. 2003. Domestic Combustion of Biomass Fuels in Developing Countries: A Major Source of Atmospheric Pollutants, Journal of Atmospheric Chemistry, 44, 23-37, https://doi.org/10.1023/A:1022159910667

Mafusire, G., Annegarn, H. J., Vakkari, V., Beukes, J. P., Josipovic, M., Van Zyl, P. G., and Laakso, L. 2016. Submicrometer aersols and excess CO as tracers for biomass burning air mass transport over southern Africa, Journal of Geophysical Research, 121, 10262-10282, doi:10.1002/2015JD023965

Marconi, M., Sferlazzo, D. M., Becagli, S., Bommarito, C., Calzolai, G., Chiari4, M., di Sarra, A., Ghedini, C., Gómez-Amo, J. L., Lucarelli, F., Meloni, D., Monteleone, F., Nava, S., Pace, G., Piacentino, S., Rugi, F., Severi, M., Traversi, R. and Udisti, R. 2014. Saharan dust aerosol over the central Mediterranean Sea: PM10 chemical composition and concentration versus optical columnar measurements, Atmopsheric Chemistry and Physics, 14, 2039-2054, https://doi.org/10.5194/acp-14-2039-2014

Maritz, P., Beukes, J.P., Van Zyl, P.G., Liousse, C., Gardrat, E., Ramandh, A. and Mkhatshwa, G.V. 2019. Temporal and source assessments of organic and elemental carbon at sites in the northern South Africa interior, sumbitted to Journal Atmospheric Chemistry

Massoli, P., Baynard, T., Lack, D. A., Brock, C. A., Murphy, D. M., and Lovejoy, E. R. 2009. Uncertainty in Light Scattering Measurements by TSI Nephelometer: Results from Laboratory Studies and Implications for Ambient Measurements,

Aerosol Science and Technology, 43, 1064-1074, doi:10.1080/02786820903156542

Mcgill, M. J., Hlavka, D. J., Hart, W. D., Welton, E. J. and Campbell, J. R. 2003. Airborne lidar measurements of aerosol optical properties during SAFARI-2000, Journal of Geophysical Research – Atmospheres, 108, 8493, doi:10.1029/2002JD002370

Montilla, E., Mogo, S., Cachorro, V., Lopez, J., and Frutos, A. D. 2011. Absorption, scattering and single scattering albedo of aerosols obtained from in situ measurements in the subarctic coastal region of Norway, Atmospheric Chemistry and Physics, 11, 2161-2182, doi:10.5194/acpd-11-2161-2011

Mucina, L. and Rutherford, M. C. (Eds.). 2006. The vegetation of South Africa, Lesotho and Swaziland, South African National Biodiversity Institute, Pretoria, South Africa

Müller, T., Henzing, J. S., De Leeuw, G., Wiedensohler, A., Alastuey, H., Bizjak, M., Collaud Coen, M., Engström, J. E., Gruening, C., Hillamo, R., Hoffer, A., Imre, K., Ivanow, P., Jennings, G., Sun, J. Y., Klaivitis, N., Karlsson, H., Komppula, M., Laj, P., Li, S. -M., Lunder, C., Marinoni, A., Martins dos Santos, S., Moerman, M., Nowak, A., Orgren, J. A., Petzold, A., Pichon, J. M., González, S. R., Sharma, S., Sheridan, P. J., Teinilä, K., Tuch, T., Viana, M., Virkkula, A., Weingartner, E., Wilhelm, R. and Wang, Y. Q. 2011. Characterization and intercomparison of aerosol absorption photometers: result of two intercomparison workshops, Atmospheric Measurement Techniques, 4, 245-268, https://doi.org/10.5194/amt-4-245-2011

National Environmental Management: Air Quality Act, 2004 (Act no. 39 of 2004): declaration of the Waterberg National prioriy area. Government Gazette. No. 33600 [online]. 2012 [cited 3 November 2018]. Available from: https://www.environment.gov.za/legislation/gazetted_notices

Nieminen, T., Kerminen, V. -M., Petäjä, T., Aalto, P. P., Arshinov, M., Asmi, E., Baltensperger, U., Beddows, D. C. S., Beukes, J. P., Collins, D., Ding, A., Harrison, R. M., Henzing, B., Hooda, R., Hu, M., Hõrrak, U., Kivekäs, N., Komsaare, K., Krejci, R., Kristensson, A., Laakso, L., Laaksonen, A., Leaitch, W. R., Lihavainen, H., Mihalopoulos, N., Németh, Z., Nie, W., O'dowd, C., Salmal, I., Sellegri, K., Svenningsson, B., Swietlicki, E., Tunved, P., Ulevicius,

V., Vakkari, V., Vana, M., Wiedensohler, A., Wu, Z., Virtanen, A. and Kulmala, K. 2018. Global analysis of continental boundary layer new particle formation based on long-term measurements, Atmospheric Chemistry and Physics, 18, 14737-14756, https://doi.org/10.5194/acp-18-14737-2018

Pak, B. C., *et al*. 2003. Measurements of biomass burning influences in the troposphere over southeast Australia during the SAFARI 2000 dry season campaign. Journal of Geophysical Research, 108, 8480, doi:10.1029/2002JD002343

Pathak, R. K., Wu, W. S. and Wang, T. 2009. Summertime PM2.5 ionic species in four major cities of China: nitrate formation in an ammonia-deficient atmosphere, Atmospheric Chemistry and Physics, 9, 1711-1722, https://doi.org/10.5194/acp-9-1711-2009

Penner, J. E., Andreae, M. Annegarn, H., Barrie, l., Feichter, D., Hegg, D., Jayaraman, A., Leaitch, R., Murphy, D., Nganga, J. and Pitari, G. 2001. Aerosols, their direct and indirect effects. In Houghton, J.T., Ding, Y., Griggs, D.J., Noguer, M., Van der Linden, P.J., Dai, X., *et al*, eds. Climate Change 2001: The Scientific Basis. Contribution of Working Group I to the Third Assessment Report of the Intergovernmental Panel on Climate Change, Cambridge, UK, & NY, USA: Cambridge University Press. pp. 298-348

Petzold, A., Kramer, H. and Schönlinner, M. 2002. Continuous Measurement of Atmospheric Black Carbon using a multi-Angle Absorption Photometer, Environmental Science and Pollution Research, 4, 78–82

Petzold, A., Schloesser, M., Sheridan, P. J., Arnott, W. P., Ogren, J. A. and Virkkula, A. 2005. Evaluation of Multi-Angle Absorption Photometry for Measuring Aerosol Light Absorption, Aerosol Science and Technolgy, 39, 40–51, https://doi.org/10.1080/027868290901945

Petzold, A. and Schönlinner, M. 2004. Multi-Angle Absorption Photometry – A New Method for the Measurement of Aerosol Light Absorption and Atmospheric Black Carbon, Journal of Aerosol Science, 35, 421–441, https://doi.org/10.1016/j.jaerosci.2003.09.005

Petzold, A., Ogren, J.A., Fiebig, M., Laj, P., Li, S.-M., Baltensperger, U., Holzer-Popp, T., Kinne, S., Pappalardo, G., and Sugimoto, N. 2013.

Recommendations for reporting "black carbon" measurements. Atmospheric Chemistry and Physics, 13(16), 8365–8379, doi: 10.5194/acp-13-8365-2013

Pidwirny, M. 2019. Understanding physical geograply [online]. Canada: Our planet earth publishing. Available from: Google Play [acessed 4 January 2019]

Piketh, S. J., Tyson, P. D. and Steffen, W. 2000. Aeolian transport from southern Africa and iron fertilization of marine biota in the South Indian Ocean, South African Journal of Science, 96, 244-246

Pöschl, U. 2005. Atmospheric Aerosols: Composition, transformations, climate and health effects. Angewandte Chemie International Edition, 44, 7520-7540

Pretorius, I., Piketh, S., Burger, R. and Neomogus, H. 2015. A perspective on South Africa coal fired power station emissions, Journal of Energy southern Africa, 26, 27-40

Pun, B.K. and Seigneur, C. 2001. Sensitivity of particulate matter nitrate formation to precursor emissions in the California San Joaquin Valley, Environmental Science and Technology, 35, 2979-2987, https://doi.org/10.1021/es0018973

Queface, A. J., Piketh, S. J., Eck, T. F., Tsay, S. -C. and Mavume, A. F. 2011. Climatology of aerosol optical properties in Southern Africa, Atmospheric Environment, 45, 2910-2921, doi:10.1016/j.atmosenv.2011.01.056

Ramachandran, S. 2018. Atmospheric aerosols: Characteristics and radiative effects [online]. Boca Raton: CRC Press. Available from: Google Play [accessed 12 February 2019]

Ramanathan, V., and Carmichael, G. 2008. Global and regional climate changes due to black carbon, Nature Geoscience, 1, 221-227, doi:10.1038/ngeo156

Reid, J. S., Eck, T. F., Christopher, S. A., Hobbs, P. V. and Holben, B.: 1999. Use of the Ångström exponent to estimate the variabilty of optical and physical properties of aging smoke paricles in Brazil, Journal of Geophysical Research - Atmospheres, 104, 27473-27489, https://doi.org/10.1029/1999JD900833

Ross, K. E., Piketh S. J., Bruintjes, R. T., Burger, R. P., Swap, R. J. and Annegarn, H.J. 2003. Spatial and seasonal variations in CCN distribution and the aerosol-CCN relationship over southern Africa, Journal of Geophysical Research, 108, NO. D13, 8481, doi:10.1029/2002JD002384

Roy, D. P., Boschetti, L., Justice, C.O. and Ju, J. 2008. The collection 5 MODIS burned area product – global evolution by comparison with the MODIS active

fire product, Remote Sensing of Environment, 112, 3690-3707, doi:10.1016/j.rse.2008.05.013, 2008

Sahu, L. K., Kondo, Y., Miyazaki, Y. Pongkiatkul, P. and Kim Oanh, N.T. 2011. Seasonal and diurnal variations of black carbon and organic carbon aerosols in Bangkok, Journal of Geophysical Research, 116, D15302, doi:10.1029/2010JD015563,

Salkind, N. J. 2010. Root Mean Square Error. (In Encyclopedia of research design Thousand Oaks, CA: SAGE Publications Ltd. http://dx.doi.org/10.4135/9781412961288.n392. Date of access 17 October 2019)

Schindell, D. T., Chin, M., Dentener, F., Doherty, R. M., Faluveg, G. Fiore, A. M., Hess, P., Koch D. M., *et al*. 2008. A multi-model assessment of pollution transport to the Arctic, Atmospheric Chemsitry and Physics, 8, 5353-5372, https://doi.org/10.5194/acp-8-5353-2008

Schulze, B. C.,. Wallace, H. W., Flynn, J. H., Lefer, B. L., Erickson, M. H., Jobson, B. T., Dusanter, S., Griffith, S. M., Hansen, R. F.,Stevens, P. S., Van Reken, T. and Griffin, R. J. 2017. Differences in BVOC oxidation and SOA formation above and below the forest canopy, Atmopsheric Chemistry and Physics, 17, 1805-182, doi:10.5194/acp-17-1805-2017

Schuster, G. L., Dubovik, O., and Holben, B. N. 2006. Angstrom exponent and bimodal aerosol size distributions. Journal of Geophysical Research - Atmospheres, 111, doi:10.1029/2005JD006328

Schwela, D., Zali, O. and Schwela, P. 1997. Motor vehicle air pollution: public health impact and control measures, Geneva, 338p

Seinfield, J. H. and Pandis, S.P. 2016. Atmospheric Chemistry and Physics: From Air Pollution to Climate Change. New Jersey: John Wiley and Sons Inc. 1211p

Shen, Y., Virkkula, A., Ding, A., Wang, J., Chi, X., Nie, W., Qi, X., Huang, X., Liu, Q., Zheng, L., Xu, Z., Petäjä, T., Aalto, P. P., Fu, C. and Kulmala, M. 2018. Aerosol optical properties at SORPES in Nanjing, east China, Atmospheric Chemisty and Physics, 18, 5265-5292, https://doi.org/10.5194/acp-18-5265-2018

Shiraiwa, M., Ueda, K., Pozzer, A., Lammel, G. Kampf, C. J., Fushimi, A., Enami, S., Arangio, A. M, Fröhlich-Nowoisky, J., Fujitani, Y., Furuyama, A., Lakey, P. S. J., Lelieveld, J., Lucas, K., Morino, Y., Pöschl, U., Takahama, S., Takami, A.,

Tong, H., Weber, B., Yoshino, A. and Sato, K. 2017. Aerosol health effects from molecular to global scales, Environmental Science and Technoloqy, 51, 13545-13567, https://doi.org/10.1021/acs.est.7b04417

Slemr, F., Brunke, E. -G., Whittlestone, S., Zahorowski, W., Ebing-Haus, R., Kock, H. H. and Labuschagne, C. 2013. 222 Rn-calibratedmercury fluxes from terrestrial surface of southern Africa, Atmospheric Chemistry and Physics, 13, 6421-6428, doi:10.5194/acp-13-6421-2013

Slemr, F., Angot, H., Dommergue, A., Magand, O., Barret, M., Weigelt, A., Ebinghaus, R., Brunke, E. -G., Pfaffhuber, K. A., Edwards, G., Howard, D., Powell, J., Keywood, M. and Wang, F. 2015. Comparison of mercury concentrations measured at several sites in the Southern Hemisphere, Atmospheric Chemistry and Physics, 15, 3125-3133, doi:10.5194/acp-15-3125-2015

Smith, S. J., Van Aardenne, J., Klimont, Z., Andres, R. J., Volke, A. and Arias, S. D. 2011. Anthropogenic sulphur dioxide emission: 1850–2005, Atmospheric Chemistry and Physics, 11, 1101-1116, doi:10.5194/acp-11-1101-2011

South Africa. 2006. Declaration of the Vaal Triangle Air-shed Priority Area in terms of Section 18(1) of the National Environmental Management: Air Quality Act 2004, (ACT NO. 39 OF 2004). Government gazette, 28732: 21 Apr. Available: Department Environmental Affairs RSA. Date of acces: 5 Oct. 2018. Available from: https://www.environment.gov.za/legislation/gazetted_notices/archived_gazetted_notices

South africa. 2007. Declaration for the Highveld as Priority Area in terms of Section18(1) of the National Environmental Management: Air Quality Act, 2004 (ACT NO. 39 OF 2004). Government gazette, 35018: 23 Nov. Available: Department Environmental Affairs RSA. Date of access: 5 Oct. 2018. Available from: https://www.environment.gov.za/legislation/gazetted_notices/archived_gazetted_notices

South Africa. 2012. National Environmental Management: Air Quality Act, 2004 (ACT NO. 39 OF 2004) Declaration of the Waterberg National Priority Area.

Government gazette, 35435: 15 Jun. Date of access: 5 Oct. 2018. Available from: https://www.environment.gov.za/legislation/gazetted_notices

StatsSA: 2019. http://www.statssa.gov.za/?page_id=1021&id=city-of-cape-town-municipality, accessed 12 April 2019

Squizzato, S., Masiol, M., Brunelli, A.,Pistollato, S., Tarabotti, E., Rampazzo, G. and Pavoni, B. 2013. Factors determining the formation of secondary inorganic aerosol: a case study in the Po Valley (Italy), Atmopheric Chemistry and Physics, 13, 1927-1939, https://doi.org/10.5194/acp-13-1927-2013

Swap, R. J., Annegarn, H. J., Suttles, J. T., King, M. D., Platnick, S., Privette, J. L. and Scholes, R. J. 2003. Africa burning: a thematic analysis of the Southern African Regional Science Initiative (SAFARI 2000), Journal of Geophysical Research - Atmospheres, 108, doi:10.1029/2003JD003747

Techcentral: https://techcentral.co.za/live-charts-show-awesome-power-cape-storm/74728/, accessed 12 April 2019

Ten Brink, H., Otjes, R., Jongejan, P. and Slanina, S. 2007. An instrument for semi-continuous monitoring of the size-distribution of nitrate, ammonium, sulphate and chloride in aerosol, Atmospheric Environment, 41, 2768-2779, https://doi.org/10.1016/j.atmosenv.2006.11.041

Tiitta, P., Vakkari, V., Croteau, P., Beukes, J., Van Zyl, P., Josipovic, M., Venter, A., Jaars, K., Pienaar, J. and Ng, N. 2014. Chemical composition, main sources and temporal variability of PM 1 aerosols in southern African grassland, Atmospheric Chemistry and Physics, 14, 1909-1927, doi:10.5194/acp-14-1909-2014

Tong, H. Y., Hung, W. T. and Cheung, C. S. 2011. On-road motor vehicle emissions and fuel consumption in urban driving conditions, Journal of the Air and Water Management Association, 50, 543-554, https://doi.org/10.1080/10473289.2000.10464041

Turner, J. and Colbeck, I. 2008. Physical and chemical properties of atmospheric aerosols. In: Colbeck, J., ed. Environmental chemistry of aerosols. United Kingdom: Blackwell Publishing, pp. 1-29

Tyson, P. D., and Preston-Whyte, R. A.. 2000. The Weather and Climate of Southern Africa, New York: Oxford University Press

Tyson, P., Garstang, M., and Swap, R. 1996. Large-scale recirculation of air over southern Africa, Journal of Applied meteorology, 35, 2218-2236, http://dx.doi.org/10.1175/1520-0450(1996)035<2218:LSROAO>2.0.CO;2

Vakkari, V., Laakso, H., Kulmala, M., Laaksonen, A., Mabaso, D., Molefe, M., Kgabi, N. and Laakso, L. 2011. New particle formation events in semi-clean South African savannah, Atmospheric Chemistry and Physics, 11, 3333-3346, doi:10.5194/acp-11-3333-2011

Vakkari, V., Beukes, J. P., Laakso, H., Mabaso, D., Pienaar, J. J., Kulmala, M. and Laakso, L. 2013. Long-term observations of aerosol size distributions in semi-clean and polluted savannah in South Africa, Atmospheric Chemistry and Physics, 13, 1751-1770, doi:10.5194/acp- 13-1751-2013

Vakkari, V., Kerminen, V. -M., Beukes, J. P., Tiitta, P., Van Zyl, P. G., Josipovic, M., Venter, A. D., Jaars, K., Worsnop, D. R., Kulmala, M. and Laakso, L. 2014. Rapid changes in biomass burning aerosols by atmospheric oxidation. Geophysical Research Lettets, 41, 2644-2651, https://doi.org/10.1002/2014GL059396

Vakkari, V., Tiitta, P., Jaars, K., Croteau, P., Beukes, J. P., Josipovic, M., Kerminen, V. -M., Kulmala, M., Venter, A. D., Van Zyl, P. G., Worsnop, D. and Laakso, L. 2015. Reevaluating the contribution of sulphuric acid and the origin of organic compounds in atmospheric nanoparticle growth, Geophysical Research Letters, 42, doi:10.1002/2015GL066459

Vakkari, V., Beukes, J. P., Dal Maso, M., Aurela, M., Josipovic, M. and Van Zyl, P. G. 2018. Major secondary aerosol formation in southern Africa open biomass burning plumes, Nature Geoscience, 11, 580-583, https://doi.org/10.1038/s41561-018-0170-0

Van der Werf, G. R., Randerson, J.T., Giglio, L., Collatz, G.J., Mu, M., Kasibhatla, P. S., Morton, D. C., DeFries, R. S., Jin, Y. and Van Leeuwen, T. T. 2010. Global fire emissions and the contribution of deforestation, savanna, forest, agricultural, and peat fires (1997–2009), Atmospheic Chemistry and Physics, 10, 11, 707-11,735, doi:10.5194/acp-10-11707-2010

Venter, A. D., Vakkari, V., Beukes, J. P., Van Zyl, P. G., Laakso, H., Mabaso, D., Tiitta, P., Josipovic, M., Kulmala, M. and Pienaar, J. J. 2012. An air quality assessment in the industrialised western Bushveld Igneous Complex, South

Africa, South African Journal of Sciences, 108, 1-10, http://dx.doi.org/10.4102/sajs.v108i9/10.1059

Venter, A. D., Beukes, J. P., Van Zyl, P. G., Brunke, E. -G., Labuschagne, C., Slemr, F., Ebinghaus, R. and Kock, H. 2015. Statistical exploration of gaseous elemental mercury (GEM) measured at Cape Point from 2007 to 2011, Atmosphric Chemistry and Physics, 15, 10271-10280, doi:10.5194/acp-15-10271-2015

Venter, A. D., Van Zyl, P. G., Beukes, J. P., Josipovic, M., Hendriks, J., Vakkari, V., and Laakso, L. 2017. Atmospheric trace metals measured at a regional background site (Welgegund) in South Africa, Atmosphric Chemistry and Physics, 17, 4251-4263, doi:10.5194/acp-17-4251-2017

Venter, A. D., Van Zyl, G. P. ,Beukes, J. P., Swartz, J. -S., Josipovic, M., Vakkari, V., Laakso, L. and Kulmala, M. 2018. Size-resolved characteristics of inorganic ionic species in atmopheric aerosols at a regional background site on the South African Highveld, Journal of Atmospheric Chemistry, 1-20, https://doi.org./10.1007/s10874-018-9378-z

Virkkula, A., Backman, J., Aalto, P. P., Hulkkonen, M., Riuttanen, L., Nieminem, T., Dal Maso, M., Sogacheva, L., De Leeuw, G. and Kulmala, M. 2011. Seasonal cycle, size, dependencies, and source analysis of aerosol optical properties at the SMEAR II measurement station in Hyytiala, Finland, Atmosphric Chemistry and Physics, 11, 4445-4468, doi:10.5194/acp-11-4445-2011

Wang, M., Xu, B., Cao, J., Tie, X., Wang, H., Zhang, R., Qian, Y., Rasch, P. J., Zhao, S., Wu, G., Zhao, H., Joswiak, D. R., Li, J., and Xie, Y. 2005 Carbonaceous aerosols recorded in a southeastern Tibetan glacier: analysis of temporal variations and model estimates of sources and radiative forcing, Atmospheric Chemistry and Physics, 15, 1191-1204, https://doi.org/10.5194/acp-15-1191-2015

Weijers, E. P., Sahan, E., Ten Brink, H. M., Schaap, M., Matthijsen, J., Otjes, R. P. and Van Arkel. F. 2010. Contribution of secondary inorganic aerosols to PM10 and PM2.5 in the Netherland; measurement and modelling results. https://www.pbl.nl/en/publications/2010/Contribution-of-secondary-inorganic-aerosols-to-PM10-and-PM2-5-in-the-Netherlands [accessed Feb 2019]

Westcott, G., Tacke, M., Schoeman, N., and Morgan, N. 2007. Impala Platinum Smelter, Rustenburg—an integrated smelter off-gas treatment solution, Journal of the Southern African Institute of Mining and Metallurgy, 107, 281-287, httpd://hdl.handle.net/10520/AJA0038223X_3

World Health Organization (WHO). Air quality guidelines for particulate matter, ozone, nitrogen dioxide and sulphur dioxide – global update 2005. https://www.who.int/phe/health_topics/outdoorair/outdoorair_aqg/en/ [accessed 10 Nov. 2018]

Worobiec, A., De Hoog, J., Osán, J., Szalóki, I., Ro, C. -U. and Van Grieken, R. 2003. Thermal stability of beam sensitive atmospheric aerosol particles in electron probe microanalysis at liquid nitrogen temperature, Spectrochimica Acta Part B: Atomic Spectroscopy, 58, 479-496. https://doi.org/10.1016/S0584-8547(03)00013-2

Williams, P. I. and Baltensperger, U. 2009. Particulate matter in the atmosphere. In: Hewit, C. N. and Jackson, A. V., eds. Atmospheric science for environmental scientists. West Sussex: Wiley and Blackwell, pp. 168-197

Xu, J., Bergin, M. H., Yu, X., Liu, G., Zhao, J., Carrico, C. M. and Baumann, K. 2002. Measurement of aerosol chemical, physical and radiative properties in the Yangtze delta region of China, Atmospheric Evironment, 36, 161-173, https://doi.org/10.1016/S1352-2310(01)00455-1

Xu, J., Bergin, M. H., Greenwald, R., Schauer, J. J., Shafer, M. M., Jaffrezo, J. L., and Aymoz, G. 2004. Aerosol chemical, physical, and radiative characteristics near a desert source region of northwest China during ACE-Asia, Journal of Geophysical Research - Atmospheres, 109, 1-14, https://doi.org/10.1029/2003JD004239

Yan, P., Tang, J., Huang, J., Mao, J. T., Zhou, X. J., Liu, Q., Wang, Z. F. and Zhou, H. G. 2008. The measurement of aerosol optical properties at a rural site in Northern China, Atmospheric Chemistry and Physics, 8, 2229-2242, https://doi.org/10.5194/acp-8-2229-2008